2017

Synthesis and Characterization of Metallic Nanoparticles for Catalytic Applications

Sarah Smith
Virginia Commonwealth University

Synthesis and Characterization of Metallic Nanoparticles for Catalytic Applications

A dissertation in partial fulfillment of the requirement for the degree of doctor of philosophy at Virginia Commonwealth University

by

Sarah Emily Smith

B.S., University of Mary Washington, Virginia, 2012

Director: Everett E. Carpenter

Department of Chemistry

Virginia Commonwealth University

Richmond, Virginia

April 2017

Acknowledgements

With the completion of this work, there are so many people whom I would like to thank. First and foremost, I want to thank my family for all of their encouragement, moral, and emotional support. Without all of your support, I would have never started this endeavor. I want to thank my research adviser Dr. Carpenter for his guidance during this journey and for allowing me to explore my own research interests. I want to thank the VCU chemistry department, my committee, and the chemistry department at UMW. Lastly, I want to thank my lab mates Dan, Zach, Stan, April, Turki, Dustin, and especially Brent and Melissa. Thank you all for your suggestions and company and putting up with me the last few years. We have been through so much together and have formed friendships that will last a lifetime. This journey would have been much harder without you all.

Table of Contents

Acknowledgements ii
Table of Contents iii
List of Figures vii
List of Tables x
Abstract 1
Chapter 1: Introduction and Overview 3
1.1. Overview 3
1.2. Nanoparticle Catalysis 5
1.2.1. Cross-coupling Reactions 7
1.2.1.1. Suzuki Cross-coupling Reaction 7
1.2.1.1.1. Common Catalysts 8
1.2.1.2. Songashira Reaction 9
1.2.1.2.1. Common Catalysts 10
1.2.1.3. Heck Reaction 10
1.2.1.3.1. Common Catalysts 11
1.2.2. Fischer Tropsch Synthesis 12
1.2.2.1. Common Catalysts 13
1.2.3. Hydrogenation Reactions 15
1.2.3.1. Common Catalysts 16
1.3. Nucleation and Growth 16
1.3.1. Bimetallic Nanoparticle Synthesis 19
1.3.1.1. Choice of Precursor 20
1.4. Conventional Synthesis Methods 21
1.4.1. Polyol Method 21
1.4.2. Turkevich Method 23
1.5. Microwave Synthesis 25
1.5.1. Microwave Synthesis of Inorganic Materials 29

1.6. Flow Chemistry 29
1.6.1. Continuous Flow Synthesis of Inorganic Materials 31
1.7. Summary of Objectives 31
Chapter 2: Characterization 33
2.1. Introduction 33
2.2. X-Ray diffraction (XRD) 34
2.2.1. Scherrer Analysis 36
2.2.2. Reitveld Analysis 36
2.2.3. Elevated Temperature XRD (HTK-XRD) 37
2.3. Transmission Electron Microscopy (TEM) 37
2.3.1. Electron Energy Loss Spectroscopy (EELS) 38
2.4. Scanning Electron Microscopy (SEM) 39
2.4.1. Energy Dispersion Spectroscopy (EDS) 39
2.5. Dynamic Light Scattering (DLS) 40
2.6. X-Ray photoelectron Spectroscopy (XPS) 42
2.7. Vibrating Sample Magnetometry (VSM) 45
2.8. Thermogravimetric Analysis (TGA) 46
Chapter 3: Synthesis and Characterization of CuPd Nanoparticles 48
3.1. Overview and Motivation 48
3.2. Introduction 48
3.3. Experimental Methods 49
3.3.1. Synthesis 49
3.3.2. Characterization 50
3.3.3. Catalytic Testing 51
3.3.3.1. Suzuki Cross Coupling Reaction 51
3.3.3.2. Heck Coupling Reaction 51
3.3.3.3. Sonogashira Coupling Reaction 52
3.3.3.4. Recyclability Testing of CuPd in Suzuki Cross-coupling reactions 52
3.4. Results and Discussion 53
3.4.1. Reactivity of CuPd nanoparticles in Suzuki cross-coupling reactions 56
3.4.2. Reactivity of CuPd nanoparticles in Heck and Sonogashira coupling reactions 59

3.5. Conclusions 61
Chapter 4: Continuous flow synthesis of Cu@M (M=Ni, Co) core/shell nanocomposites 62
4.1. Overview and Motivation 62
4.2. Introduction 62
4.3. Experimental Methods 64
4.3.1. Continuous Synthesis Capillary Microreactor 64
4.3.2. Synthesis of Cu@M nanocomposites 65
4.3.3. Characterization 65
4.3.4. Fischer Tropsch Testing 65
4.4. Results and Discussion 66
4.4.1. Characterization of Cu@M nanocomposites 67
4.4.2. Temperature Stability on Core/Shell structure 72
4.5. Catalytic Activity for Fischer Tropsch 75
4.6. Conclusions 79
Chapter 5: Continuous Microwave Flow Synthesis of Platinum Nanoparticles 81
5.1. Overview and Motivation 81
5.2. Introduction 81
5.3. Experimental Methods 82
5.3.1. Synthesis of platinum nanoparticles on benchtop 82
5.3.2. Synthesis of platinum nanoparticles using a conventional microwave 82
5.3.3. Synthesis of platinum nanoparticles with continuous flow microwave capillary reactor 83
5.3.4. Synthesis of platinum nanoparticles using a continuous stir tank microwave reactor 84
5.3.5. Characterization 84
5.3.6. Hydrogenation Reactions 85
5.4. Results and Discussion 85
5.4.1. Optimization of benchtop synthesis 85
5.4.1.1. Temperature 85
5.4.1.2. pH 87
5.4.2. Optimization of conventional microwave synthesis 92

5.4.2.1. pH 92
5.4.2.2. Surfactants 93
5.4.3. Optimization of continuous flow capillary microwave synthesis 97
5.4.3.1. Microwave Wattage Settings 97
5.4.3.2. Resonance Time 99
5.4.3.3. Temperature 101
5.4.3.4. pH 102
5.4.3.5. Concentration of Metal Precursor 103
5.4.4. Optimal Conditions 105
5.4.5. Organic Removal 106
5.4.6. Hydrogenation of Octene 109
5.5. Conclusions 111
Chapter 6: Synthesis of Supported Platinum Nanoparticles onto Silica Star Supports 113
6.1. Overview and Motivation 113
6.2. Introduction 113
6.3. Experimental Methods 114
6.3.1. Incipient wetness of colloidal platinum nanoparticles onto silica star supports 114
6.3.2. Synthesizing platinum nanoparticles onto silica support using microwave irradiation 114
6.3.3. Characterization 115
6.4. Results and Discussion 115
6.4.1. Incipient wetness with colloidal platinum nanoparticles 115
6.4.2. Microwave synthesis of platinum nanoparticles onto silica star supports 116
6.4.2.1. Using hexanes as a co-solvent 121
6.4.2.2. Adding Ascorbic Acid in a Second Step 122
6.5. Conclusions 124
Chapter 7: Conclusions 126
List of References 129
Vita 138

List of Figures

Figure 1 % Savings with an increase in the core/particle ratio for several core materials[10] 4
Figure 2 Properties of nanoparticle catalysts that need to be considered when designing new catalysts 6
Figure 3 Proposed cycle of the Suzuki cross-coupling reaction 8
Figure 4 Proposed cycle of the Sonogashira cross-coupling reaction 9
Figure 5 Proposed cycle for the Heck cross-coupling reaction 11
Figure 6 Mechanism for the classical pathway for Fischer Tropsch Synthesis 13
Figure 7 Behavior of transition metals towards Fischer Tropsch synthesis[20] 14
Figure 8 Schematic of hydrogenation ethene to ethane on a heterogeneous catalyst 16
Figure 9 LaMer's model of nanoparticle nucleation and growth 18
Figure 10 Schematic for Nucleation and Growth of A. core/shell B. homogeneous nanoparticle C. heterogeneous nanoparticle 20
Figure 11 Suggested mechanism for the formation of gold nanoparticles using the Turkevich method[44] 24
Figure 12 Microwave heating mechanisms of a. dipolar polarization and b. ionic conduction mechanism[60] 26
Figure 13 The temperature profile after 60 seconds as affected by microwave irradiation (left) compared to treatment in an oil-bath (right). Temperature scale in Kelvin. '0' on the vertical scale indicates the position of the meniscus[64] 28
Figure 14 Schematic of Bragg diffraction 35
Figure 15 Interactions between electrons and a sample in electron microscopy 38
Figure 16 Schematic illustrating the creation of an X-ray from an electron source 40
Figure 17 Schematic of DLS instrument 42
Figure 18 Schematic diagram of a typical XPS spectrometer 43
Figure 19 Schematic illustrating the creation of an X-ray from the core from an X-ray source 44
Figure 20 Schematic diagram of VSM instrument 46
Figure 21 Schematic diagram of TGA instrument 47
Figure 22 Reaction scheme for wet synthesis of CuPd alloyed nanoparticles 50
Figure 23 TEM images of the CuPd nanoparticles 53
Figure 24 XRD pattern of as prepared CuPd nanoparticles 54
Figure 25 Binding energies of A. Pd 3d and B. Cu 2p 56
Figure 26 Schematic of Heck (Eq. 1) and Sonogashira (Eq. 2) coupling reactions with CuPd nanoparticles 60
Figure 27 Schematic of capillary microreactor set-up 64
Figure 28 Schematic of Fischer Tropsch reactor 66
Figure 29 XRD patterns of synthesized Cu@Ni, Cu@Co, and elemental Co, Ni, and Cu. 68

Figure 30 Bright Field TEM images of (a,b) Cu@Ni and (d,e) Cu@Co particles. EELS maps of (c) Cu@Ni and (f) Cu@ Co particles. 70
Figure 31 A. Room temperature hysteresis of Cu@Ni and Cu@Co particles B. M(T) curves of Cu@Ni and Cu@Co particles taken at 50 Oe 72
Figure 32 High Temperature XRD patterns for Cu@Ni particles collected from 200 °C to 700 °C 74
Figure 33 XRD spectra of synthesize Cu@M particles at 295 °C 75
Figure 34 Conversion of carbon monoxide versus reaction temperature. 76
Figure 35 XRD of Cu@Co and Cu@Ni nanocomposites after Fischer Tropsch catalytic testing 77
Figure 36 Hydrocarbon distribution as a function of carbon number. 78
Figure 37 Olefin/Paraffin ration for C2-C6. 79
Figure 38. Schematic of Continuous Flow Microwave Microreactor 83
Figure 39 Schematic of CSTR microwave reactor 84
Figure 40 XRD spectra of platinum nanoparticles synthesized at different temperatures 86
Figure 41 UV/VIS spectrum of K_2PtCl_4 solution before and after reduction 88
Figure 42 Flow UV/VIS of platinum nanoparticles synthesized at a pH of 5 89
Figure 43 Flow UV/VIS of platinum nanoparticles synthesized at a pH of 8 90
Figure 44 Flow UV/VIS of platinum nanoparticles synthesized at a pH of 10 91
Figure 45 Schematic of ascrobic acid at different pH values 92
Figure 46 TEM images of platinum nanoparticles synthesized with A. PVP K10. and B. PEG 2,000. 95
Figure 47 STEM images of platinum nanoparticles synthesized using conventional microwave 97
Figure 48 TEM images of platinum nanoparticles synthesized under a fixed wattage of 300 W 98
Figure 49 TEM images of platinum nanoparticles synthesized under dynamic wattage . 99
Figure 50 TEM image of platinum nanoparticles synthesized with a resonance time of 8 minutes 100
Figure 51 TEM images of platinum nanoparticles synthesized at A. 85 °C B. 90 °C and C. 95 °C 102
Figure 52 TEM images of platinum nanoparticles synthesized at a pH of A. 5.8 B 6.5, and C 9.1 103
Figure 53 TEM images of platinum nanoparticles synthesized with A 2.9 mM K_2PtCl_4 and B 7.6 mM K_2PtCl_4 105
Figure 54 TEM images of platinum nanoparticles synthesized with A 18 wt % and B 9 wt % PVP K10 106
Figure 55 TPO of platinum nanoparticles from 30-600 °C and then held at 600 °C for 1 hour 108
Figure 56 TPO of platinum nanoparticles from 30-600 °C and then held at 600 °C for 1 hour following the formation of NO_x with a mass of 30 108
Figure 57 XRD spectrum of platinum nanoparticles after TPO at 600 °C 109
Figure 58 Schematic of the hydrogenation of octene to octane 110

Figure 59 Uptake of H_2 as a function of time for platinum nanoparticles synthesized in microwave flow, benchtop conventional heating, and platinum using a CSTR microwave flow 110
Figure 60 Image of platinum on silica support synthesized with 0.5 minutes of microwave irradiation with a 30 minute prestir step 118
Figure 61 Image of cross section and full support of platinum on star support with PVP K10 present 119
Figure 62 EDX elemental mapping of platinum for the cross section of the silica star support synthesized with PVP K10..... 120
Figure 63 mage of cross section and full support of platinum on star support without PVP K10 present 120
Figure 64 EDX elemental mapping of platinum for the cross section of the silica star support synthesized without PVP K10 121
Figure 65 Image of silica stars in a solution of hexanes, DI water, and K_2PtCl_4 A. before microwave irradiation and B. After microwave irradiation..... 122
Figure 66 Cross section of A. reduced before microwave B. ascorbic acid added in a second step and microwaved 123
Figure 67 XPS of silica stars after loading platinum by A. reducing before microwave and B. ascorbic acid added as a second step and then microwaved 124

List of Tables

Table 1 Properties of common Fischer Tropsch catalysts 15
Table 2 Loss tangent values at 2.45 GHz and 20 °C of different solvents 27
Table 3 Types of flow reactors 31
Table 4 Characterization techniques used in this work 34
Table 5 Suzuki cross-coupling reactions using CuPd nanoparticles..... 57
Table 6 Recycling Experiment with CuPd nanoparticles 59
Table 7 Comparison of lattice parameters in Cu@Ni nanocomposites 68
Table 8 Crystallite size, hydrodynamic radius, and PDI values for platinum nanoparticles synthesized at different temperatures..... 87
Table 9 Reduction time from UV/VIS data at different pHs 91
Table 10 Hydrodynamic radius and PDI values for platinum nanoparticles synthesized at different pHs with microwave irradiation..... 93
Table 11 Hydrodynamic radius and PDI values of platinum nanoparticles synthesized with different surfactants with 18 wt% surfactant with microwave irradiation..... 94
Table 12 Hydrodynamic radius and PDI values of platinum nanoparticles synthesized with different amounts of PVP K10 with microwave irradiation 96
Table 13 Hydrodynamic radius and PDI values for platinum nanoparticles synthesized with different microwave settings..... 99
Table 14 Hydrodynamic radius and PDI values for platinum nanoparticles synthesized with different resonance times 100
Table 15 Hydrodynamic radius, PDI and TEM size data for platinum nanoparticles synthesized at various temperatures..... 101
Table 16 Hydrodynamic radius and PDI values for platinum nanoparticles synthesized at different pHs 103
Table 17 Hydrodynamic radius, PDI and TEM diameters of platinum nanoparticles synthesized at different mM of K_2PtCl_4..... 104
Table 18 Hydrodynamic radius, PDI, and TEM sizes of platinum nanoparticles synthesized with microwave flow..... 106
Table 19 Comparison of hydrogenation of octene using several platinum catalysts..... 111
Table 20 Wt % platinum onto support using incipient wetness method with and without hexanes..... 116
Table 21 Wt % platinum loaded onto the support at different reaction times 117
Table 22 Wt % of platinum on the support at different ratios of ascorbic acid and PVP K10..... 119
Table 23 Wt% platinum on support with ascorbic acid added as a second step..... 123

Abstract

SYNTHESIS AND CHARACTERIZATION OF METALLIC NANOPARTICLES FOR CATALYTIC APPLICATONS

Sarah Emily Smith

A dissertation in partial fulfillment of the requirements for the degree of Doctor of Philosophy at Virginia Commonwealth University

Virginia Commonwealth University, 2017

Director: Everett E. Carpenter

Department of Chemistry

In recent years, research has focused on reducing the cost of catalysts in a variety of ways including using less expensive materials, improving the synthetic method, and increasing the catalytic activity, recovery, and recyclability. Typically with nanoparticles, the size, shape, composition, and surface coating have an effect on catalytic activity.[1-2] In this work, we focused on reducing the cost of precious metal based catalysts by altering the synthetic methods.

One way to lower the cost of synthesizing precious metal nanoparticles is by debasing the precious metal with a second cheaper more abundant metal. CuPd nanoparticles were

synthesized in oleylamine and displayed catalytic activity in several cross-coupling reactions. Due to copper being present in the nanoparticle, a copper halide co-catalyst was not needed for Sonogashira cross coupling to be successful.[3] While this method produced reactive catalysts, low product yield hinders its application for industry.

Solution based synthesis of metallic nanoparticles typically require long reaction times and high temperatures, which make large scale production of nanoparticles on an industrial scale difficult.[4-5] The use of continuous flow microreactors provides greater control of synthetic parameters, leading to lower batch-to-batch variability and increasing the efficient of heat and mass transfer and have been applied to the synthesis of metals, semiconductors, zeolites, organic compounds, and semiconductors.[5-7] To compare continuous flow methods to benchtop reactions, a well-characterized benchtop reaction synthesizing Cu@Ni core/shell nanoparticles was successfully transferred to a flow reactor set-up. Cu@Ni nanoparticles were synthesized using a capillary microreactor in under 1 minute compared to the 1 hour reaction on benchtop with similar properties in a green solvent.[2] The Cu@Ni nanocomposites were active towards the Fischer Tropsch reaction.[8] 2 nm platinum nanoparticles and platinum bimetallic alloys were synthesized in water using a capillary microwave flow reactor. Investigations showed the nanoparticles were activity toward hydrogenation of octene.

With further development, continuous flow synthesis of metallic nanoparticles can be applied to the synthesis of a wide variety of catalysts on an industrial scale. Continuous flow methods provide greater control of reaction parameters, increased safety by reacting smaller volumes of chemicals at a given time, and decreasing the batch-to-batch variability.

Chapter 1: Introduction and Overview

1.1. Overview

Metallic nanoparticles can be synthesized in a variety of methods from dry and wet chemical synthesis. Due to their large surface area to volume ratio, nanoparticles exhibit interesting optical, catalytic, and magnetic properties.[9] Academic research has focused on developing new synthetic methods to control the size and shape of nanoparticles. However, most research does not translate well to industry for a variety of reasons.

Historically, organometallic complexes have been used as the catalyst of choice. However, organometallic complexes can be difficult to remove from solution after the reaction and can interact with the products. Nanoparticles have shown to be affective in catalyzing several reactions with the active sites being on the surface of the nanoparticle. To decrease the overall cost of the catalysts, synthesis of alloys, core/shell, and supported nanoparticles have been investigated. By selectively adding the active metal species as a shell on a filler metal as the core, the cost of the particle decreases as shown in Figure 1.[10]

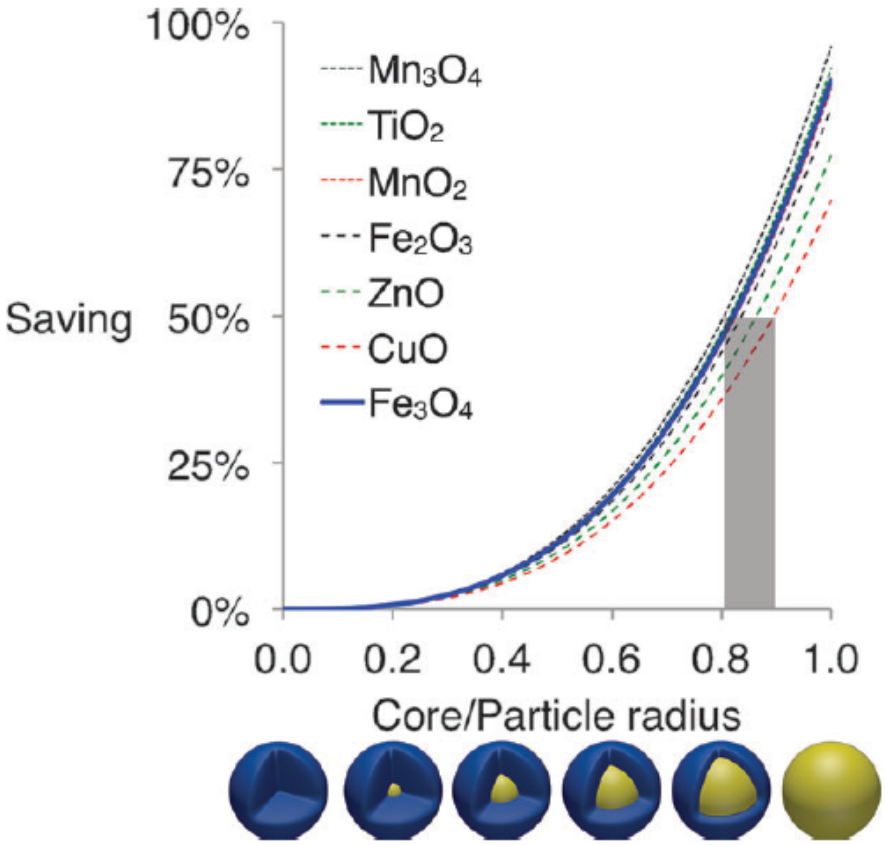

Figure 1 % Savings with an increase in the core/particle ratio for several core materials[10]

Most academic research synthesizes the products on a milligram scale, which is not large enough to move the new methods into industrial applications. To test nanoparticles for catalysis on an industrial scale, an average of 500 grams of catalyst is needed. Therefore, research has been investigating new large-scale synthetic methods. One research area focuses on using continuous flow methods. These methods have the capability for large-scale synthesis on an industrial scale.

1.2. Nanoparticle Catalysis

Nanoparticle catalysts are used during the synthesis of a variety of products such as medicines, chemicals, polymers, fibers, fuels, paints, lubricants and more.[11] Due to the large surface area to volume ratio, nanoparticles exhibit an increase in active sites with a decrease in size.

Catalysts can be divided into two categories, homogenous and heterogeneous catalysts. Homogenous catalysts are catalysts that are in the same phase as the reactants being catalyzed. These catalysts are generally organometallic complexes that are soluble in solution. Homogenous catalysts are known for their high selectivity, high yield, and activity. Most organometallic catalysts have electron donating ligands such triphenylphosphine. Due to the ligands, the catalyst can be difficult to remove because the ligands can interact with the product. Trace metal in the products, especially in the pharmaceutical industry can be detrimental.

Heterogeneous catalysts show great promise as future catalysts for a wide variety of reactions. Heterogeneous catalysts are catalysts that are in a different phase than the reactants. For solution-based reactions, a heterogeneous catalyst is commonly a supported nanoparticle. The supports can be metal oxides, carbon materials, or polymers. Compared to homogeneous catalysts, heterogeneous catalysts typically exhibit high stability and recyclability but lower catalytic activity and selectivity.[12] Heterogeneous catalysts are much easier to remove from solution than organometallic complexes using a filtering step. Some supported nanoparticles do show metal leaching into the solution. This can be remedied by making sure the nanoparticle is firmly bound to the support or by changing the support. Since the nanoparticle is supported, some of the active surface area is lost.

Unsupported nanoparticle catalysts do not meet the requirements of either category and can be classified as semiheterogenous.[13] Nanoparticles show similar catalytic activity to homogenous catalysts due their completely exposed surface. Since the nanoparticles are not soluble and are instead dispersed in the solvent, they are easier to recover similar to heterogeneous catalysts. If the nanoparticle is sufficiently small, then the nanoparticle can be considered a homogenous catalyst.

When designing new catalysts, there are many things to take into consideration and are shown in Figure 2. The chemical-physical properties, such as the surface area, porosity, composition, and morphology are controlled during the synthesis. These properties directly affect both the mechanical properties, such as the strength and attrition, and catalyst properties, such as the selectivity, activity, and stability.

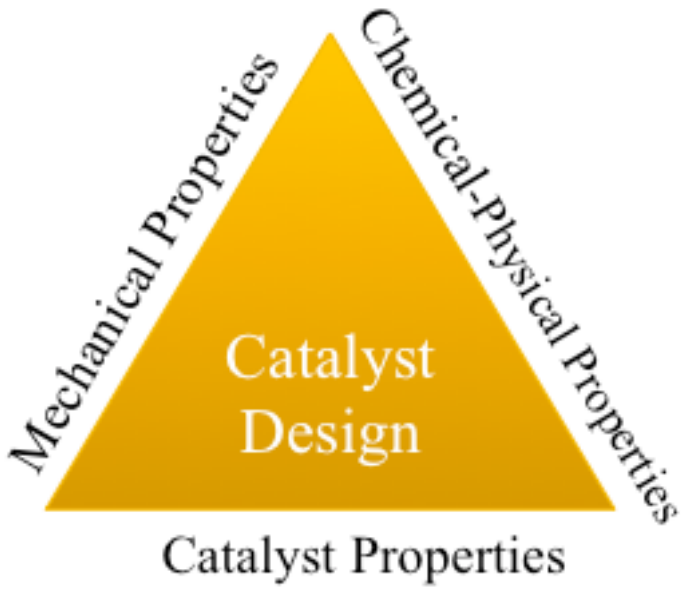

Figure 2 Properties of nanoparticle catalysts that need to be considered when designing new catalysts

1.2.1. Cross-coupling Reactions

1.2.1.1. Suzuki Cross-coupling Reaction

The Suzuki cross coupling reaction shown in Figure 3 was first published by Akia Suzuki in 1979 and affording him a share of the noble prize in chemistry in 2010 with Richard Heck and Ei-ichi Negishi.[14] This reaction is used to synthesize poly-olefins, styrenes and biphenyls by creating a carbon carbon bond between an organoboron and a halide. The reaction is commonly catalyzed by a Pd(0) catalyst. The first step of the reaction involves an oxidative addition changing the oxidation state of the palladium to Pd(II). In the next step of the cycle, the palladium exchanges its halide for a hydroxide group from the base present in the system. After this, a transmetallation step occurs between an activated boronic acid and the palladium species. Lastly, a reductive elimination step occurs regenerating the Pd(0) catalyst and leaving the biphenyl product.

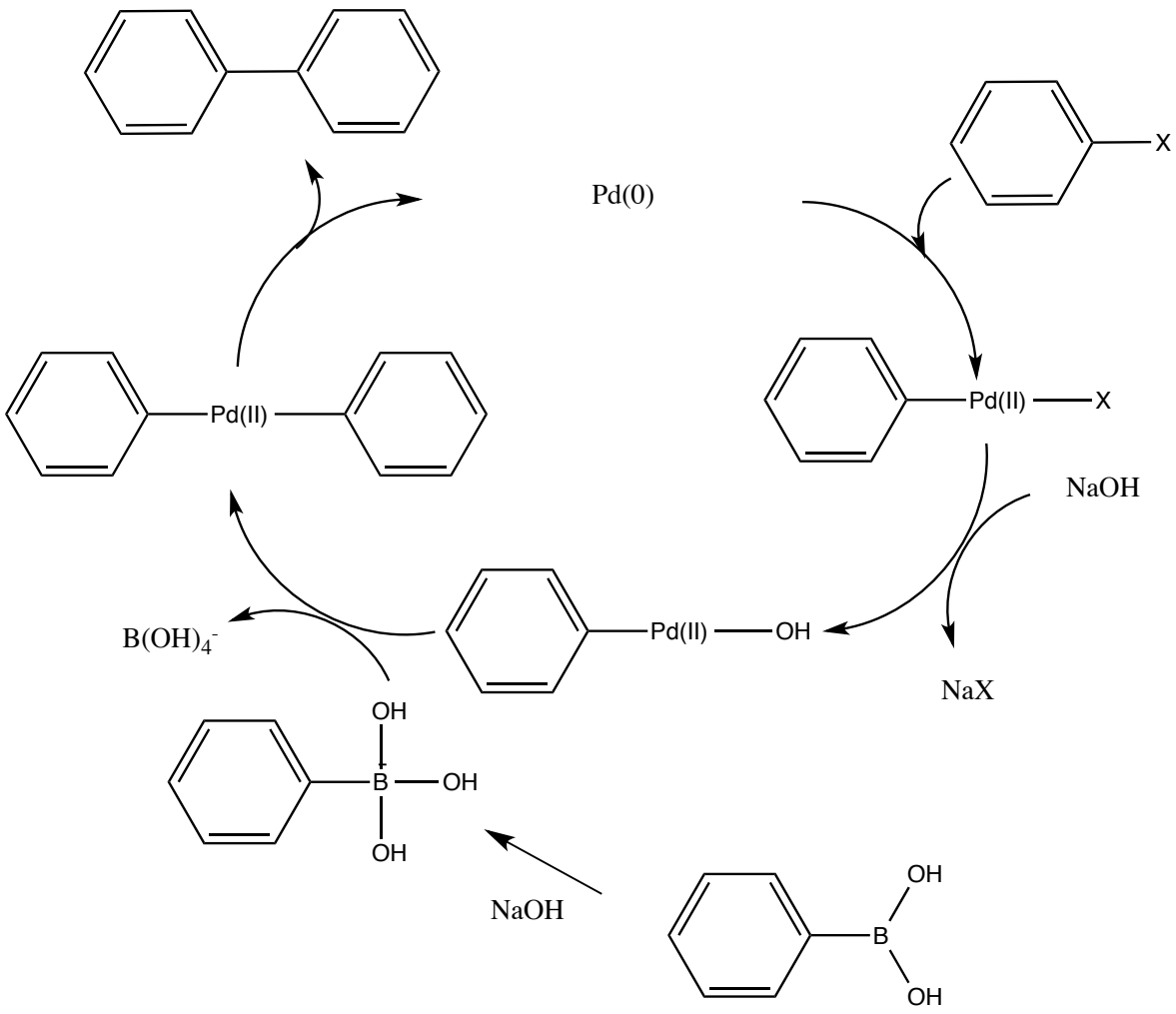

Figure 3 Proposed cycle of the Suzuki cross-coupling reaction

1.2.1.1.1. Common Catalysts

The Suzuki reaction commonly relies on an organometallic palladium complex as the catalyst. [15] The most common ligands are electron donating ligands such as phosphines.[16] Since ligands can interact with the product making recovery difficult, research has been focused on increasing the recoverability of the catalyst. [9,10] This can be done by either eliminating the need for the ligands or by putting the catalyst on a support.[15]

1.2.1.2. Songashira Reaction

The Sonogashira cross-coupling reaction shown in Figure 4 was first published in 1975 by Kenichi Sonogashira as a reaction that could form carbon carbon bonds between a terminal alkyne and either an aryl or vinyl halide with palladium and copper co-catalysts.[13] The first step of the cycle involves the palladium complex undergoing oxidative addition of the either the aryl or vinyl halide changing the oxidation state of the palladium to Pd(II). Next, the palladium species undergoes transmetallation with the activated alkyne species so it now contains copper on a terminal end. Then reductive elimination takes place regenerating the palladium catalyst and aryl alkynes.

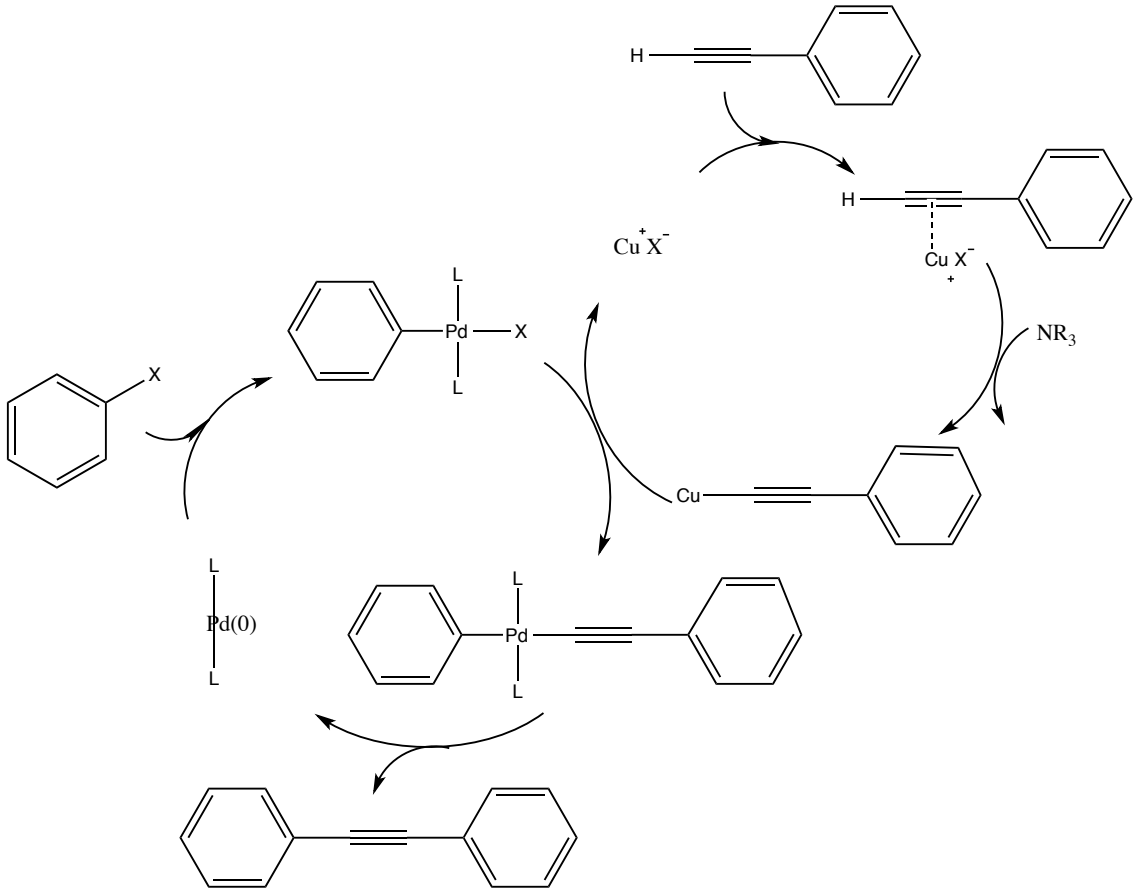

Figure 4 Proposed cycle of the Sonogashira cross-coupling reaction

1.2.1.2.1.Common Catalysts

The Sonogashira reaction historically relies on both a Pd(0) and a Cu(I) as co-catalysts for the reaction. It most commonly uses a palladium phosphine complex and a copper halide salt in relatively high amounts. In recent years, there has been a movement towards eliminating the need for the copper co catalyst because the copper is difficult to recover and can form impurities by reacting with the acetylides.[13] However, most copper free Sonogashira reactions add an excess of amine, which increases the negative environmental impact.[13] The ligands typically used for the reaction like with the Suzuki reaction make recovery difficult because they can interact with the product.

1.2.1.3. Heck Reaction

The first publication of the Heck reaction was in 1971 by Tsutomu Mizoroki and Richard Heck and earned Heck a share of the noble prize in chemistry in 2010.[14] The Heck reaction forms a carbon carbon bond between an alkene and an unsaturated halide using a palladium catalyst. The cycle is shown in Figure 5. In the first step, the $Pd(PPh_3)_3$ catalyst is subjected to oxidative addition of an aryl halide changing the oxidation state of the catalyst to Pd(II). Next the Pd(II) forms a π complex and completes an insertion step with the alkene followed by a β-hydride elimination. Lastly reductive elimination takes place.

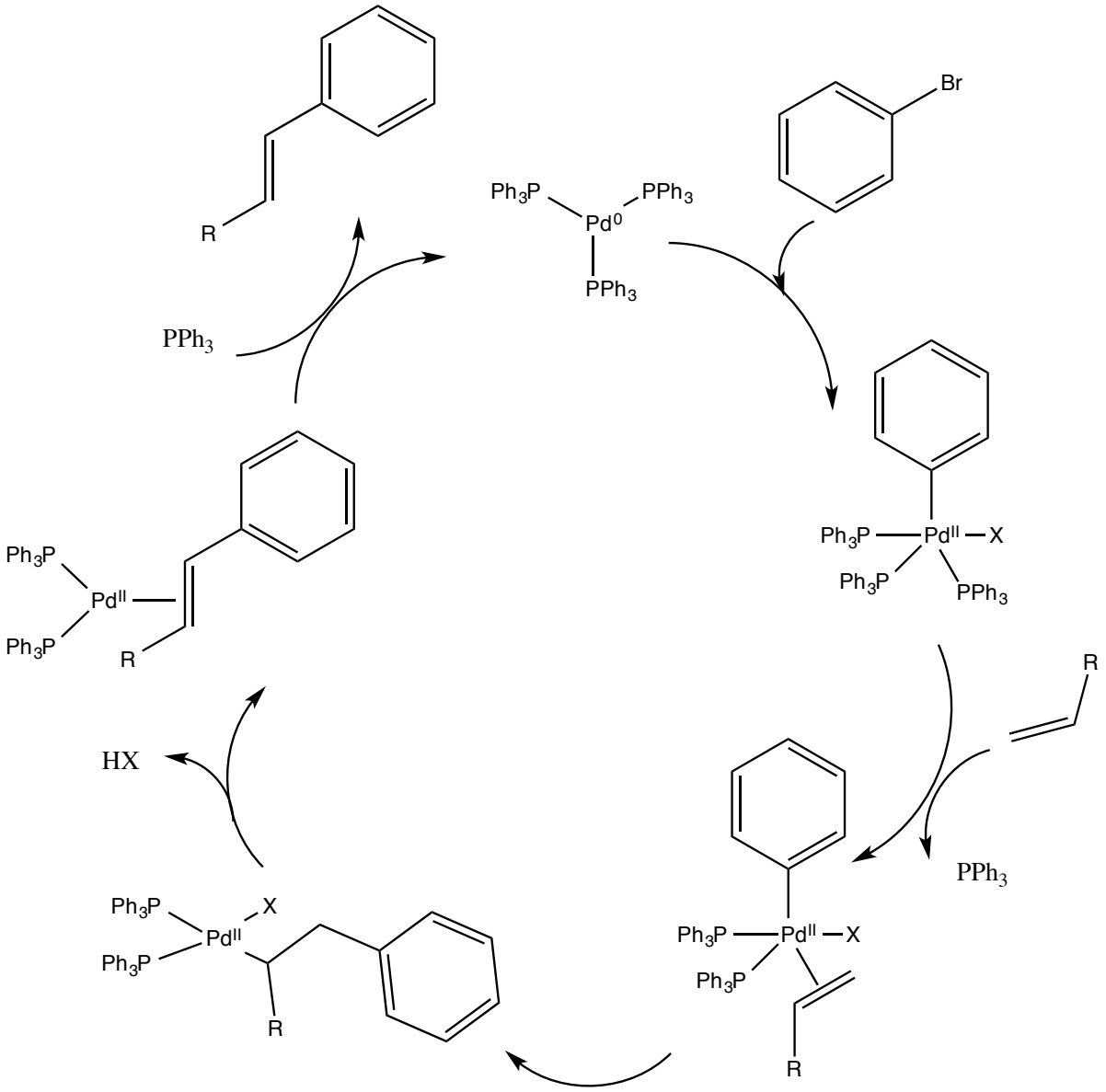

Figure 5 Proposed cycle for the Heck cross-coupling reaction

1.2.1.3.1. Common Catalysts

The Heck reaction historically has used an organometallic palladium complex as the catalyst. There has been a move to find new catalysts that would be cheaper such as using other transition metals such as nickel cobalt, and copper with electron donating ligands.[17-19] However,

like with the catalysts used for the Suzuki and Sonogashira reactions, the ligands make recovery difficult.

1.2.2. Fischer Tropsch Synthesis

The Fischer Tropsch synthesis was discovered by Franz Fischer and Hans Tropsch in 1923 in Germany. During World War II, the Fischer Tropsch reaction gave Germany the process to turn coal into hydrocarbon liquid fuel needed for war efforts.

The Fischer Tropsch synthesis synthesizes hydrocarbons from a mixture of carbon monoxide and hydrogen gas with the reaction:

$$(2n+1)\ H_2 + nCO \rightarrow C_n H_{(2n+2)} + nH_2O,$$

where n is an integer. The chain length of the hydrocarbon can be selected based on the catalyst, reaction temperature, pressure, and the ratio of carbon monoxide to hydrogen gas. The Fischer Tropsch synthesis can also produce olefins following the reaction:

$$2nH_2 + nCO \rightarrow C_n H_{2n} + nH_2O,$$

where n is an integer. A third reaction that can take place is the water-gas shift reaction:

$$CO + H_2O \rightarrow CO_2 + H_2$$

The water-gas shift reaction can be used to alter the carbon monoxide to hydrogen ratio, which can affect the selectivity for the hydrocarbon produced.

The mechanism for Fischer Tropsch synthesis has been the focus of research for many years. It can most commonly be explained as a polymerization reaction and is shown in Figure 6.[20] In the initiation step, carbon monoxide and hydrogen are absorbed onto the surface of the metal catalyst and dissociate. The dissociated hydrogen then inserts into the carbon-metal species, forming CH_2, which is needed for the propagation step. During propagation, the carbon

chain grows until the chain desorbs from the metal catalyst surface. The exact mechanism of this step is not fully understood and still under debate among researchers.

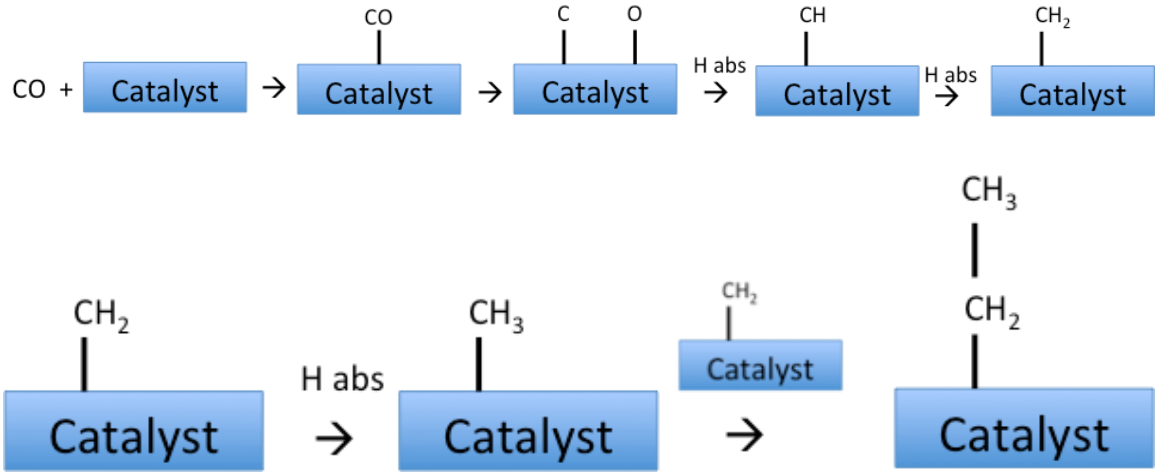

Figure 6 Mechanism for the classical pathway for Fischer Tropsch Synthesis

1.2.2.1. Common Catalysts

The most significant parameter for Fischer Tropsch synthesis is the catalyst. In order to be a successful for Fischer Tropsch, the catalyst needs to be able to adsorb and dissociate both carbon monoxide and hydrogen gas. The catalyst should also be easily reducible. Figure 7 shows the behavior of various transition metals.[20] Based on this criteria, nickel, cobalt, iron, ruthenium, rhenium, and osmium are the best choices for a catalyst.

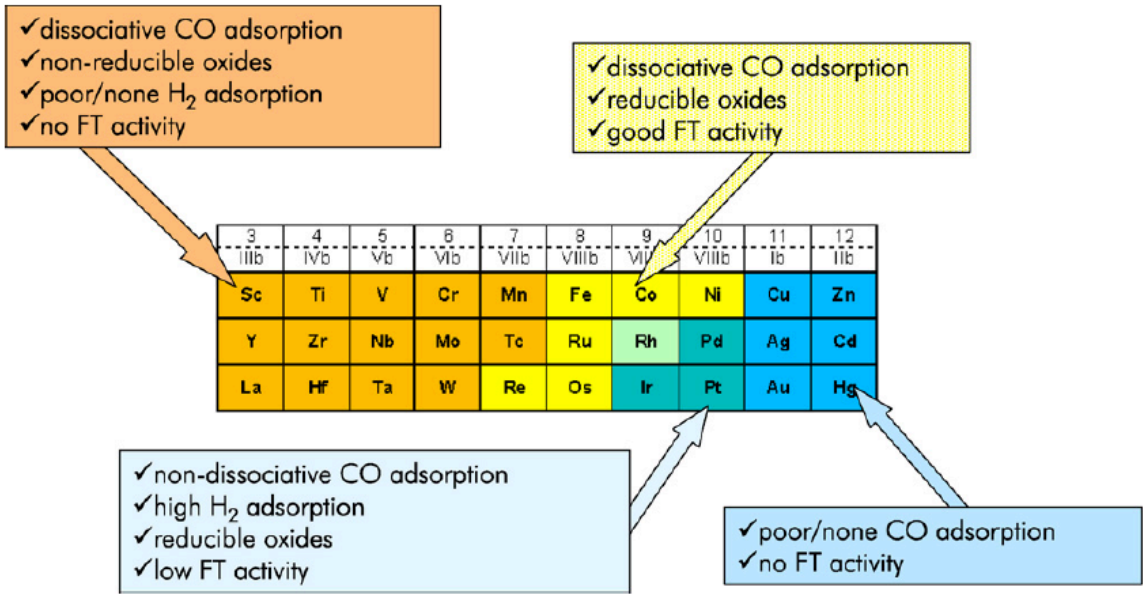

Figure 7 Behavior of transition metals towards Fischer Tropsch synthesis[20]

The most commonly used catalysts for Fischer Tropsch are iron, cobalt, nickel, and ruthenium. Although the most active catalyst and more selective for high molecular weight hydrocarbons, the price of ruthenium makes it not feasible to use on an industrial scale. Nickel is also not used much because it is selective for methane formation due to its high hydrogenation activity.[21] Iron based catalysts are the cheapest, more abundant catalysts used for Fischer Tropsch synthesis. Iron catalyst have high activity for the water gas shift reaction, which makes it catalytically active in a wider range of CO:H_2 ratios specifically when the ratio is low. This means that iron catalysts are suitable when biomass or coal is used as the feed source.[21] Iron catalysts are more selective for the formation of olefins over parafins. However, iron catalysts are subject to poisoning from sulfur and oxygen and are easily deactivated. Cobalt catalysts are usually the catalyst of choice for Fischer Tropsch. Compared to iron, cobalt catalysts are less active for the water gas shift reactions, meaning that a higher ratio of CO:H_2 is needed for synthesis to take place. It is most active when natural gas is used as the feed source. Cobalt

catalysts are more selective for the formation of parafins over olefins. Compared to iron, cobalt is also more chemically inert and harder to deactivate and have a longer lifetime.

Table 1 Properties of common Fischer Tropsch catalysts

Catalyst	Selective	Temperature range most active (°C)	Other Notes
Iron	olefins	330-350	Water gas shift reaction active
Cobalt	parafins	220-270	Not water gas shift active
Nickel	methane	-	-
Ruthenium	-	-	Very expensive

Many promoters have been tested with Fischer Tropsch catalysts including metal oxides, transition metals, and alkali metals.[21-22] The main role of promoters is to enhance the reducibility of the catalyst increasing the number of active sites. In most cases, the metal catalyst is on an oxide support.[23] With some promoters such as copper or potassium, the activity for the water gas shift reaction is increased, making the catalyst able to adjust the ratio of CO and H_2.[22]

1.2.3. Hydrogenation Reactions

Hydrogenation reactions are a broad area of catalysis. Hydrogenation reactions can most simply be described as the reduction of a double or triple bond in hydrocarbons with the addition of hydrogen atoms. The hydrogen source can be hydrogen gas, another molecule such as diazene, or from an electrochemical reaction.

Hydrogenation takes place on the surface of the catalyst. In the first step, hydrogen is absorbed to the surface of the catalyst and dissociated forming metal hydrogen bonds. The alkene also absorbs to the surface of the catalyst. The two absorbed hydrogen atoms transfer to

the alkene in a syn addition forming the alkane product. A schematic of this process is shown in Figure 8.

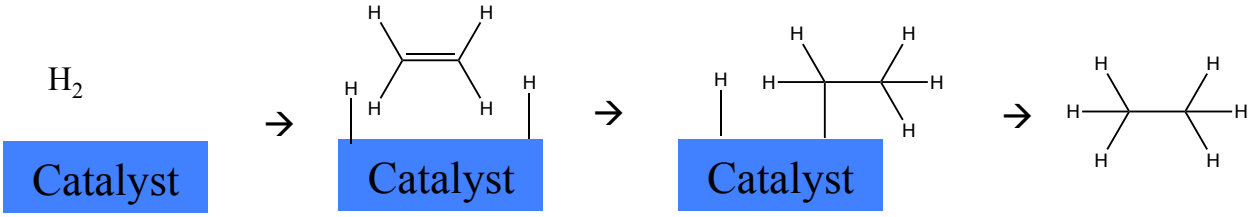

Figure 8 Schematic of hydrogenation ethene to ethane on a heterogeneous catalyst

1.2.3.1.Common Catalysts

Both heterogeneous and homogeneous catalysts can catalyze hydrogenation reactions. The appropriate catalyst depends on the substrate and desired product. The metal must be able to adsorb and dissociate hydrogen well. A wide selection of transition metals has been used for hydrogenation reactions with a large amount of research completed with noble metal catalysts. Platinum and palladium display good catalytic activity towards several hydrogenation reactions with the activity being dependent on the size and shape of the nanoparticle.[2, 24-28, 29] In this work, the focus will be on heterogeneous platinum catalysts.

1.3. Nucleation and Growth

Classical nucleation theory is described as a kinetic model of cluster formation and growth that involves only one step. The theory is based on the work by Volmer, Gibbs, and Becker. Classical nucleation theory states that primary building blocks, or monomers, form clusters that can either can dissolve back into the system or form stable clusters. If the clusters reach a critical size, then addition of lattice energy is larger than the energy loss from the change in surface energy and the particle can grow.

One of the first accepted theories on crystallization was in 1897 by Friedrich Wilhelm Ostwald. In his theory Ostwald's rule of stages, he stated that crystallization usually took place in stages. The first stages typically are the kinetic products that closely resemble the initial states. The final stage is the more thermodynamically favored product.

In 1950, Victor Kuhn LaMer published a new theory on crystallization and is shown in Figure 9.[30] LaMer's theory describes crystallization as taking place in three steps. In the first step, the concentration of monomers is increased until supersaturation is reached. In the case of metallic nanoparticles, the monomer is reduced metal species. Once the critical concentration is met, nucleation occurs of stable nuclei starting the second step. As nucleation takes place, the concentration of monomers decreases rapidly. Once the concentration is below the supersaturation limit, step three begins. In step three, growth of the particle takes place following Ostwald's ripening and diffusion. The smaller nuclei and particles have a much higher surface energy and will form larger particles to reduce the surface energy or will dissolve into solution.[30-32] When nucleation and growth take place simultaneously, the resulting nanoparticles have a wide size distribution and are polydisperse.[31] When nucleation and growth occur as two separate stages, the resulting nanoparticles have small size distributions and appear relatively monodisperse.[31] This process can be described as burst nucleation.

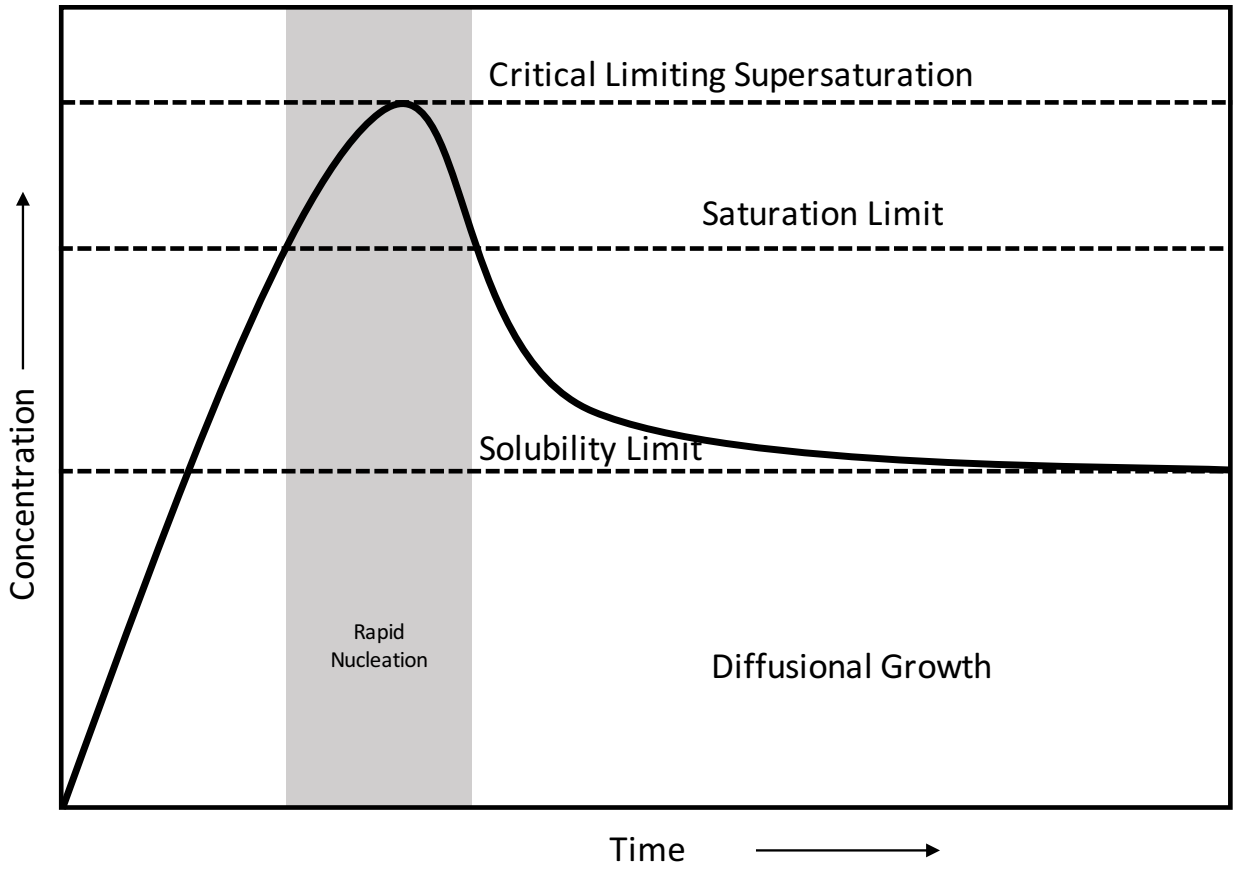

Figure 9 LaMer's model of nanoparticle nucleation and growth

There are a few modifications to classical nucleation theory that need to be made. Classical nucleation theory assumes that formed nuclei exist in the same crystal phase as the final product after nucleation and growth has finished. This theory ignores that different products are favored depending on thermodynamic and kinetic conditions. Classical nucleation theory also assumes that only one step is needed during nucleation and that all nuclei are spherical because they have the lowest surface energy. Recently, it has been found that not all nuclei are spherical and some are hexagonal.

Nucleation can occur both homogeneously and heterogeneously. In homogeneous nucleation, nucleation takes place if the overall Gibbs free energy is negative. The energy for the

formation of the bond has to be larger than the surface energy in order for nucleation to take place. Heterogeneous nucleation occurs when nucleation takes place on a surface. At the surface, the surface energy is lowered, lowering the activation energy needed for nucleation. Heterogeneous nucleation occurs during seed mediated synthesis and when nanoparticles are grown onto a support. In nanoparticle synthesis, both types of nucleation occur. [9]

1.3.1.Bimetallic Nanoparticle Synthesis

As the number of different metals increases, the complexity of the nucleation and growth processes also increases. The possibility of heterogeneous nanoparticles greatly increases. The resulting nanoparticles can be homogenous alloys, heterogeneous nanoparticles, or have a core/shell morphology.

LaMer's model can be used to explain how each of the different types of particles can be made in terms of the nucleation and growth. Depending on the rate at which the supersaturation level is met for each metal present, a different type of nanoparticle will be made.[31] If the nucleation and growth are completely separated of each metal like in A of Figure 10, a core shell nanoparticle will be synthesized. The second metal to nucleation will nucleate on the first metal following the process of heterogeneous nucleation. If both metals reach their individual supersaturation levels simultaneously and grow together, a homogeneous particle will be seen like in B of Figure 10. If the nucleation of one metal overlaps with the growth of the other metal, a heterogeneous particle with a possible gradient will be synthesized. The process is described in C of Figure 10. The rate at which the metals reach their individual supersaturation levels can be controlled by the choice of precursors.

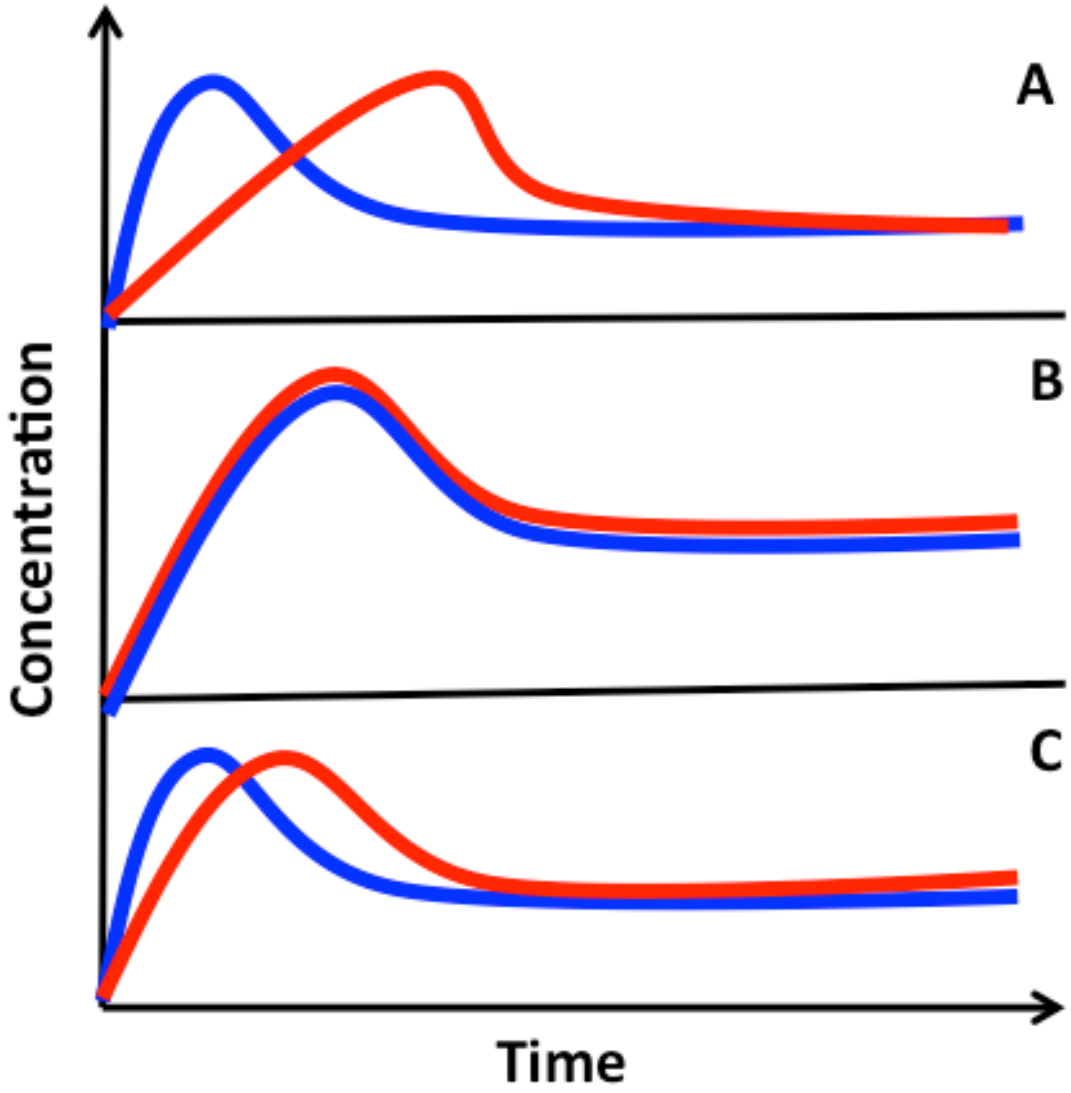

Figure 10 Schematic for Nucleation and Growth of A. core/shell B. homogeneous nanoparticle C. heterogeneous nanoparticle

1.3.1.1.Choice of Precursor

To control the nucleation of the metals, the interaction and stability of the metal complex needs to be considered. The bond strength between the metal and its ligands and the reduction potential of the metal play a role into the stability of the complex. Hard acid soft base theory by Pearson can be used to discuss the strength of the metal to ligand bonds.[33] In this theory, metals

and bases are divided into two categories; hard and soft. Hard acids and bases are metals and ligands that have a high charge density and are polarizing agents. Soft acids and bases are the metals and ligands that have low charge densities and are polarizable. In general, hard acids prefer hard bases where the bond is ionic in character and soft acids prefer to bind with soft bases where the bond is covalent in character. The strength of the metal to ligand bond determines when the complex will dissociate and be able to form the reactive monomer. For a rapid nucleation event, a weak metal to ligand bond is favorable because it increases the concentration of the active species.[31] A stronger bond would require more time and energy to break the complex to form the active species for nucleation and would lead to a slow nucleation event.[31] By choosing precursors based on the bond strength between the metal and ligand, the type of nanoparticle can be controlled.

The reduction potentials can also play a role in terms of determining the morphology and composition of the bimetallic nanoparticle. In most reactions, the metal precursors have a positive charge on the metal that is reduced to a neutral oxidation state to form the active species monomer needed for nucleation to take place. If both metal complexes dissociate at the same time, the metal with the lower reduction potential will reduce first making the active species and will reach supersaturation faster then the other metal.

1.4. Conventional Synthesis Methods

1.4.1. Polyol Method

The polyol method was first published in 1989.[34] In this method, a polyhydric alcohol acts as the reducing agent, surfactant, and solvent. Many different polyols have been used such as 1,2 diols, ethylene, and polyethylene glycols. In a typical experiment, metal salts and a base

are dissolved in the polyol and brought to reflux at temperatures between 200-320 °C for an extended period of time. The reduction potential of the polyol is controlled by the identity of the polyol, reflux temperature, and base concentration. The base is added to help facilitate the reduction of the metal. The base helps deprotonate the glycol making it a better stabilizing agent. It has also been shown that the metal can complex with the polyol by going through a ligand exchange.[35] The chelating to the polyol helps control nucleation and growth of the nanoparticle. The polyol method is known for synthesizing uniform size and shape nanoparticles with a low degree of agglomeration.[36]

The first study synthesized elemental copper, nickel, and cobalt from metal hydroxides, oxides, and acetate salts in ethylene and diethlyene glycol.[34] In this study, the resulting nanoparticles were large with diameters on the micron scale. Since the first studies utilizing the polyol method, it has been used to synthesize a wide variety of nanomaterials such as metals, oxides and chalcogenides. Nanoparticles on the nanometer scale with controlled shapes can now be synthesized. The polyol method is easily applied to the synthesis of noble metals such as ruthenium, platinum, silver, and gold of various sizes and shapes due to reducing power of the polyol.[36-38] Recently, it has been shown that the shape of copper could be controlled by the choice of polyol and if the reaction was run under reflux or distillation.[39] The synthesis of less-noble metals and transitions metals proved to be more difficult due to the lower electrochemical potential of the metal.[36] To overcome this, some research has focused on a seed mediated synthesis using a noble metal as the seed. [40-41]

1.4.2. Turkevich Method

Noble metal nanoparticles have been extensively studied due to their interesting optical and catalytic properties. By controlling the size and shape of certain metal nanoparticles, the surface plasmon resonance can be controlled.[42] One of the first methods for synthesizing noble metal nanoparticles in an aqueous system was developed by Turkevich in 1951.[43] In this method, gold colloidal nanoparticles are synthesized by adding sodium citrate to a boiling solution of $HAuCl_4$ in water where the sodium citrate as both reducing agent and surfactant.[43] This method allows for the synthesis of quasi-spherical gold nanoparticles in the size range of 12-16 nm. The synthesis of larger gold nanoparticles would allow for better tuning of the surface plasmon and allow for a wider range of applications.

The mechanism for the formation of gold nanoparticles using the Turkevich method has been well studied. Research has shown that the Turkevich method as a seed mediated process. Gold nanoparticles with a diameter of at least 1.5 nm are formed first. The gold ions still in solution form an electronic double layer surrounding the formed particles and grow onto the already formed nanoparticles in a two step process.[44] This two-step growth process is what leads to monodisperse nanoparticles. A schematic of this process is shown in Figure 11. The number of nanoparticles synthesized is determined based on the number of seed particles synthesized in the second step.

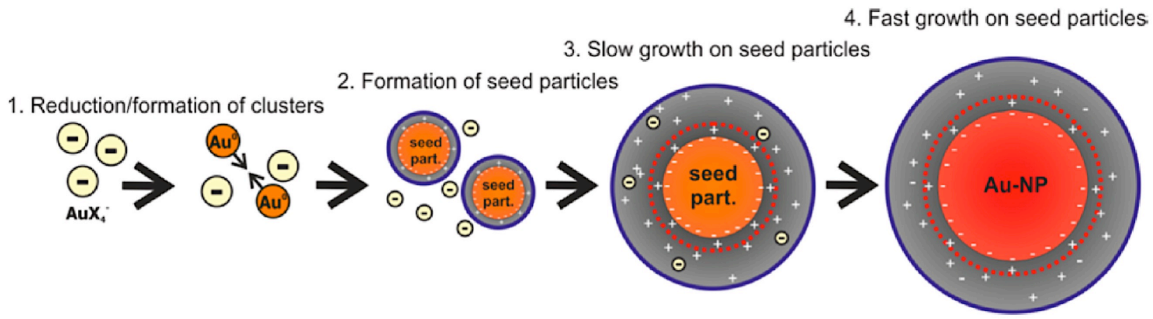

Figure 11 Suggested mechanism for the formation of gold nanoparticles using the Turkevich method[44]

In 1973, Frens refined the Turkevich method by examining the ratio of $HAuCl_4$ to citrate.[45] By doing this, he was able to control the size of gold nanoparticles from 16 nm to 147 nm. However, when the particles were larger then 40 nm, the size distribution broadened. Since the pioneering work by Turkevich and Frens, much research has been completed with the goal of controlling the size of the gold nanoparticles.[42, 45-49] Xia *et al.* controlled the size of gold nanoparticles from 2-330 nm.[42] To obtain the larger sizes, tris(hydroxymethyl) aminomethane was used as a second stabilizer and was premixed to obtain sizes between 40-95 nm.[42] pH has also been shown to help control the size of gold nanoparticles at elevated and room temperature reactions.[49]

The Turkevich method has been applied to the synthesis of silver nanoparticles.[50-51] However, the method did not transfer well to using different metals without adjusting the reaction. With silver, the nanoparticles were larger and more polydisperse compared to gold nanoparticles synthesized in the same manner. It has been suggested that with silver, the formation of stable seed particles does not take place. [44] With the addition of ammonia after nucleation has taken place, the synthesized silver nanoparticles are much smaller and more monodisperse by forming silver (I) complexes that act similarly to the electronic double layer during the synthesis of gold.[51] Using the work of Turkevich as a base, this method has been

altered to synthesize larger gold nanoparticles and other noble metals by adding ascorbic acid.[47] In these reactions, ascorbic acid acts as a reducing agent with citrate acting as a stabilizer. Platinum nanoparticles with diameters of 29-107 nm were synthesized using a modified Turkevich method.[52] Silver nanoparticles have also been synthesized using ascorbic acid and citrate with diameters of 30-72 nm.[53]

1.5.Microwave Synthesis

Microwave heating was discovered in 1945 by Percy LaBaron Spencer by having a chocolate bar melt while working with microwaves for radar applications.[54] The first published papers using microwave heating were published in 1986 for organic synthesis.[55-56] Microwave heating has now been applied to both organic and inorganic syntheses including in the synthesis of metal nanostructures and colloidal nanoparticles.

Microwave heating relies on the ability of a material to absorb electromagnetic radiation and convert it to heat by molecular rotations.[57] Polar molecules generate heat from friction, rotation, and collisions, while quickly orienting with a rapidly changing external electric field as shown in Figure 12. The other main mechanism shown also in Figure 12 relies on ions in solution that will orient with the electric field based on the difference in charges causing friction and collisions with other molecules. Most microwaves operate at 2.45 GHz (12.24 cm), which is the optimal frequency for rotation of polar molecules to be slightly slower then the electric field oscillations to generate heat. This frequency is only 1.2×10^{-6} eV which is lower then the energy needed to break chemical bonds.[58] At higher and lower frequencies, the polar molecules do not have enough time to orient themselves with the electric field before the electric field is changed.[59]

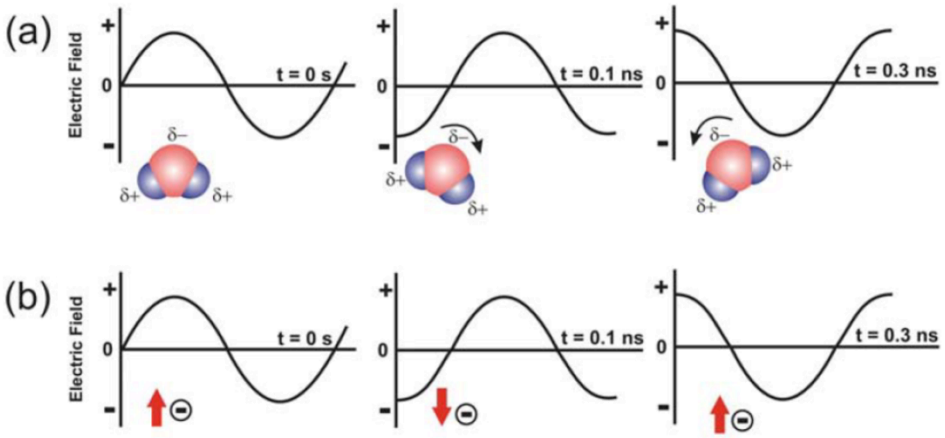

Figure 12 Microwave heating mechanisms of a. dipolar polarization and b. ionic conduction mechanism[60]

The ability of a material to generate heat with microwave irradiation is based on the materials dielectric loss and dielectric constant. The dielectric loss is described as the efficiency with which electromagnetic radiation is converted into heat.[59] the dielectric constant is defined as the ability of the material to be polarized by an electric field. The ability of microwave heating at a given temperature and frequency is described by the loss tangent.

$$\tan \delta = \frac{\delta''}{\delta'},$$

where δ'' is dielectric loss and δ' is the dielectric constant. The loss tangent is used to determine the penetration depth of the microwaves into the solution. The higher the value of the loss tangent, the shorter the penetration depth of the electromagnetic field. Table 2 shows loss tangent values of common solvents at 2.45 GHz and 20 °C. Some materials are more sensitive to microwave heating, creating regions of higher heating, or localized heating.[61-62] The hot spots are created most commonly by differences in dielectric properties of materials in the reaction.[63]

Table 2 Loss tangent values at 2.45 GHz and 20 °C of different solvents

Solvent	Boiling point (°C)	tan δ
ethylene glycol	198	1.350
ethanol	78	0.941
2-proponal	82	0.799
methanol	65	0.659
1,2-dichlorobenzene	180	0.280
N-methyl-2-pyrrolidone	202	0.275
acetic acid	118	0.174
N,N-dimethylformamide	153	0.161
1,2-dichloroethane	84	0.127
water	100	0.123
chlorobenzene	131	0.101
acetone	56	0.054
tetrahydrofuran	66	0.047
dichloromethane	39	0.042
toluene	111	0.040
hexane	68	0.020

One of largest advantages microwave heating provides compared to conventional heating methods such as oil baths or hot plates is a more uniform heating. Figure 13 shows the comparison of temperature profiles after 1 minute of heating by microwave or oil bath.[64] The temperature profile from microwave heating shows that the center of the solution is hotter then the edges and is relatively uniform throughout the solution. This is because the entire solution is

heated simultaneously internally. The temperature profile also shows that the temperature of the solution is more uniform then that of the solution heated with the oil bath. The solution heated with an oil bath shows a much larger temperature gradient because it relies on convention currents and thermal conductivity for heating the solution.[65]

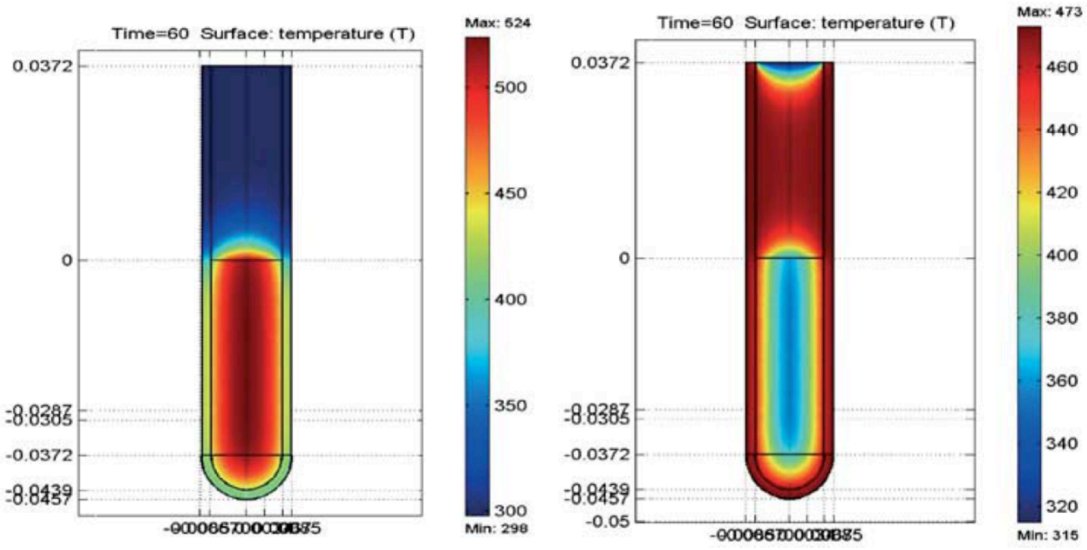

Figure 13 The temperature profile after 60 seconds as affected by microwave irradiation (left) compared to treatment in an oil-bath (right). Temperature scale in Kelvin. '0' on the vertical scale indicates the position of the meniscus[64]

Another advantage of microwave heating is that it can alter the kinetics of a reaction. In terms of inorganic synthesis, microwave heating has been shown to accelerate both nucleation and growth stages and is dependent on microwave power, vessel size, concentration of precursors, and microwave cavity design.[66] The overall reaction rate is also increased due to the steep temperature heating ramp.[67] The fast temperature ramp to higher temperatures has also been shown to increase the crystallinity of synthesized nanomaterials.[67] Microwave heating has also been shown to reduce the number of side reactions and improve product yields.[65] Irradiation time also can affect the nanoparticle size and shape.[68]

1.5.1. Microwave Synthesis of Inorganic Materials

One of the first groups to use microwave synthesis of inorganic materials was Komarnei's group. They published on the microwave synthesis of several metal oxides using a polyol method that including TiO_2, ZrO_2, and Fe_2O_3 in 1992.[69] This group then expanded into the synthesis of cobalt, copper, nickel, and silver in 1995.[70] Since this pioneering work, microwave synthesis has expanding and used for the synthesis of metal oxides, sulfides, selenides, tellurides, chalcogenides, and metal nanoparticles in water, ionic liquids, polyols, and mixed solvent systems.[54, 65, 71-76]

1.6.Flow Chemistry

In recent years, size and shape control of metal nanoparticles has been achieved in academic studies. However, this work is not easily applied to industrial applications mostly due to small sample sizes produced using academic synthesis methods.[77] To increase the amount of product formed, benchtop reactions could be run at larger volumes. The larger volume would change the temperature ramps and increase the batch to batch variability.[77] Another option would be to decrease the volume of the reaction and use continuous flow methods to synthesize the product. Flow chemistry can most simply be described as the continuous flow of one or more precursor solutions to a mixing point and reaction zone with the product being continuous collected.

Continuous flow reactor synthesis has many advantages over conventional benchtop synthesis methods mostly due to increased control over mixing, temperature, and rate of addition of precursors.[78] At any given time of the reaction, very little solution is in the reaction zone. This leads to increase in safety especially if the reaction is exothermic or precursors are hazardous.[5, 79] Flow reactors use less reagent volume, which can be advantageous when used to gather chemical

information about a reaction.[80] The large surface area to volume ratio of the reactors allows for an increase in heat transfer.[5, 78] The increase in heat transfer leads to faster reaction rates and more uniform heating compared to reactions run by conventional methods. Flow reactors can also have more efficient mixing depending on the design of the reactor.[5] Scale-up of reactions by continuous flow can be achieved by either increasing the volume of precursor solution or by running more reactors in parallel.[80]

There are some disadvantages to using continuous flow reactors. One disadvantage that can be difficult to overcome is clogging in the reactor. Depending on the reactor, cross-contamination can be difficult to control. Cross contamination can be decreased by modifying the surface of the reactor walls.[6]

There are many different reactor designs that can help overcome some of these disadvantages. Reactors are typically characterized based on the phase of the reactants and some common ones are listed in Table 3. The choice of reactor limits what kind of reaction can be completed. In this work, two capillary flow reactors are used to synthesize nanomaterials.

Table 3 Types of flow reactors

Reactor Type	Phases
capillary	liquid
coaxial	liquid
microchannel	liquid
droplet	liquid, gas
emulsion	liquid
packed bed	Solid, liquid, gas
Pulsed flow	liquid

1.6.1. Continuous Flow Synthesis of Inorganic Materials

One of the first reports of nanoparticles synthesized using a microreactor was in 2005 with the synthesis of gold nanoparticles using a modified Turkevich method.[6] A similar method synthesized gold nanoparticles between 4-15 nm were synthesized using a single mode microwave flow reactor with a modified Turkevich method in 90 seconds.[81] Continuous flow reactors have been used to synthesize a wide range of nanomaterials including metals, metal oxides, semiconductors, zeolites, and organic reactions.[5-7, 79] For multistep reactions, microreactors with multiple heat and sample inlet zones have been made.[82] Flow methods have also been used to synthesize supported nanoparticles.[83] Using a pulsed-flow supercritical reactor, 4-5 nm platinum nanoparticles were synthesized onto carbon.[83]

1.7.Summary of Objectives

In this dissertation, the overall goal is to reduce the cost of metal nanoparticle catalysts by altering the composition and morphology of the nanoparticles, increasing the recyclability and

recovery of the catalysts, and by synthesizing the nanoparticles using continuous flow reactors. Some key objectives of this dissertation work are:

- Synthesizing a CuPd nanoparticle that can be used as a catalyst for cross coupling reactions. By synthesizing an alloyed nanoparticle, two metals are on the surface of the nanoparticle and are present for catalysis and can be used for several different reactions.

- The comparison of Cu@M (M= Ni , Co) nanocomposities synthesized using a capillary flow reactor to similar nanocomposities synthesized using conventional benchtop methods. The temperature stability of the core/shell morphology was determined and the catalytic activity towards Fischer Tropsch synthesis.

- The optimization of the synthesis of colloidal platinum nanoparticles synthesized using a continuous flow microwave reactor. The platinum nanoparticles were tested for the hydrogenation of octene.

- Investigating the synthesis of platinum nanoparticles onto silica supports using microwave irradiation.

Chapter 2: Characterization

2.1. Introduction

Nanoparticle applications rely heavily on the shape, size, and composition of the nanoparticles. The optical, physical, and magnetic properties can all be affected by differences in the morphology of the nanoparticle. Extensive characterization is essential to determine how the size, crystal phase, shape, and any surface layers of the nanoparticle alter the application. It can also reveal any impurities in a sample that could negatively effect the application. This chapter is dedicated to introducing characterization instrumentation and techniques used in this work.

Table 4 Characterization techniques used in this work

Technique	Advanced Techniques	Application
X-Ray diffraction (XRD)	• Elevated temperature XRD, • Sherrer analysis, • Reitveld refinement	• Crystal phase identity • Crystallite size • Temperature stability
Transmission Electron Microscopy (TEM)	• Electron energy loss spectroscopy (EELS)	• Particle size and shape <100 nm • Elemental mapping
Scanning Electron Microscopy (SEM)	• Energy dispersive spectroscopy	• Particle size and shape >50 nm • Elemental mapping >100 nm
Dynamic Light Scattering (DLS)	• Zetapotential	• Particle hydrodynamic size • Poly dispersion index
Vibrating Sample Magnetometry (VSM)	• Magnetization versus temperature	• Magnetic properties analysis
X-Ray Photoelectron Spectroscopy (XPS)	• Depth profile	• Identification of surface species • Oxidation states of surface species
Thermogravimetric Analysis (TGA)		• Thermal stability and associated changes in mass

2.2.X-Ray diffraction (XRD)

X-ray diffraction (XRD) is a very easy, versatile, non-destructive technique that can be used to determine crystal phase of a material. It utilizes an X-ray source, typically Cu with a wavelength of 1.5418 Å that is scanned across multiple angles against the sample. This type of analysis relies on the interactions of the incident x-ray with the sample using Braggs law:

$$2d \sin\theta = n\lambda,$$

where d is the lattice spacing between adjacent crystal planes, θ is the angle where interference takes place, and n is an integer value. A schematic showing Bragg diffraction is shown in Figure 14. If the interaction between the incident x-ray and sample is constructive and follows Braggs law, an increase in intensity is seen as a peak in the resulting diffractogram. The diffractogram is then compared to known standards with the largest library maintained by the International Center for Diffraction Data (ICDD). XRD is known as a bulk analysis method because the X-rays have a large penetration depth for most materials.

For this work, a PANalytical X-Pert Pro Materials Research Diffractometer was used operating at a current of 45 mA at an accelerating voltage of 40 kV. Samples were prepared by pressing the powders onto a low background holder. Data was analyzed using Highscore plus equipped with a JCPDS-ICDD database.

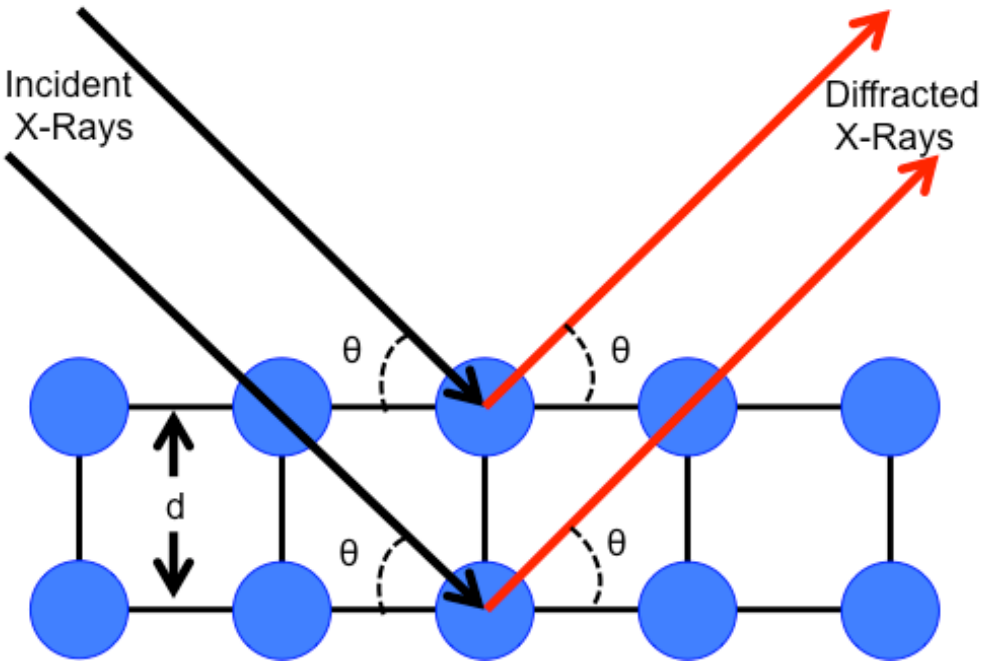

Figure 14 Schematic of Bragg diffraction

2.2.1.Scherrer Analysis

Based on Braggs law, each crystal plan should only have one lattice spacing value, d, for a perfect crystal. Therefore, the peaks in the diffractogram should have a width of zero. However, this is not the case experimentally most commonly due to size effects. Nanomaterials typically see an increase in peak broadening due to the decrease in crystal sizes. The relationship between the peak shape and the crystallite size of a material can be described using the Scherrer formula:

$$size = \frac{K\lambda}{FWHM \cos\theta},$$

where K is the Scherrer constant, λ is the wavelength of the incident x-rays, FWHM is the full width at the half maximum intensity, and θ is the angle corresponding to the diffraction. Due to the inverse relationship between crystallite size and peak width, Scherrer analysis is biased towards larger crystallite sizes.

2.2.2.Reitveld Analysis

To get a better idea of the ratio between phases present in a sample, Reitveld refinement can be applied. This technique uses a computer program to model the data by using the phase parameters such as the space group, lattice parameters, and atomic positions of the crystal structure. In this work, Reitveld Refinement was completed using X'Pert Highscore Plus and the lattice parameters were found in the Pearson Handbook of Lattice Spacings. By modeling the data, changes to the lattice parameters can be detected. If the changes are due to alloying between two species with the same crystal structure, Vegard's Law can be applied:

$$d_{ab} = (1 - x)a_A + x_{a_B},$$

where d_{ab} is the lattice parameter of the alloyed material, and a_A and a_B are the lattice parameters of the pure species before alloying. This can be used to determine the degree of alloying between the two species.

2.2.3.Elevated Temperature XRD (HTK-XRD)

In most cases, XRD is run under ambient temperature and air to determine crystal structure and crystallite size. However, crystal structure and crystallite size are dependent on temperature. An Anton Paar HTK1200N high temperature camera can be used to collect XRD spectra at temperatures between 25 °C and 1200 °C under various gases. This allows the study of changes to the material as temperature is changed. During the experiment, the height of the sample is changed to correct for thermal expansion of the sample at each temperature before a spectrum is collected.

2.3.Transmission Electron Microscopy (TEM)

One of the most useful instruments used to characterize nanomaterials is transmission electron microscopy (TEM). TEM is used to determine the size, shape, and size distribution of nanoparticles visually with high resolution. The TEM uses an electron beam that is directed to the sample. Based on how the electrons interact with the sample, a variety of information can be determined about the sample as shown in Figure 15.

Bright field imaging is the most commonly used TEM technique to determine size and shape of nanoparticles. In this case, the electron beam is passed through the sample. Based on the density of the sample, the electrons are able to pass through the sample in different amounts. In areas of more dense material, the resulting image appears darker since fewer electrons are able to pass through the sample. In areas of low density, the image appears lighter.

This work completed TEM work on a Zeiss LIBRA® 120 PLUS TEM. Samples were prepared by drying a drop of dilute sample suspending in hexanes, methanol, 1-propanol, or DI water onto a copper TEM grids. Image J software was used to analyze the images.

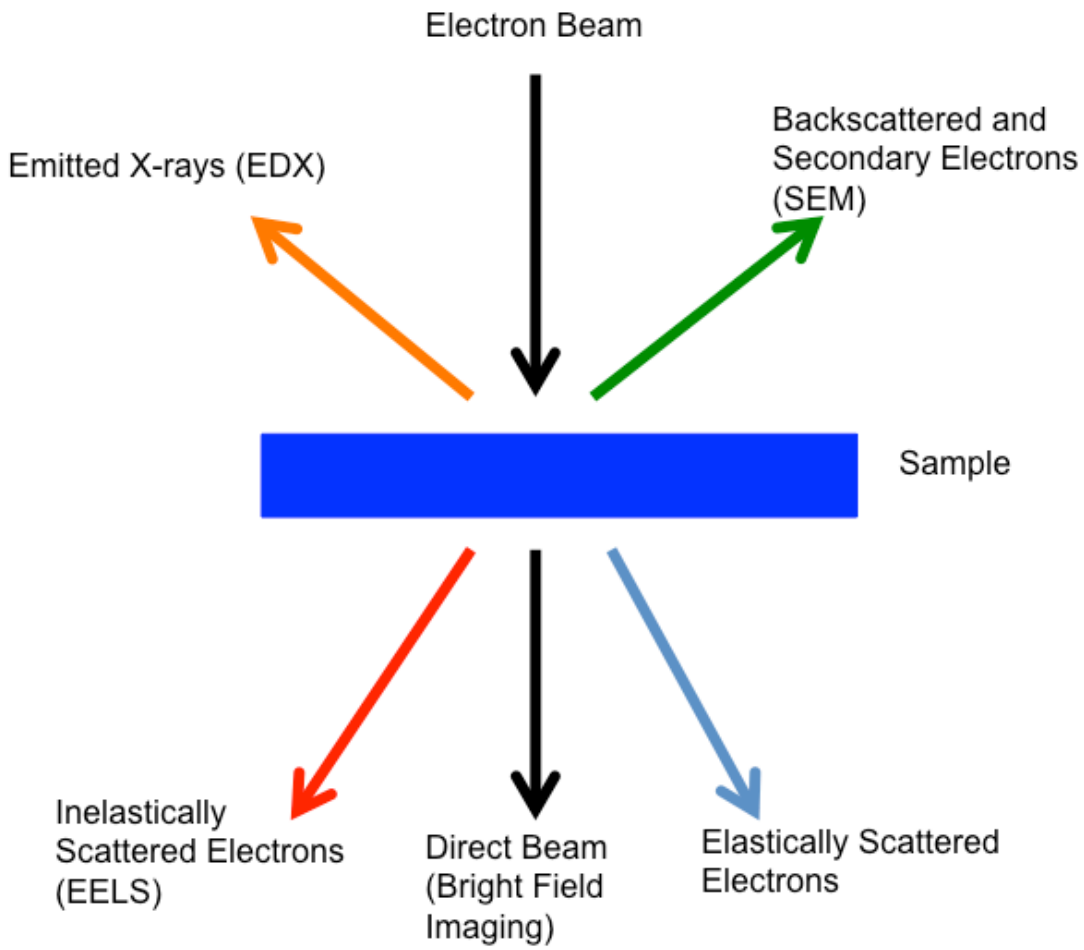

Figure 15 Interactions between electrons and a sample in electron microscopy

2.3.1.Electron Energy Loss Spectroscopy (EELS)

As the electrons are passed through the sample, the electrons are able to interact with the sample atoms in a variety of ways as shown in Figure 15. If the electrons are scattered inelastically from the sample, elemental information can be gathered about the sample using a

technique called electron energy loss spectroscopy (EELS). The sample absorbs the electrons energy and excites a core electron to the LUMO and is unique to each element. Based on the change in energy, the identity of the element can be determined.

EELS can be used to determine if a sample is core/shell or as an alloy if more than one element is present. By using an energy filter to only look at a certain energy value, elemental EELS mapping can be completed.

2.4. Scanning Electron Microscopy (SEM)

Another form of microscopy that utilizes an electron beam for imaging is scanning electron microscopy (SEM). Like with TEM, the electron beam interacts the sample, however with SEM backscattered, secondary electrons, and X-rays are analyzed. Secondary and backscattered electrons provide detail about the topography and morphology of the surface of the sample. While collecting an image, the electron beam is scanned across the surface of the sample in a raster pattern. The secondary electrons are detected at each point by a detector. Places of greater intensity are shown as bright spots on the resulting image.

SEM images were collected on a Hitachi SU-70 FE-SEM operating at 5 keV. Samples were prepared by dusting sample powder onto conductive carbon tape mounted on an Al sample holder. For oxide samples, the samples were coated with carbon to prevent charging.

2.4.1. Energy Dispersion Spectroscopy (EDS)

When a secondary electron is formed and removed from the electron shell, it leaves a positively charged hole, or electron hole, in the inner shell. To compensate the charge, an electron from the valence band will relax into the inner shell, releasing an X-ray. The process is depicted in Figure 16. The energy of the X-ray is directly related to the difference in energy of inner and valence shell and is characteristic to each element. Based on the number and energy of

the emitted X-rays, the elemental composition of the sample can be determined. This can be performed on a single point, an area, or a line.

Similarly to EELS on the TEM, EDS on the SEM can be applied to elemental mapping. In this case, as the electron beam is scanned across the surface of the sample, emitted X-rays are detected and can be compiled to create an image for each element seen in the sample.

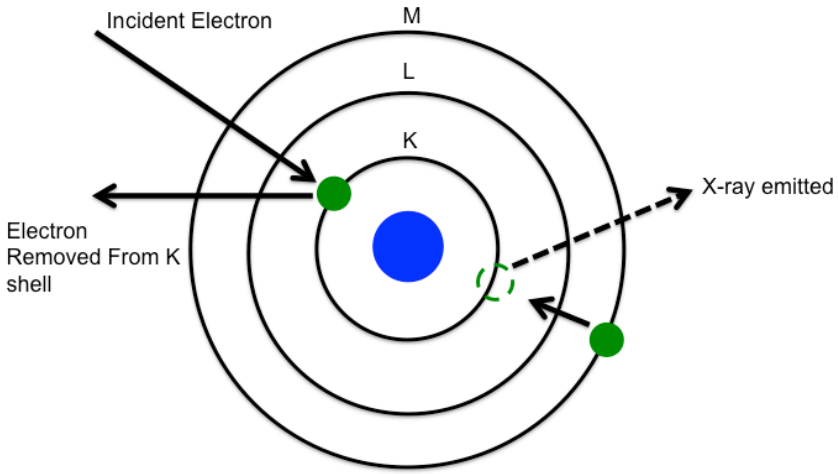

Figure 16 Schematic illustrating the creation of an X-ray from an electron source

2.5.Dynamic Light Scattering (DLS)

While TEM and SEM can give information about the size and shape of nanoparticles, these techniques are time consuming and relatively expensive. Dynamic light scattering (DLS) is an alternative that can quickly give information about the hydrodynamic radius (R_H) of nanoparticles in solution and how polydisperse the particles are in solution. DLS is also a nondestructive technique and the sample is easily recovered. During an analysis, a monochromatic He-Ne laser (633 nm) is passed through the sample as shown in the schematic in Figure 17. As the light is passed through the sample, the nanoparticles in solution will diffract

the light in either a constructive or destructive manner, creating a pattern of light and dark spots. Since the nanoparticles are in solution, they are constantly in motion with smaller particles moving faster then larger particles. Therefore, the scattering intensity changes over time. To overcome the fluctuations, an autocorrelation function is used to correlate the intensities as a function of time. The diffusion coefficient is also measured from the nanoparticles as the velocity of the Brownian motion. The viscosity, refractive index, and temperature of the solution must be known in order to relate the light scattering data to the diffusion of the nanoparticles in solution. To obtain the best results, the sample should be a very stable clean colloid.

The hydrodynamic radius, (R_H) is calculated using the Stokes-Einstein equation,

$$R_H = \frac{K_B T}{3\pi\eta D}$$

where K_B is Boltzmann's constant, T is the absolute temperature, η is the viscosity of the solution, and D is the diffusion coefficient. The equation assumes that the nanoparticles are spherical, do not interact with each other, and that they interact with the solvent system. The polydispersity index (PDI) is a measurement of the width of the particle size distribution and is determined from the DLS intensity data using the equation:

$$PDI = \frac{\mu_2}{\langle\Gamma\rangle^2}$$

where μ_2 is the variance of the decay rate distribution and Γ is the average decay rate. A value close to 0 indicates a monodisperse sample with a value of 1 being polydisperse. A value below 0.7 is considered to be mid range. Similarly to Scherrer analysis with XRD, DLS is biased towards larger sizes because larger nanoparticles will scatter more light then smaller nanoparticles. Therefore for samples containing small nanoparticles, the data should be analyzed in terms of volume instead of intensity.

A Malvern Zetasizer Nano-ZS was used to obtain the hydrodynamic radius and polydispersity index for colloidal samples. Samples were prepared by diluting with DI water as needed.

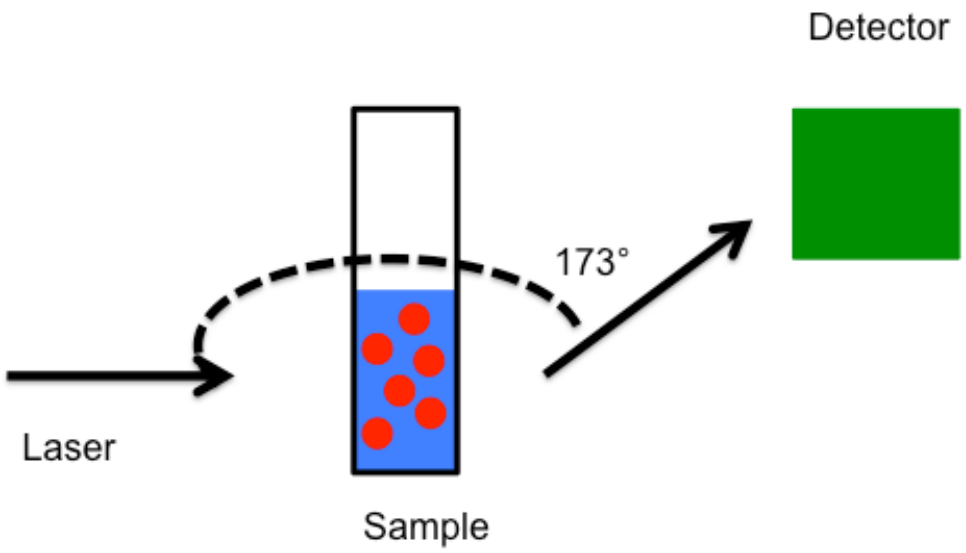

Figure 17 Schematic of DLS instrument

2.6. X-Ray photoelectron Spectroscopy (XPS)

X-Ray photoelectron spectroscopy (XPS) is a destructive analytical technique that provides detailed information about the oxidation states based on the binding energies of the sample. Due to short penetration depths of X-rays into materials of a few nanometers, XPS is considered a surface sensitive characterization technique. A typical instrument, shown in Figure 18 consists of 3 main parts, the X-Ray source, electron energy analyzer, and detector. The X-ray source is most commonly an Al source (hv=1486.6 eV) or a Mg source (hv= 1253.6 eV). The electron energy analyzer separates the emitted X-rays based on their kinetic energy. Charge

compensation from electrostatic charging causing peak broadening is completed by an internal flood gun operating at 2 eV in conjunction with an external Ar^+ flood gun.

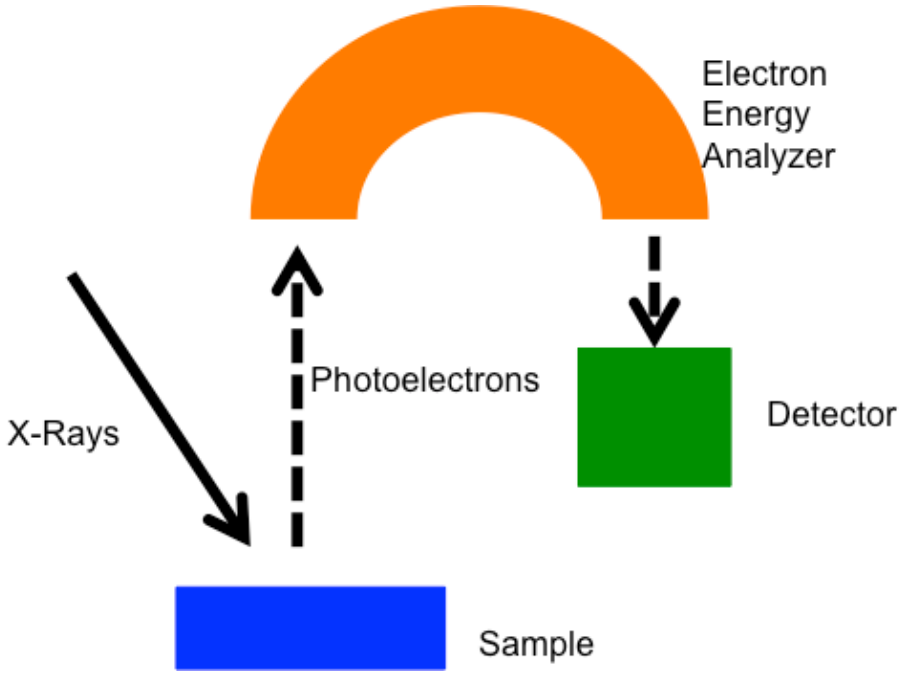

Figure 18 Schematic diagram of a typical XPS spectrometer

XPS utilizes the photoelectric effect to determine the binding energy of emitted photoelectrons. The photoelectric effect is the emission of photoelectrons from a solid, gas, or liquid when irradiated with light. During an experiment, the sample is bombarded with X-rays that interact with the sample's core electrons. The incident X-rays excite the core electrons, releasing it as a photoelectron as shown in Figure 19. The energy of this emitted X-ray can then be used to determine the binding energy of the emitted X-ray. This is completed with the equation

$$BE = KE - h\nu + \phi,$$

where BE is the binding energy, KE is the kinetic energy of the photoelectron, hν is the energy of the incident X-ray, and ϕ is the work function. The binding energy is unique for each element and energy level. The binding energy can also be used to help determine chemical binding of the element based on shifting of the measured binding energy. If the binding energy of the element is shifted to higher eV, the element in question is mostly likely in a more positive oxidation state or is bonded to a more electronegative species. Binding energies shifted to lower eV reveal the element is in a lower oxidation state or bound to a less electronegative species. Fitting XPS data can be difficult because peaks for different binding energies can overlap.

All XPS data was collected on a Thermofisher ESCAlab 250 with an Al Kα source. Samples were prepared by pressing the powder onto a small piece of indium foil and mounted onto a sample holder using double-sided conductive carbon tape. Binding energies were corrected by calibrating to the aliphatic hydrocarbon C 1s peak at 284.6 eV.

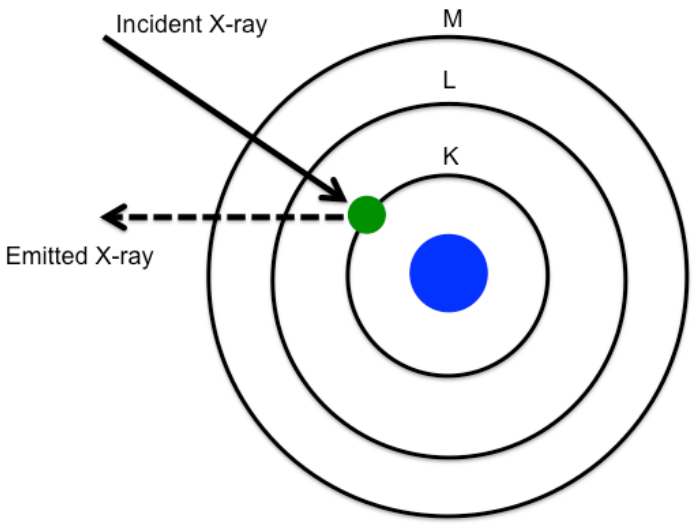

Figure 19 Schematic illustrating the creation of an X-ray from the core from an X-ray source

2.7. Vibrating Sample Magnetometry (VSM)

Vibrating sample magnetometry (VSM) is one of the most commonly used characterization instrument for magnetic materials. An instrument schematic is shown in Figure 20. The VSM contains two electromagnets that create a uniform magnetic field. As the sample is vibrated perpendicular to the magnetic field, the sample will create magnetic flux creating electric potential, which is measured by pick-up coils. This voltage is directly proportional to the magnetic moment of the sample.

In the most basic experiment performed on magnetic materials, the magnetic moment of the sample is measured as the external magnetic field is swept from a positive field, reversed to a negative field, and back to a positive field creating a hysteresis loop. From this loop, the magnetic saturation (M_s), magnetic remanence (M_r), and coercivity (H_c) can be determined.

All VSM data was collected on a VersaLab 3 Tesla Cryogen-Free Vibrating Sample Magnetometer. Samples were prepared using a VSM sample capsule loaded with between 1-10 mg of powdered sample.

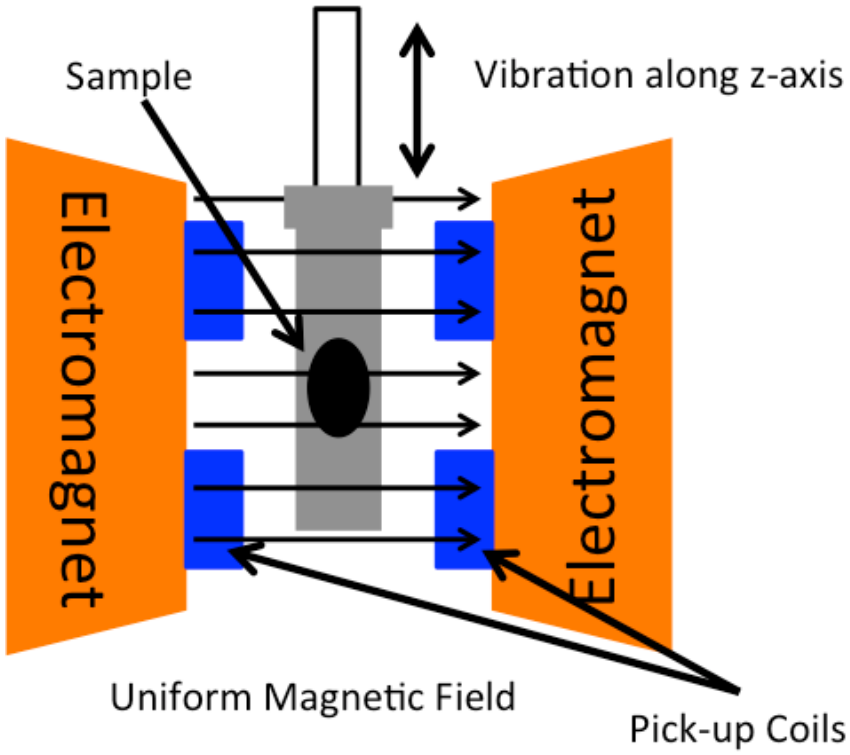

Figure 20 Schematic diagram of VSM instrument

2.8. Thermogravimetric Analysis (TGA)

Thermogravimetric analysis (TGA) is a useful technique that can be used to examine changes in a samples mass as a function of time, temperature, and environment. The instrument, shown in Figure 21, consists of a three main parts: microbalance, furnace, and gas system.

TGA data can be used in a multitude of ways, mostly investigating the samples thermal stability. With organic samples, TGA is used to determine at what temperature the sample decomposes under different environments. With nanoparticles synthesized using surfactants, it can be used to determine at what temperature the surfactant is lost. This is beneficial especially for catalysis applications since the surface of the nanoparticle needs to be exposed. For magnetic material, TGA data can be used to calculate a more accurate magnetization saturation value by determining what percentage of the sample is organic.

All TGA data was collected on a Thermo Fischer TGA Q500.

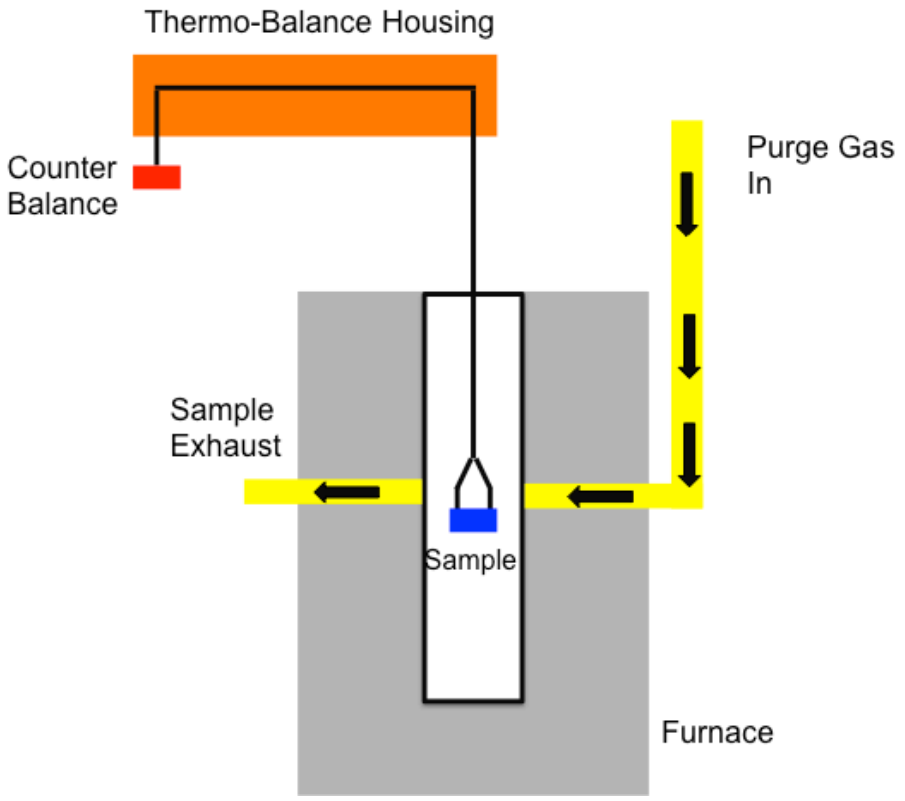

Figure 21 Schematic diagram of TGA instrument

Chapter 3: Synthesis and Characterization of CuPd Nanoparticles

3.1.Overview and Motivation

The goal of this chapter was to synthesize a CuPd alloyed nanoparticle that could be used as a catalyst for cross-coupling reactions. Previous reports have shown that a palladium homogeneous catalyst is most commonly used in cross coupling reactions, but does have limitations with recyclability, metal leaching, and catalyst recovery.[19, 84-85] While the use of a heterogeneous catalyst can reduce these problems, the use of metallic nanoparticles can also be advantageous. [86-87] The increase in surface atoms as the size decreases means that there are more active sites for catalysis to take place. Recently, nanoclusters, core/shell nanoparticles, and alloyed nanoparticles have been studied for use in a wide range of catalytic reactions.[88-92] By introducing more than one metal the electronic properties of the material can be tuned by choice of the metal or alloy.

First, a synthetic protocol was developed to achieve a homogenous alloy. Once a homogeneous alloy was synthesized, the nanoparticles were characterized by a variety of characterization techniques including XRD, ICP-OES, XPS, and TEM. The nanoparticles were then tested for catalytic activity for Heck, Sonogashira and Suzuki cross-coupling reactions.

3.2. Introduction

Cross coupling reactions, such as the Suzuki, Heck, and Sonogashira reactions have an important role in both organic and pharmaceutical synthesis and most commonly rely on palladium homogenous catalysts. One novel bimetallic nanoparticle for use in Suzuki, Heck, and Sonogashira reaction is a copper palladium alloy nanoparticle. This type of material has been successfully used as a catalyst for formic acid oxidation and methanol oxidation, and for Heck reactions.[27, 92-93] This type of bimetallic alloy nanoparticle is advantageous for catalysis because

the copper acts as an electron donor and the palladium as an electron acceptor.[94] Therefore, there is no need for electron donor ligands such as phosphine ligands, which can make catalyst recovery more difficult due to ligand interactions with the product. The overall cost of the catalyst is reduced by not only the addition of a cheaper metal, but also because catalyst recovery can be more efficient.

The addition of copper to a palladium catalyst increases the variety of cross coupling reactions the alloy is appropriate for use. Sonogashira cross-coupling reactions use a copper halide as a co-catalyst. With the addition of copper in the palladium nanoparticle, it reduces the amount of catalysts required to complete the reaction. In recent years, research has shown that Heck reactions can be catalyzed successfully in relatively high yields by both palladium and copper in a variety of solvents.[93, 95] It was shown that for Heck reactions, a bimetallic CuPd alloy had the highest catalytic efficiency for Heck reactions compared to Pd, Ag, Pd/Ag, and Pd/Ni nanoparticles synthesized by reverse micelles.[93] Recently, it was shown that a new catalyst containing copper and palladium supported on charcoal could be used for Sonogashira-Click reactions and Heck-Click reactions in high yields.[96]

3.3.Experimental Methods

3.3.1.Synthesis

In a typical experiment, 0.04 grams each of copper acetate hydrate (45.9-48.4% purity, Alfa Aesar), and palladium acetate trimer (98% purity, Aldrich), were dissolved in a 100 mL round bottom flask containing 10 mL of oleylamine (>50% purity, TCI). The solution was then heating to 350°C at a rate of 15°C/min under distillation conditions. The reaction was kept at 350°C for two hours before taken off heat and cooled to room temperature. The particles were

rinsed and sonicated in methanol and hexanes multiple times and collected by centrifugation until the supernatant was clear. The particles were dried in an oven vacuum overnight. A reaction scheme is shown in Figure 22.

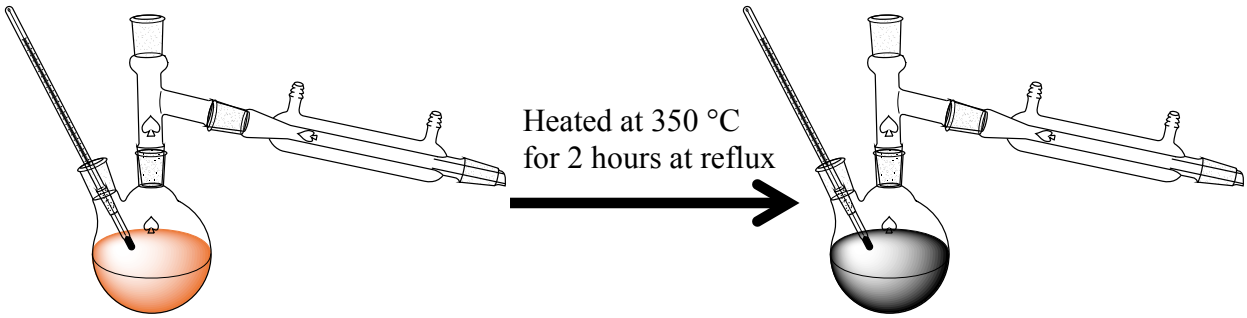

Figure 22 Reaction scheme for wet synthesis of CuPd alloyed nanoparticles

3.3.2.Characterization

The as synthesized nanoparticles were characterized using a PANalytical MPD X-Ray diffractometer (Cu Kα, λ=1.54 Å) (XRD) and the data was analyzed using X'Pert Highscore. Inductively coupled plasma optical emission spectroscopy (ICP-OES) data was collected on a Varian MPX Pro. Samples were digested in aqua reqia (1:3 ratio of HNO3 and HCl) and then diluted with DI water. Trans-mission electron microscopy (TEM) was collected on a Zeiss Libra 120 Plus operating at 120 keV. Samples were prepped with propanol and let air dry. X-Ray photoelectron spectroscopy (XPS) was performed on a Thermo fisher Scientific ESCALAB 250 using a monochromatic Al Kr X-ray. Samples were prepared on indium foil and the data was fit using CasaXPS software. The binding energies were calibrating by adjusting the aliphatic hydrocarbon C 1s peak to 284.6 eV.

3.3.3.Catalytic Testing

Dr. Ali Siamaki from the chemical engineering department at VCU under the direction of Dr. B. Frank Gupton completed all catalytic testing for this chapter.

3.3.3.1.Suzuki Cross Coupling Reaction

Iodobenzene (50 mg, 0.24 mmol) and phenylboronic acid (35.4 mg, 0.29 mmol) were mixed together in a 15 mL microwave tube using 4 mL of H_2O:EtOH (1:1) as solvents. Potassium carbonate (99 mg, 0.72 mmol) and CuPd nanoparticles (0.48 mg, 2.4 μmol) were added to the mixture and heated under microwave (250 W, 2.45 MHz) at 120°C for 10 min. The conversion % of the reaction was monitored by the GC-MS analysis (96%). The reaction mixture was further extracted with CH_2Cl_2 (3 × 50 mL) and the organic layers were combined, dried over anhydrous $MgSO_4$, and filtered. The CH_2Cl_2 solvent was then evaporated under reduced pressure and the final product was purified by means of flash chromatography using hexane:ethyl acetate as eluent to give the biphenyl product in 95% isolated yield as a white solid.

3.3.3.2.Heck Coupling Reaction

Iodobenzene (50 mg, 0.24 mmol) and styrene (50 mg, 0.48 mmol) were mixed together in a 15 mL microwave tube using 4 mL of H_2O:EtOH (1:1) as solvents. To this was added potassium carbonate (99 mg, 0.72 mmol, CuPd nanoparticles (0.48 mg, 2.4 μmol), and the mixture was heated under microwave (250 W, 2.45 MHz) at 150 °C for 10 min. The conversion % of the reaction was monitored by the GC-MS analysis (94%). The reaction mixture was further extracted with CH_2Cl_2 (3 × 50 mL) and the organic layers were combined, dried over anhydrous $MgSO_4$, and filtered. The CH_2Cl_2 solvent was then evaporated under reduced pressure and the final product was purified by means of flash chromatography using hexane:ethyl acetate as eluent to give the trans-stilbin in 90% isolated yield.

3.3.3.3.Sonogashira Coupling Reaction

Iodobenzene (50 mg, 0.24 mmol) and phenylacetylene (49 mg, 0.48 mmol) were mixed together in a 15 mL microwave tube using 4 mL of H_2O:EtOH (1:1) as solvents. To this was added potassium carbonate (99 mg, 0.72 mmol) and CuPd nanoparticles (0.48 mg, 2.4 μmol) and the mixture was heated under microwave (250 W, 2.45 MHz) at 150 °C for 10 min. The conversion % of the reaction was monitored by the GC-MS analysis (93%). The reaction mixture was further extracted with CH_2Cl_2 (3 × 50 mL) and the organic layers were combined, dried over anhydrous $MgSO_4$, and filtered. The CH_2Cl_2 solvent was then evaporated under reduced pressure and the final product was purified by means of flash chromatography using hexane:ethyl acetate as eluent to give the diphenylacetylene product in 91% isolated yield.

3.3.3.4. Recyclability Testing of CuPd in Suzuki Cross-coupling reactions

Iodobenzene (50 mg, 0.24 mmol) and phenylboronic acid (35.4 mg, 0.29 mmol) were mixed together in a 15 mL microwave tube using 4 mL of H_2O:EtOH (1:1) as solvents. Potassium carbonate (99 mg, 0.72 mmol) and CuPd nanoparticles (0.48 mg, 2.4 μmol) were added to the mixture and was heated under microwave (250 W, 2.45 MHz) at 120°C for 10 minutes. The conversion % of the reaction was monitored by the GC-MS analysis (96%). The reaction mixture was diluted with EtOH (4 mL), the mixture was centrifuged for 5 minutes, and the solution above the catalyst was carefully decanted. The EtOH washing and centrifugation were repeated two more times to insure complete removal of the organic product from the surface of the catalyst. Upon completing this procedure, fresh reagents including iodobenzene, phenylboronic acid and potassium carbonate in a mixture of 4 mL H_2O:EtOH were added to the catalyst and the reaction mixture was heated under microwave at 120 °C for 10 minutes for the

next run. The conversion rate was determined by GC/MS based on the consumption of the starting material.

3.4.Results and Discussion

TEM images were used to determine the size and morphology of the as synthesized CuPd nanoparticles. As seen in Figure 23, the nanoparticles appeared to be large agglomerates of smaller nanoparticles. Based on the micrographs, the nanoparticles appear to be relatively uniform in size and shape and are 4.5 ±0.6 nm. The small size makes these nanoparticles attractive for catalysis do to their larger surface to volume ratio with more active sites.[97]

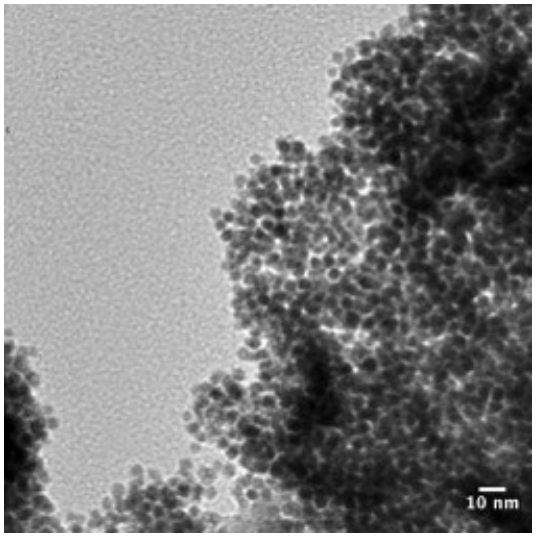

Figure 23 TEM images of the CuPd nanoparticles

The XRD pattern for the as prepared CuPd nanoparticles is displayed in Figure 24 and shows an FCC crystal structure centered between the peaks for FCC phases of copper and palladium metal, suggesting the formation of an alloy between the two metals. The lattice parameter for the alloyed peak as determined by Reitveld refinement can be compared to the standard lattice parameters for pure FCC copper and palladium to determine the composition of

the alloy using Vegard's law.[98] Using FCC copper and palladium lattice parameters of 3.614 Å and 3.867 Å respectively, the alloyed peak was found to be 47% copper and 53% palladium.[99] ICP-OES was used to confirm this ratio and was found to be 36% copper and 64% palladium. The difference in the ratio could be due from heterogeneity or the presence of amorphous palladium that were not seen in the XRD spectrum but seen in the ICP-OES data since ICP-OES looks at noncrystalline material as well as crystalline material.[95] Using information from the peak shape, Scherrer analysis was conducted on the most intense CuPd peak and determined that the crystallite size of the nanoparticles was 4.5 nm.[99] This agrees well with the small nanoparticle size determined by TEM of 4.5 ±0.6 nm.

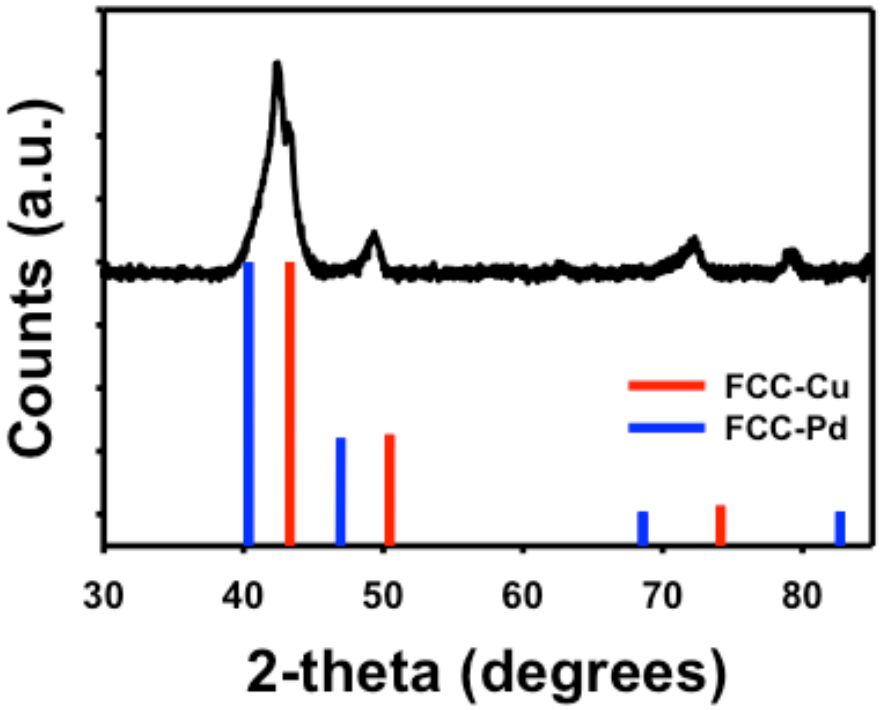

Figure 24 XRD pattern of as prepared CuPd nanoparticles

XPS was used to determine the oxidation state and composition of copper and palladium of the CuPd nanoparticles by observing the binding energies of copper and palladium. Figure 25a shows the binding energies for palladium in the 3d region and displays two distinct peaks at 334.8 eV and one at 340.2 eV that corresponds to Pd $3d^{5/2}$ and Pd $3d^{3/2}$, respectively. The peak at 334.8 eV, corresponding to Pd^0, contained a shoulder peak with a binding energy of 335.2 eV that shows Pd^{2+} is also on the surface. Using the areas of the peaks, Pd^0 and Pd^{2+} were found to exist in a 62 to 38 ratio on the surface, respectively. Similarly, the copper XPS spectrum for the 2p region, shown in Figure 25b, contained two peaks with binding energies of 334.8 eV and 951.16 eV that correspond to Cu $2p^{3/2}$ and $2p^{1/2}$, respectively. Both peaks contained shoulders that revealed two oxidation states of copper are present on the surface of the CuPd nanoparticle. The broad peak at 931.39 eV corresponds to the binding energy of Cu^0 with a shoulder at 932.0 eV, showing that Cu^+ is also present in a ratio of 62 to 38 for Cu^0 and Cu^+. In conjunction with the ratio between Pd^0 and Pd^{2+}, the ratio suggests that overall 38% of the surface of the CuPd nanoparticles has been oxidized to Cu_2O and PdO.

The presence of the both Pd^0 and Cu^+ on the surface makes these CuPd nanoparticles attractive for use in Sonogashira reactions, which have been shown to utilize both a Pd^0 species and a Cu^+.[13] In the alloy nanoparticles, both species are present on the surface eliminating the need for a co-catalysts copper salt. The presence of both metals and oxides on the surface could also allow for electron transfer from the Pd to the Cu changing the oxidation state of the Pd from Pd^{2+} to Pd^0 needed to catalyze the reaction. This could affect the catalytic activity for Suzuki, Sonogashira, and Heck cross coupling reactions.

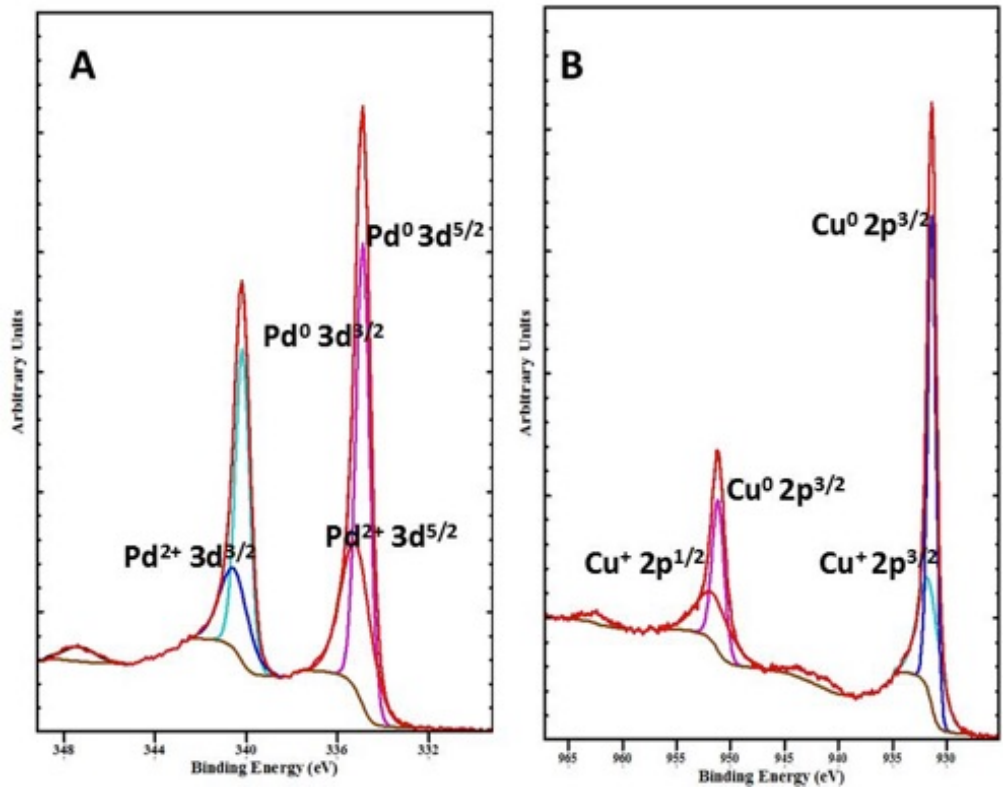

Figure 25 Binding energies of A. Pd 3d and B. Cu 2p

3.4.1.Reactivity of CuPd nanoparticles in Suzuki cross-coupling reactions

The catalytic activity of CuPd nanoparticles were examined for multiply cross-coupling reactions. The results for Suzuki cross-coupling reactions are shown in Table 5. With iodobenzene and phenylboronic acid with 1 mol% CuPd catalyst, the biphenyl product was isolated with a 95% yield as shown in Table 5, entry 1a (Isolated Yield: 95% ^{1}H NMR (300 MHz, $CDCl_3$): 7.76-7.73 (m, 2H), 7.61-7.55 (m, 2H), 7.52-7.47 (m, 1H). ^{13}C NMR (75.5 MHz, $CDCl_3$): 141.7, 129.2, 127.6, 127.6. GC-MS (EI, 70 eV): m/z(%) = 154 (100) [M^+]). Notably, the reaction was effectively proceeded at lower catalyst loading of 0.01 mol %. At this low concentration of 0.01 mol %, the CuPd nanoparticles were capable of converting 60% of iodobenzene to biphenyl product using the microwave irradiation at 120 °C for 5 minutes.

Further heating this reaction under microwave at 120 °C provided a 92% conversion to the product after 10 minutes.

Table 5 Suzuki cross-coupling reactions using CuPd nanoparticles

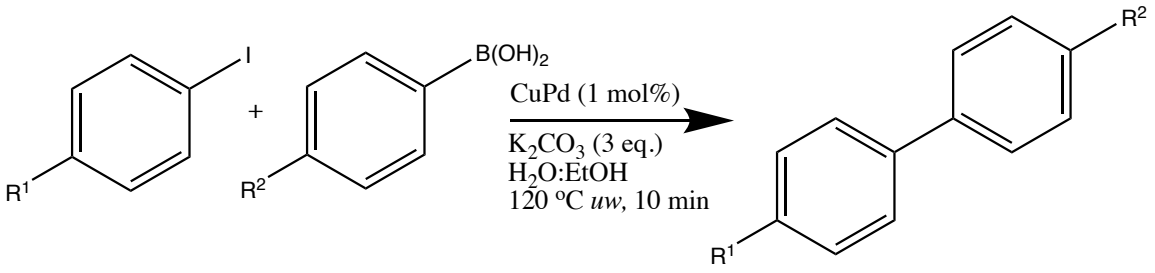

Cpd	Aryl-Halide	Boronic acid	1[b] (%)	%
a	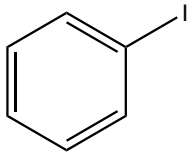	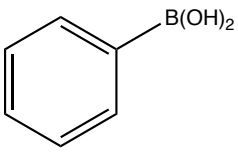	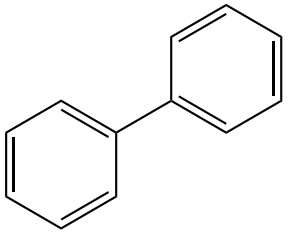	95
b	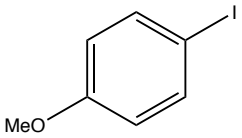	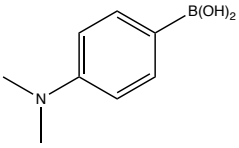	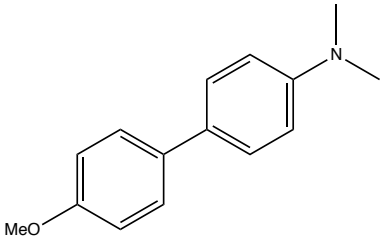	90
c	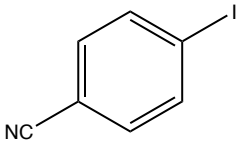	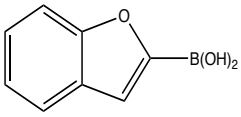	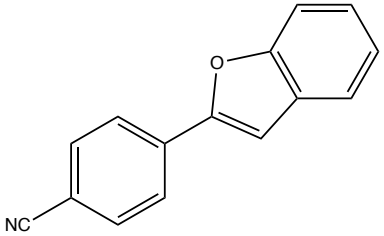	88

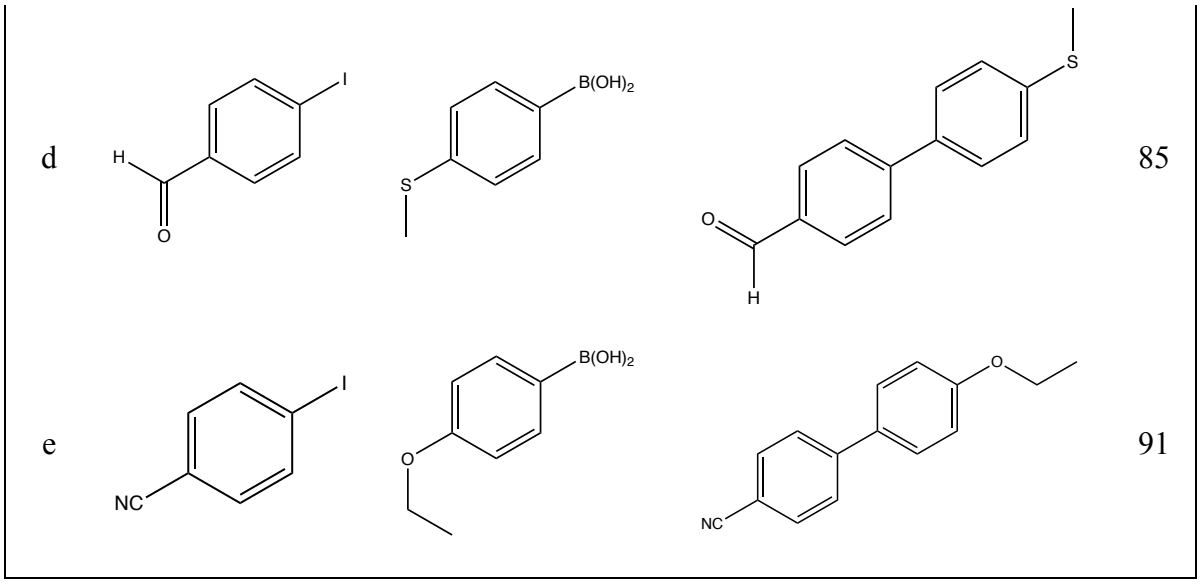

These results proved an excellent catalytic activity of CuPd nanoparticles were a turnover number of 6000 and turnover frequency of 72000 h^{-1} for Suzuki cross-coupling reactions under microwave irradiation. Furthermore, the CuPd nanoparticles were successfully recycled for multiple times using the Suzuki reaction conditions in Table 5, affording 95%, 90%, and 78% conversions after three consecutive runs, respectively by GC/MS. This is shown in Table 6. After each run, the catalyst was easily removed from the reaction mixture by centrifugation, washed with EtOH followed by decanting the solution, and reused in the subsequent run. Interestingly, the utility of the CuPd bimetallic nanoparticles were further investigated in Suzuki cross-coupling reactions with other functionalized substrates. As shown in Table 5, both electron donor and electron withdrawing functional groups such as methoxy, ethoxy, cyano, aldehyde, thiomethyl, and dimethylamino can be effectively employed on both the aryl halide and phenylboronic acid to afford the corresponding biphenyl products in excellent isolated yields as shown in Table 5 1b-1e ((4'-Methoxy-biphenyl-4-yl)-dimethyl-amine (b): Isolated yield: 90% ^{1}H NMR (300 MHz, $CDCl_3$): 7.52-7.47 (t, 4H), 6.99-6.96 (d, 2H), 6.83-6.80 (d, 2H), 3.85 (s, 3H),

3.00 (s, 6H). ^{13}C (75.5 MHz, $CDCl_3$): 158.5, 149.7, 134.2, 129.4, 127.56, 127.56, 114.3, 113.1, 55.5, 40.8., 4-Benzofuran-6-yl-benzonitrile (c): Isolated yield: 88% ^{1}H NMR (300 MHz, DMSO-d_6): 8.08-8.04 (s, br, 1H), 7.98-7.76 (S, 4H), 7.77-7.60 (dd, 1H), 7.55 (S, 1H), 7.64-7.24 (m, 2H). ^{13}C(75.5 MHz, DMSO-d6): 167.8, 155.1, 155.04, 134.6, 132.7, 129.3, 129.07, 128.9, 127.1, 125.6,125.04, 124.07, 122.1, 111.8, 104.2., 4'-Methylsulfanyl-biphenyl-4-carbaldehyde (d): Isolated yield: 85% ^{1}H NMR (300 MHz, $CDCl_3$): 10.02 (s, 1H), 7.9-7.88 (d, 2H), 7.72-7.70 (d, 2H), 7.55-7.52 (d, 2H), 7.33-7.30 (d, 2H), 2.51 (s, 3H). ^{13}C (75.5 MHz, $CDCl_3$): 192.01, 146.6, 139.7, 136.2, 135.3, 130.5, 127.8, 127.4, 126.8, 15.7., 4'-ethoxy-[1,1'-biphenyl]-4-carbonitrile (1e): Isolated yield: 91% ^{1}H NMR (300 MHz, $CDCl_3$): 7.68-7.60 (q, 4H), 7.53-7.50 (d, 2H), 7.0-6.96 (d, 2H), 4.08-4.05 (d, 2H), 1.46-1.41 (t, 3H). ^{13}C(75.5 MHz, $CDCl_3$): 159.7, 145.2, 132.7, 131.4, 128.5, 127.2, 119.2, 115.2, 110.2, 63.7, 15.03).

Table 6 Recycling Experiment with CuPd nanoparticles

Run	Conversion (%)
1	95
2	90
3	78
4	60

3.4.2.Reactivity of CuPd nanoparticles in Heck and Sonogashira coupling reactions

The reactivity of the CuPd nanoparticles were further investigated for the Heck coupling reactions using iodobenzene with styrene forming trans-stibin in 90% isolated yield (^{1}H NMR

(300 MHz, $CDCl_3$): 7.57-7.54 (m, 5H), 7.42-7.38 (t, 5H), 7.32-7.27 (m, 2H). ^{13}C NMR (75.5 MHz, $CDCl_3$): 137.6, 128.9, 127.9, 126.8. GC-MS (EI, 70 eV): m/z(%) = 180 (100) [M^+]).

To test the activity in Sonogashira coupling reaction, iodobenzene was reacted with phenyl acetylene to form diphenylacetylene with a 91% isolated yield (^1H NMR (300 MHz, $CDCl_3$): 7.54-7.50 (m, 4H), 7.32-7.29 (m, 6H), ^{13}C NMR (75.5 MHz, $CDCl_3$): 131.7, 128.5, 128.2, 123.3, 89.5 GC-MS (EI, 70eV): m/z(%) = 178 (100) [M^+]). As depicted in Figure 26, these reactions were successfully preformed under microwave heating at 150 °C for 10 minutes, providing the corresponding Heck and Sonogashira coupling products.

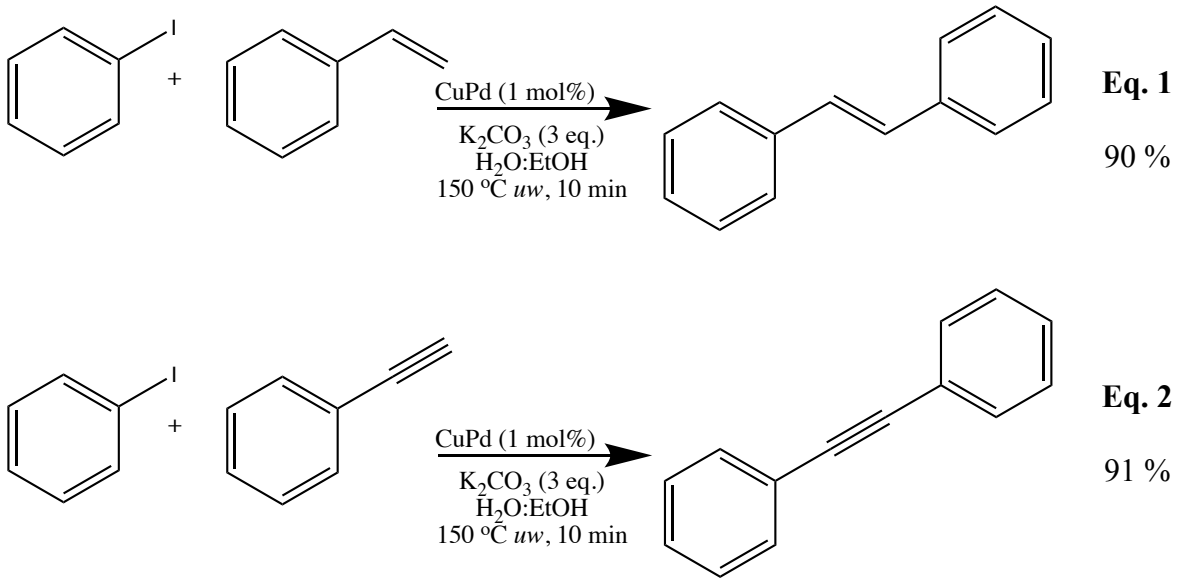

Figure 26 Schematic of Heck (Eq. 1) and Sonogashira (Eq. 2) coupling reactions with CuPd nanoparticles

It is noteworthy that typical Sonogashira reactions using homogeneous Pd catalysts usually require a copper halide salt (*e.g.* CuI) as the co-catalyst to stabilize the negative charge on the acetylide anion, forming the copper acetylide intermediate, and thus facilitating the transmetallation step to Pd complex during the coupling process. By incorporating the copper into the palladium nanoparticle, the copper can be oxidized to Cu^+, activating the substances for

catalysis and eliminating the need for the copper halide. Thus, the CuPd nanoparticles allow for simultaneous activation of aryl halide and the alkyne on the surface of the bimetallic catalyst in which the Cu site of the nanoparticles can serve as the alkyne activator during the catalytic cycle, circumventing the necessity of using any other copper salts in this reaction. Notably, performing these reactions at a lower temperature of 120 °C for 10 min resulted in a lower conversion of 65 and 60% for Heck and Sonogashira coupling reactions, respectively. Extending the reaction time did not affect the conversion at 120 °C.

3.5. Conclusions

In this chapter, CuPd nanoparticles were successfully synthesized using a simple oleylamine solvothermal method. Characterization showed the particles were bimetallic and consisted of palladium and copper metal and their respected oxides. The CuPd nanoparticles were examined for catalytic activity in Suzuki cross-coupling reactions. These nanoparticles were highly reactive toward the Suzuki cross-coupling reactions with iodobenzene under microwave heating conditions using H_2O: EtOH as environmentally benign solvent systems, affording a high turnover frequency of 72000 h^{-1} as well as multiple recyclability for Suzuki coupling reaction. This bimetallic catalyst demonstrated excellent utility with other functionalized substrates as well with yields over 85%. Furthermore, the CuPd nanoparticles prepared by an oleylamine synthesis also showed potential as a catalyst for Heck and Sonogashira coupling reactions. By incorporating copper with the palladium nanoparticles, this bimetallic nanoparticle can activate and stabilize the alkyne during the Sonogashira catalytic cycle, affording the high yield of the product using the microwave irradiation as the clean heating source. This eliminates the need for a copper halide co-catalyst.

Chapter 4: Continuous flow synthesis of Cu@M (M=Ni, Co) core/shell nanocomposites

4.1. Overview and Motivation

This chapter focuses on adapting a benchtop synthesis of Cu@Ni paper previous published by our laboratory to a continuous flow synthesis method.[100] In Kyler Carroll's paper, he relied on a temperature difference based on if the reaction was run under reflux or distillation. By heating at different temperatures, the reduction and nucleation of Cu and Ni can be efficiently separated leading to core-shell morphology.

Lab scale approaches for the synthesis of core-shell nanomaterials commonly utilizes a two-step process, high boiling point solvents (e.g. oleylamine [101] or polyethylene glycols [100]). These high boiling point solvents are also highly viscous; solvent viscosity is a major concern when using a flow process making it difficult to pump at low rates and allow for sufficient heating times. Also, a two-step approach requires double the equipment and double the cost. To overcome solvent viscosity issues and increase reaction rate, ethanol is added as a cosolvent. We show that complex core-shell structures, like Cu@Ni and Cu@Co particles can be synthesized in a single step continuous flow process with slight modifications to pre-existing lab scale synthetic approaches. This work helps to demonstrate that continuous flow processes are a viable approach to the industrial scale synthesis of complex nanostructured materials that can be used as a Fischer-Tropsch catalyst.

4.2.Introduction

While metallic nanomaterials commonly show enhanced properties (ie magnetic, optical, or catalytic) when compared to their bulk counterparts, their implementation into commercial and industrial applications is still limited.[102] The solution-based synthesis of metallic

nanoparticles requires high temperatures, long reaction times, strong reducing agents, and commonly are run at low reactant concentrations. These high temperatures, long reactions times, and use of hazardous chemicals make translating lab scale nanoparticle syntheses to industrial scale volumes difficult. Increasing reaction volumes causes slower heating and cooling rates and introduces large temperature gradients as you move away from the heat source.[4] One proposed method to overcome these obstacles is the use of a flow microreactor for the large scale, continuous production of metallic nanoparticles.

A continuous flow microreactor process uses microcapillary columns and minimizes temperature gradients in the reaction solution by immersing the microcapillary into a continuous heating source. The continuous flow allows for small volumes of the reaction solution to be heated at allowing for instantaneous heating and cooling rates. The versatility and effectiveness of the continuous flow production of metallic nanoparticles has already been demonstrated on several instances throughout literature mostly with simples systems such as metals, alloys, or oxides.[103-107] Morphology control in continuous flow production has been achieved with metallic nanoparticles in various systems by altering pH, temperature, flow rates, and use of surfactants.[108-110] More complex structures, such as those with a core-shell morphology, to date have been made in lab scale batch processes.

Bimetallic nanoparticles, especially bimetallic core/shell nanoparticles, recently have shown unique catalytic activity compared to monometallic catalysts due to synergistic effects.[27, 111-113] By adding copper to Fischer-Tropsch catalysts, the copper is able to help facilitate the non-dissociative activation of CO during the reaction.[114] Recently, it has been shown that a Cu@CuCo core/shell nanoparticle was able to successfully synthesize higher alcohols due to the synergistic effects between copper, which was able to adsorb the CO, and cobalt, which acted as

the active site for Fischer Tropsch.[111] It has also been shown that a Co@Cu/SiO_2 catalyst has better thermal stability compared to its monometallic counterparts with higher selectivity for C-C bonds and methanol.[115]

4.3. Experimental Methods

4.3.1. Continuous Synthesis Capillary Microreactor

The capillary microreactor used to synthesize cobalt particles consists of three basic parts: a pump, a heated coil, and a back pressure regulator as shown in the schematic in Figure 27. An Agilent 1100 series HPLC pump was used to pump the preheated reactants through a 1/8th inch outer diameter stainless steel capillary coil that is submerged in a Huber CC 308 circulating heating oil bath. At the end of the coil, a Swagelok gas/water pressure regulator was connected to control the pressure inside the heated coil. The synthesized particles were collected with a catch flask located after the regulator. The larger diameter of the stainless steel capillary coil, moderate flow rate, and high temperature of the reaction helps with the prevention of clogging the capillary.[116] The capillary was also cleaned with 5% nitric acid before use to remove any residual fouling material on the surface of the coil.

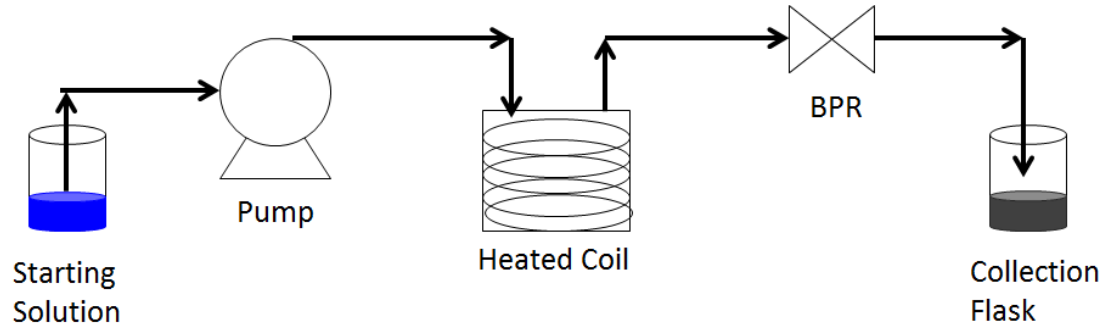

Figure 27 Schematic of capillary microreactor set-up

4.3.2. Synthesis of Cu@M nanocomposites

0.5 grams of $CuCl_2$ $2H_2O$ (Alfa Aesar, 99%), 0.5 grams of $NiCl_2$ $6H_2O$ (Fisher Scientific tech grade), and 3 grams of NaOH (Sigma Aldrich) were dissolved into a solvent mixture containing 45 mL of ethanol (Pharmco-AAPER, 190 proof) and 5 mL of ethylene glycol (BDH). This solution was stirred until all of the NaOH was in solution. The reactants were pumped through the capillary microreactor, cleaned with 5% nitric acid solution, at a rate of 2 mL/min at 200°C at a pressure of 100 bar. The particles were separated using a rare earth magnet and washed several times with methanol. The particles were dried in a vacuum oven overnight. The same procedure was used to synthesize Cu@Co particles except 0.5 grams of $CoCl_2$ $6H_2O$ (Alfa Aesar, 98%) was used instead of $NiCl_2$ $6H_2O$. All reagents were used as received without additional purification.

4.3.3. Characterization

The particles were analyzed using an X-Ray Diffractometer (Cu K_α, λ=1.54 Å) (XRD) and the data was analyzed using X'Pert Highscore. The lattice parameter of each metal was calculated using Reitveld Refinement. The magnetic data was obtained on a Quantum Design VersaLab Vibrating Sample Magnetometer (VSM). Transmission electron microscopy (TEM) was collected on a Zeiss Libra 120 Plus operating at 120 keV. Expected Energy Loss Spectroscopy (EELS) was conducted at the L-Edge of Co, Ni, and Cu, and were analyzed using Gatan Digital Micrograph analysis software.

4.3.4.Fischer Tropsch Testing

The fixed bed reaction, shown in Figure 28, was carried out in a stainless steel tubular reactor (5.3 mm ID) and the catalyst bed consists of 10 mg held by quartz wool. The pressure

was regulated by a back pressure regulator to have a typical FT pressure. The gas product after passing the cold trap at 15ºC is automatically injected to Gas Chromatograph that is equipped with two Agilent HP-PLOT Q columns to be analyzed using FID and TCD detectors. The catalysts were pretreated in-situ with (H_2:He) gas mixture 20:40 sccm at 300ºC to reduce samples. Catalytic activity and selectivity was studied by running a reaction at industrial conditions of FT synthesis (20 bar, and 220-320ºC) with a H_2/CO ratio of 2. Above 320ºC the methanation rate became high and the formation of higher carbon number products dropped significantly. The total flow of gases (CO + H_2) was 30 sccm and diluted with 10 sccm of He.

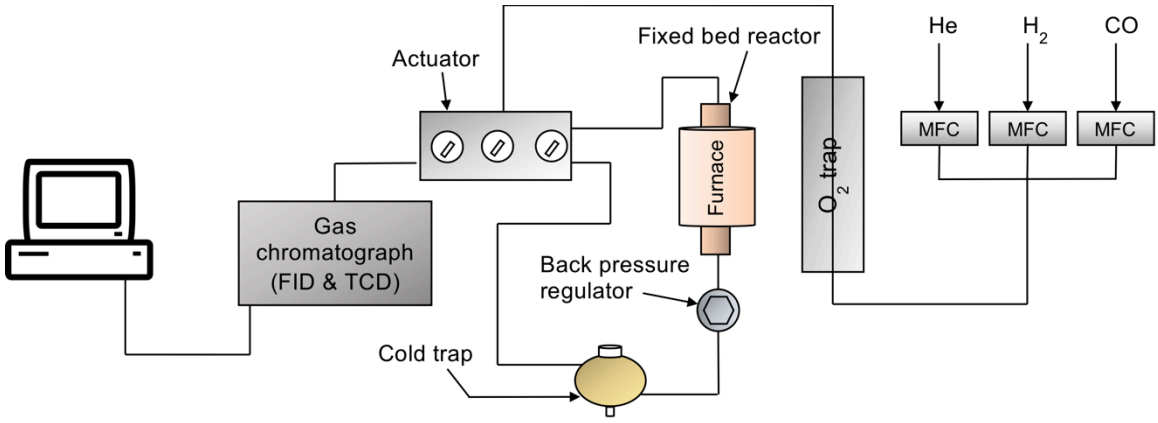

Figure 28 Schematic of Fischer Tropsch reactor

4.4. Results and Discussion

On the benchtop, Cu@Ni particles can be synthesized using a modified polyol process with ethylene glycol as a solvent and reducing agent.[100] By heating at different temperatures, the reduction and nucleation of Cu and Ni can be efficiently separated leading to core-shell morphology. Ethylene glycol and ethanol are used as solvent and reducing agent.[117] Using this approach, bimetallic core-shell particles were synthesized in a single step process without the use of multiple temperature steps. The separation of nucleation events can be explained by the large

difference in reduction potentials between Cu^{2+} and Ni^{2+} or Co^{2+} ions going to their metallic states.

4.4.1. Characterization of Cu@M nanocomposites

X-ray diffraction patterns for as prepared powders are shown in Figure 29. The Cu@Ni XRD spectrum showed peaks for two distinct FCC phases possessing lattice parameters of 3.607 Å and 3.530 Å calculated using Reitveld Refinement, respectively. These values differ from standard lattice parameters for FCC copper and nickel of 3.614 Å and 3.524 Å, suggesting slight alloying between the two metals.[118] Using Vegard's law, the interface between the layers was determined to be 7.9% nickel copper rich phase containing and a nickel rich with 6.6% copper. Similar results were seen with in the XRD spectrum of the synthesized Cu@Co particles. Two resolved FCC phases with lattice parameters of 3.613 Å and 3.554 Å were observed. A degree of alloying was again confirmed 1.8% cobalt was found in the copper rich phase and the cobalt rich phase contained 15.2% copper. Although there was a slight degree of alloy formation in each system, two resolved FCC phases were identified and imply that sufficient separation of nucleation events between the Cu and Ni or Co was achieved. The lattice parameters were comparable to those measured by Carroll *et al*. and are shown in Table 7.[100] Based on the values for the lattice parameter, this work shows a lesser degree of alloying compared to the work published by Carroll *et al.* [100]

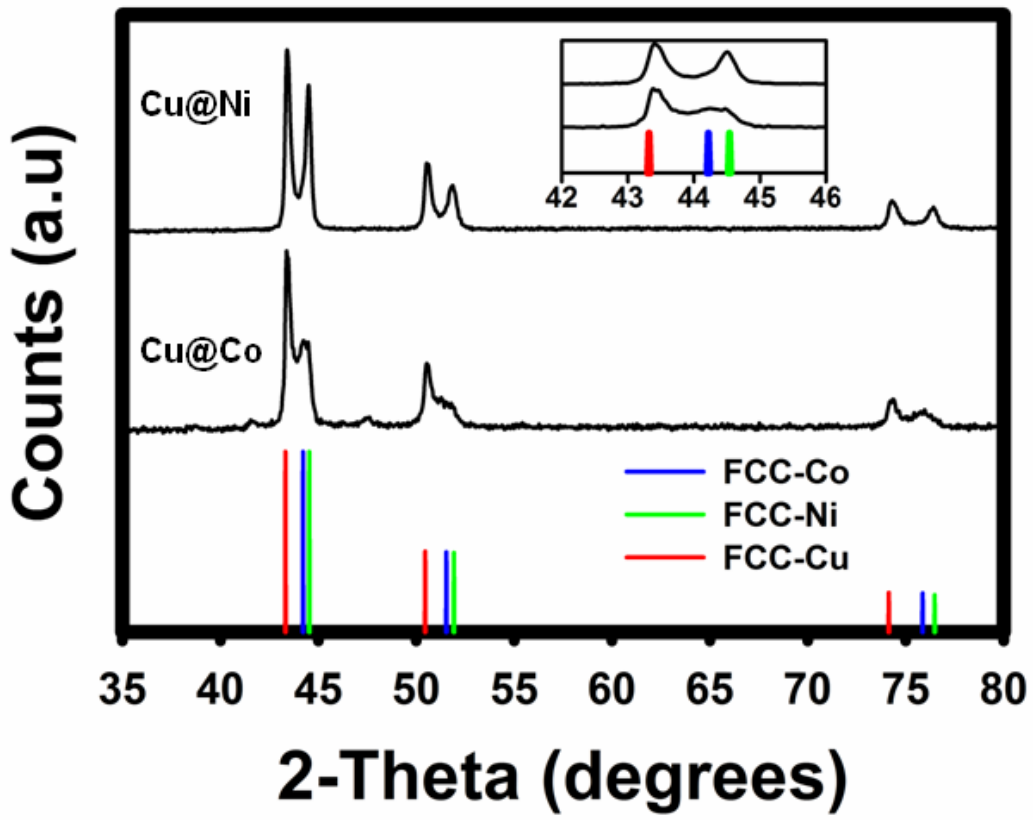

Figure 29 XRD patterns of synthesized Cu@Ni, Cu@Co, and elemental Co, Ni, and Cu.

Table 7 Comparison of lattice parameters in Cu@Ni nanocomposites

Element	Lattice Parameters in This Work (Å)	Lattice Parameters in Literature[100] (Å)	Lattice Parameters for pure element[118] (Å)
Cu	3.607	3.609	3.614
Ni	3.530	3.519	3.524

Transmission electron microscopy (TEM) imaging was used to investigate the particle morphology and identify the presence of core-shell particles. Synthesized Cu@Ni particles possessed diameters between 300 nm to 500 nm. The particles were irregular with many facets

and sharp edges at the particles surface could be observed in Figure 30 (a,b). The observed particle diameters and shape agrees well with the previous report of polyol synthesized Cu@Ni particles.[100] The Cu@Co particles showed a wide range of particle shapes and sizes; Particle shapes ranged from spheres to long cylindrical rod structures (Figure 30 (d)). To confirm the core shell morphology, electron energy loss spectroscopy (EELS) mapping was employed. Figure 30(c) and (f) show the distinct core shell structure of the Cu@Ni and Cu@Co particles, respectively. The Cu@Ni particles displayed a 75-100 nm Ni rich shell. The Cu@Co particles possessed similar Co shell thicknesses to the Cu@Ni particles. The observed shell thicknesses were increased compared to calculated crystallite sizes from XRD analysis. This implies the presence of a polycrystalline shell; however possible chemical gradients at the core-shell interface could cause the visualization of larger than actual shell thicknesses. The large size distribution and variety of particle morphologies can be attributed to the poor efficiency of ethanol as a capping agent.[117] To better control the size and shape of the particles, a more efficient capping agent could be used. In batch reactions, oleylamine and oleic acid have proved to effectively control the morphology of cobalt and cobalt nickel alloyed nanoparticles using a polyol method as well as varying the concentration of base in the reaction.[119-120] The TEM analysis clearly reveals the formation of ferromagnetic core shell particles in a continuous flow single step process.

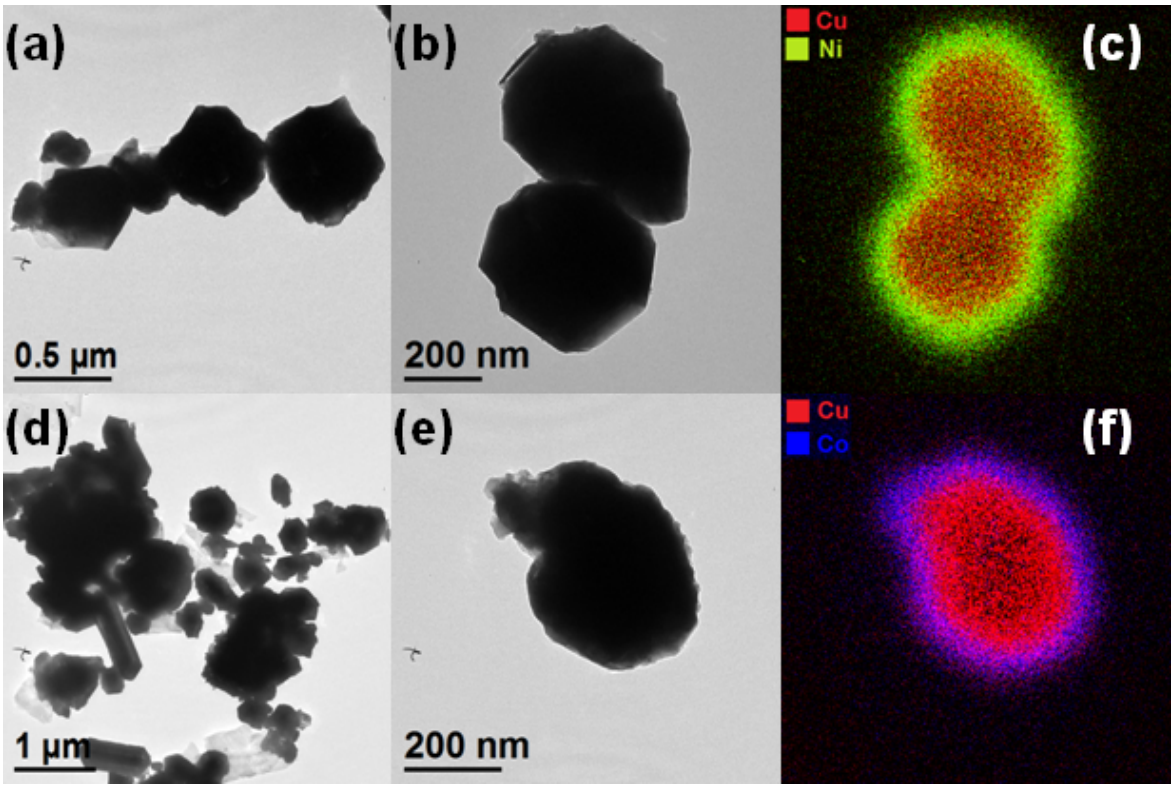

Figure 30 Bright Field TEM images of (a,b) Cu@Ni and (d,e) Cu@Co particles. EELS maps of (c) Cu@Ni and (f) Cu@ Co particles.

Room temperature hysteresis curves of the as prepared ferromagnetic particles were collected and are shown in Figure 31A. The magnetization saturation value for the Cu@Ni particles was 28 emu/g with a coercivity of 100 Oe. This value is higher than that reported by Carroll *et al.* with a magnetization saturation value of 18.15 emu/g.[100] The higher value in this work can be attributed to larger percentage of nickel present in the sample. The Cu@Co particles presented a magnetization saturation value of 56.9 emu/g with a coercivity of 125 Oe. Combining the elemental composition data gathered by ICP-OES with the magnetization saturation values for the Cu@Ni and Cu@Co particles, the magnetization saturation value for just the nickel and cobalt can be calculated, assuming that only the nickel and cobalt contribute to the magnetization. The ICP-OES data showed the Cu@Ni particle composition was $Cu_{46}Ni_{54}$.

Correcting the magnetization saturation value for just the nickel, the value increases to 51.9 emu/g, which is closer to the bulk nickel magnetic moment of 54.4 emu/g. The Cu@Co particle composition was $Cu_{51}Co_{49}$ according the ICP-OES. When corrected for just cobalt, the magnetization saturation value increased to 116 emu/g. However, this value is much lower than the bulk cobalt magnetic moment of 160 emu/g. The discrepancies could be caused by a small amount of metal oxide and is under investigation. M(T) curves were also obtained of the Cu@Ni and Cu@Co particles at 50 Oe and are shown in Figure 31B. The shape of the ZFC curves reveal that the particles have a large size distribution[121], which agrees well with the observed particles in the collected TEM images in Figure 30.

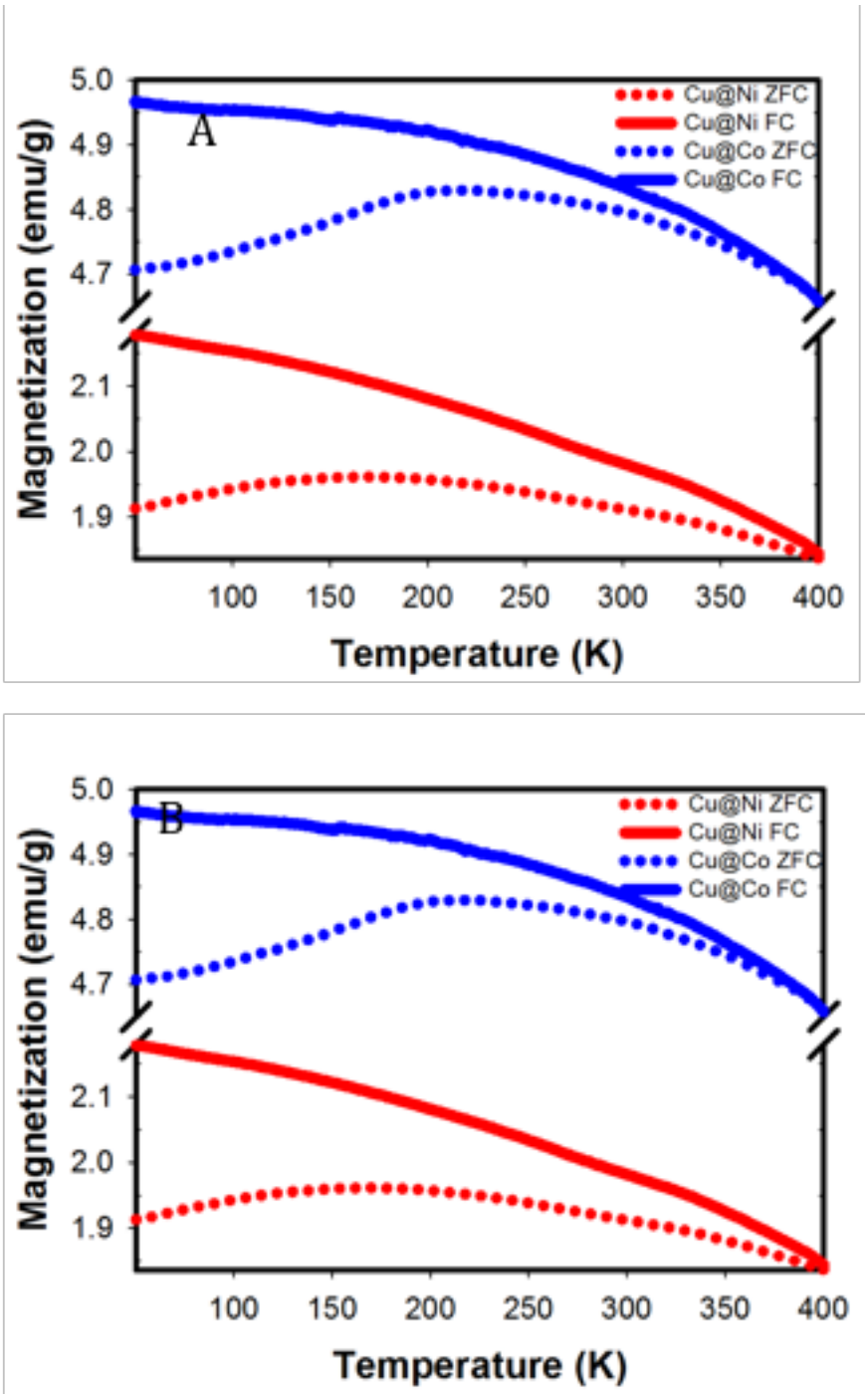

Figure 31 A. Room temperature hysteresis of Cu@Ni and Cu@Co particles B. M(T) curves of Cu@Ni and Cu@Co particles taken at 50 Oe

4.4.2. Temperature Stability on Core/Shell structure

Since each core shell system experienced a slight degree of alloy formation, the effect of temperature on alloy formation was investigated using Elevated Temperature XRD (ETXRD) on

samples prepared at 200 °C (Figure 32). The individual FCC structures show minimal alloy formation below 550 °C. A slight shift in peak positions to lower 2 theta angles was observed for each metal and is due thermal expansion of the metal structures. The ETXRD data shows that alloy formation is limited at temperatures below 550 °C, and that the alloy formation for samples prepared at 200 °C cannot be attributed to thermal effects, and is most likely due to an incomplete separation of nucleation events. Above 550 °C, peak broadening was observed. This is attributed to a decrease in crystallite size due to the diffusion-induced disorder of the metals during the alloying process.

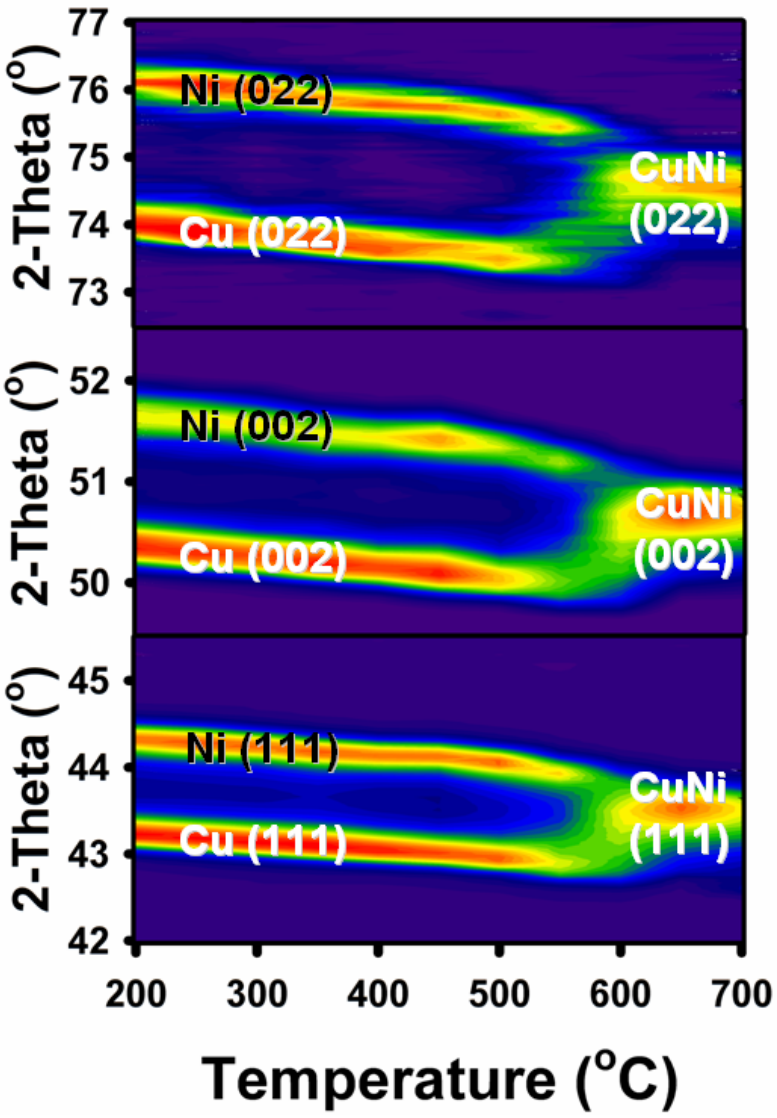

Figure 32 High Temperature XRD patterns for Cu@Ni particles collected from 200 °C to 700 °C

Although thermally induced chemical alloying does not occur till temperatures in excess of 550 °C, increasing reaction temperatures above 200 °C resulted in an increase of alloy formation between the core and shell components. For instance, conducting flow syntheses at 295 °C resulted in a cobalt rich shell containing 38.2% copper for the Cu@Co system. Also at higher temperatures a significant amount of sodium carboxylate impurities were observed in collected XRD spectrums, shown in Figure 33. These sodium carboxylate impurities were

identified to be in the form of sodium carbonate and sodium oxalate.[12] The carbonate and oxalate anions are common oxidation products of ethylene glycol, and their presence at high reaction temperatures can be attributed to an increased rate of oxidation of the ethylene glycol.[122] The higher rates of oxidation would also lead to a faster reduction process for the Cu, Ni, and Co; this would cause less differentiation between nucleation events and helps to explain the increase in alloy formation at high reaction temperatures.

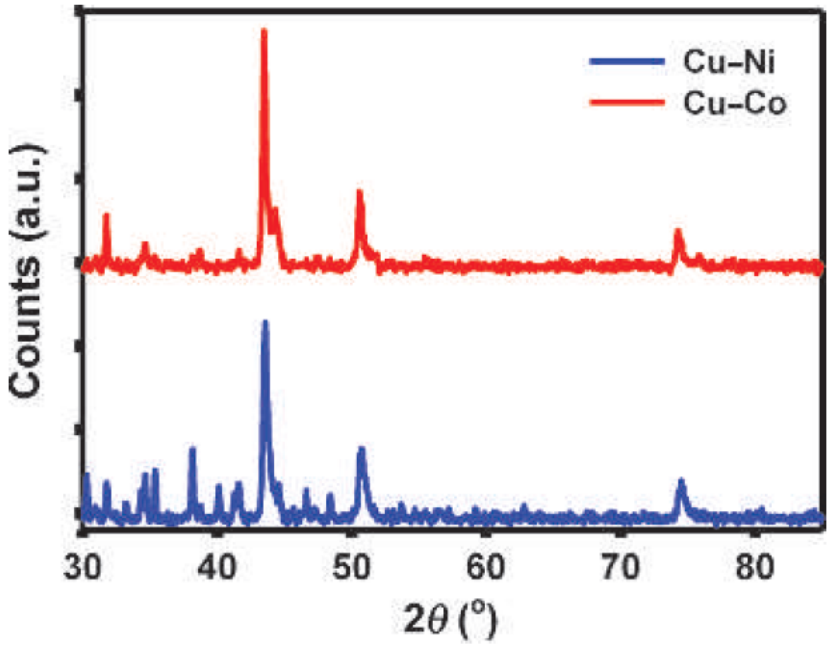

Figure 33 XRD spectra of synthesize Cu@M particles at 295 °C

4.5. Catalytic Activity for Fischer Tropsch

Both nanocomposites were tested for reactivity for Fischer Tropsch and results are shown in Figure 34. For both samples, the activity was insignificant below 220 ºC, which is a typical Fischer Tropsch reaction temperature, but each catalyst did eventually exhibit some activity. For Cu@Ni catalyst, activity starts around 260ºC and exhibits an approximately exponential increase

with temperature as expected. The Cu@Co material becomes active at 230 ºC, but the rate increases only slowly and linearly thereafter; this suggests a restructuring and possible loss of active sites as the temperature increased. Under these conditions, it is likely that the cobalt shell is restructuring to the poor Fischer Tropsch catalyst carbide and the nickel shell remains relatively unchanged.[123-124] Based on the temperature study, the Cu@M nanocomposite core/shell morphology was stable up to 550 °C. However, the catalytic activity of the Cu@Co nanocomposites decreased at a much lower temperature. XRD spectra of both nanocomposites were collected after catalytic testing and are shown in Figure 35. The spectra show restructuring of the crystal structure from Cu@Co to cobalt carbide did take place, possibly reducing the number of cobalt active sites.

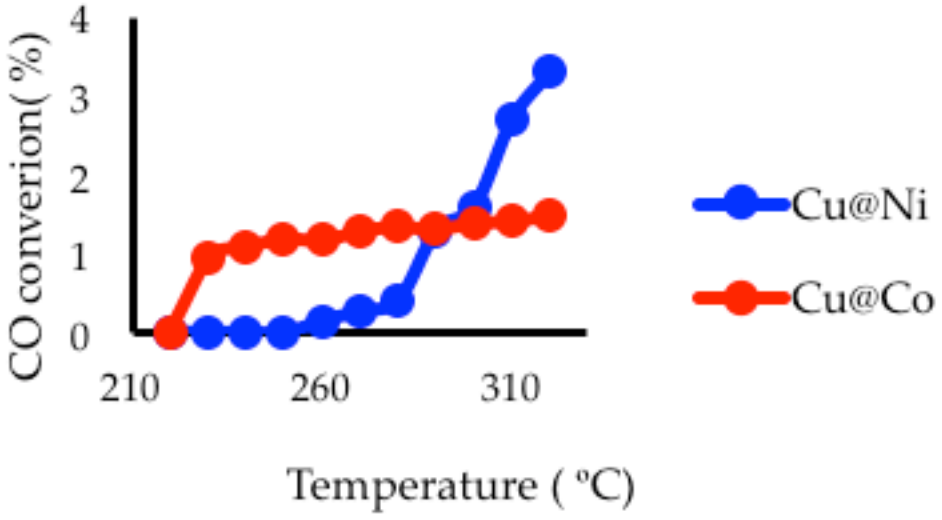

Figure 34 Conversion of carbon monoxide versus reaction temperature.

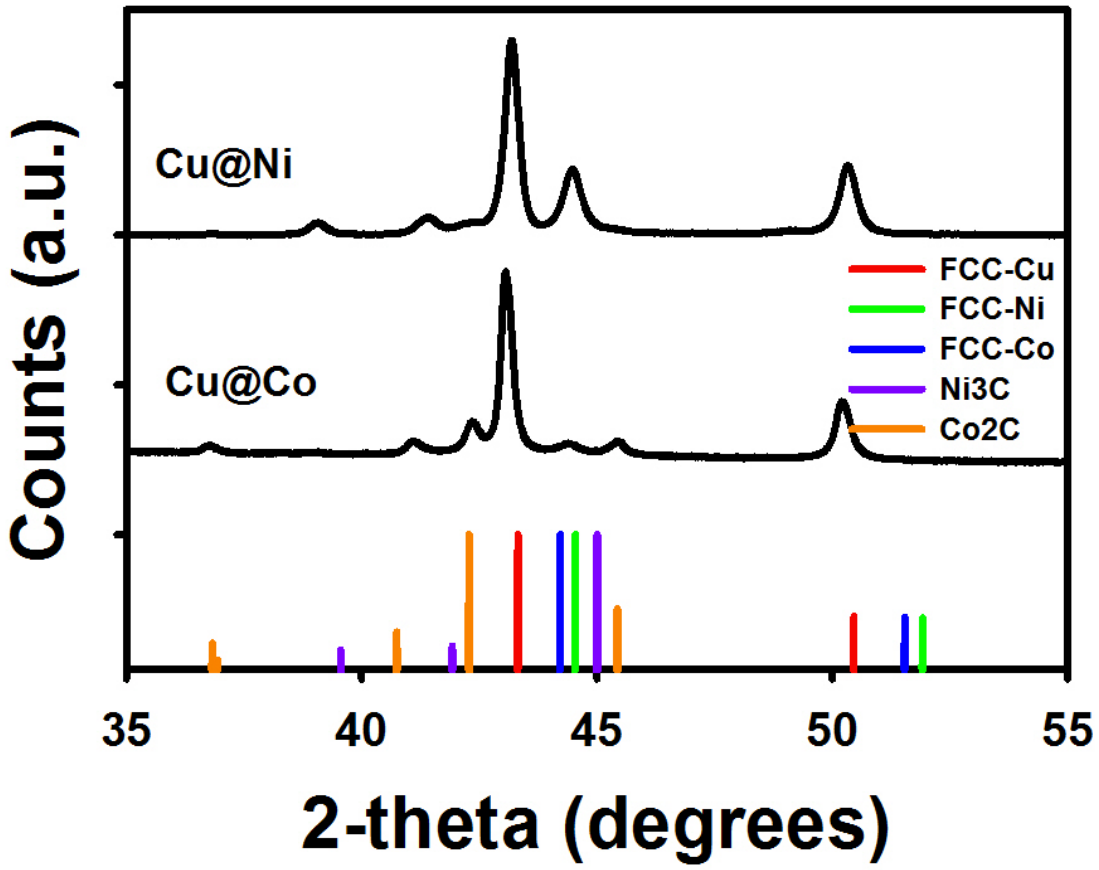

Figure 35 XRD of Cu@Co and Cu@Ni nanocomposites after Fischer Tropsch catalytic testing

The hydrocarbons distribution at 320ºC (maximum activity) is given in Figure 36. Comparing Cu@Ni and Cu@Co, the light hydrocarbon production rate is higher for Cu@Ni catalyst, especially in the C1-C4 range. That is in consistent with literature work of Ni catalyst for Fischer Tropsch reaction which has high production rate of light hydrocarbons and high methanation activity.[125] On the other hand, Co catalyst is known to be more selective for heavier hydrocarbon range (high molecular mass paraffins).[126]

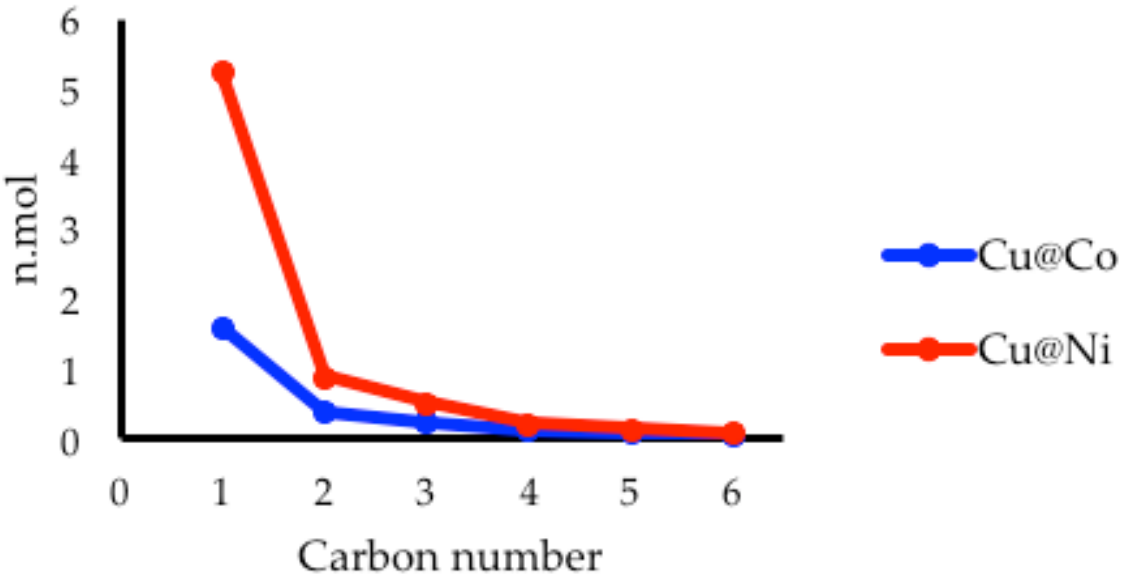

Figure 36 Hydrocarbon distribution as a function of carbon number.

The other important factor in Fischer Tropsch synthesis is olefin to paraffin ratio. In Figure 37, olefin to paraffin ratios were compared for the two catalysts. Cu@Co has high olefin to paraffin ratio up to 4.2 at carbon number 3 and it is higher for all carbon numbers (C2-C6), compared to the Cu@Ni olefin to paraffin ratios. This implies the hydrogenation rate or degree of hydrogenation of the CH_2 monomer building block is higher when Cu@Ni catalyst is used for the reaction. Thus, the selectivity of high molecular mass hydrocarbons is higher with Cu@Co catalyst.

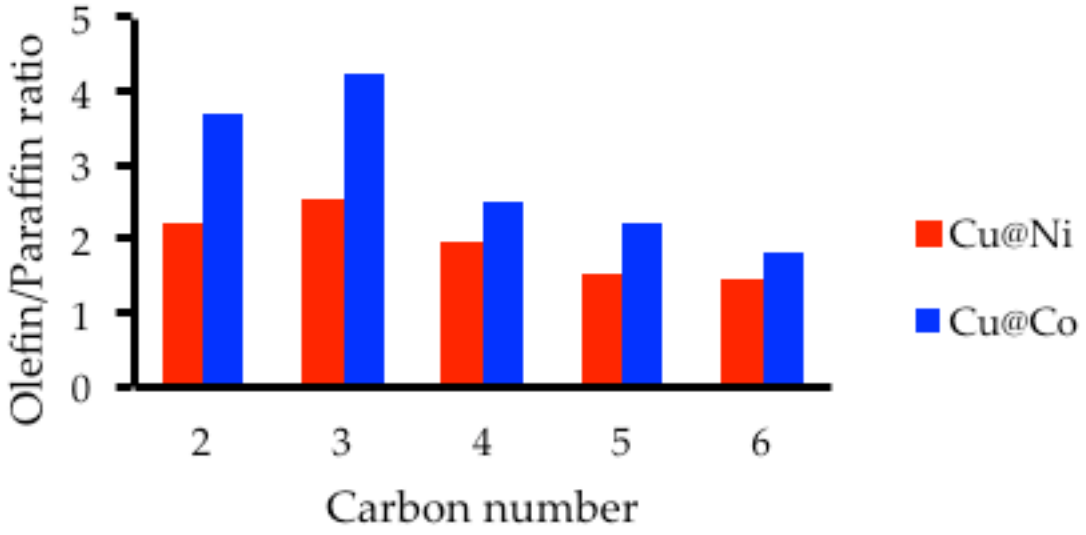

Figure 37 Olefin/Paraffin ration for C2-C6.

4.6.Conclusions

In this chapter, Cu@M nanocrystalline nanocomposites, where M is either nickel or cobalt, were synthesized using a capillary microreactor. At 200 °C, both Cu@Ni and Cu@Co particles were synthesized with very little alloying between the two metals. TEM analysis confirmed that the particles had core shell morphology. When the reaction temperature was increased to 295 °C, a higher percentage of alloying was seen between both the Cu@Ni and Cu@Co particles, but still contained FCC phases of the individual metals. Elevated temperature XRD showed that below 550 °C, there is very minimal alloying between copper and nickel. It was not until above 550 °C that the metals started to alloy. Both samples showed catalytic activity towards Fischer Tropsch. The Cu@Ni nanocomposite showed activity starting at 260 °C with a higher production rate for lower molecular weights. The Cu@Co nanocomposites showed activity starting at 230 °C with a higher production rate for higher molecular weights, but

showed a possible reconstructing of the cobalt shell. The capillary microreactor used in this study has the capabilities to make a wide range of materials in shorter reaction times compared to conventional benchtop methods.

Chapter 5: Continuous Microwave Flow Synthesis of Platinum Nanoparticles

5.1. Overview and Motivation

In Chapter 4, Cu@M nanoparticles were synthesized using a capillary flow reactor using a stainless steel coil that was submerged and heated using a circulating oil heating bath. While this reaction was successful, the oil bath had to be preheated before the reaction could take place and relied on convection methods to heat. Microwave heating has also been shown to be an efficient heat source for both organic and inorganic synthesis reactions. This chapter focuses on the synthesis of platinum nanoparticles using microwave irradiation as the heat source. The reaction was completed with water as the solvent and ascorbic acid as the reducing agent. To optimize the reaction conditions, the reaction was first run using conventional heating methods, then a conventional microwave, and lastly using a continuous flow microwave reactor. The optimized nanoparticles were tested for catalytic activity for the hydrogenation of octene.

5.2. Introduction

Noble metal nanoparticles have interesting optical and catalytic properties that are dependent on their size and shapes. However, large-scale production of the nanoparticles is difficult. Conventional benchtop synthesis methods have limitations when producing noble metal nanoparticles on an industrial scale including low product yields. By using a continuous flow reactor, the product yield can be drastically increased with a shorter reaction time.[80] Using a benchtop method with sodium citrate and tannic acid as co-reducing sources, gold nanoparticles with controllable sizes of 3.5-10 nm were synthesized.[127] Sodium citrate is not commonly used as a reducing agent for platinum, therefore ascorbic acid was used instead with tannic acid.

Using a microreactor with conventional heating, gold nanoparticle of 5-50 nm were using ascorbic acid as the reducing agent.[6] When the metal was switched to platinum 10 nm platinum nanoparticles were synthesized, but did not afford a stable colloid.[128] Over the course of 6 days, the platinum nanoparticles aggregated to from clusters of 40-50 nm.

By combining continuous flow methods with microwave heating, synthesized nanoparticles will have controlled sizes and shapes due to the rapid heating, short reaction times, faster reaction rates, and increased product yield.[129] By combining flow reactors with microwave heating, the heat transfer is increased and selectively heats the polar molecules, ions, and metals in solution which increases the reaction rate.[71] Microwave continuous flow reactors have successfully synthesized metal and metal oxide nanoparticls.[81, 129-132] By combining microwave flow synthesis with a modified Turkevich method, small mondisperse colloidal platinum nanoparticles should be obtained.

5.3.Experimental Methods

5.3.1. Synthesis of platinum nanoparticles on benchtop

In a typical experiment, 0.49 mmol of K_2PtCl_4, 0.66 mmol ascorbic acid, 0.001 mmol tannic acid, 0.30 mmol K_2CO_3, were dissolved in 50 mL of DI water while stirring. The pH was adjusted as needed with 0.1 M NaOH. The reaction was heated on a hotplate at various temperatures.

5.3.2.Synthesis of platinum nanoparticles using a conventional microwave

In a typical experiment, 0.49 mmol of K_2PtCl_4, 0.66 mmol ascorbic acid, 0.001 mmol tannic acid, 0.30 mmol K_2CO_3, were dissolved in 50 mL of DI water while stirring. The pH was

adjusted as needed with 0.1 M NaOH. The reaction was heated using a conventional microwave operating at 1100 W.

5.3.3.Synthesis of platinum nanoparticles with continuous flow microwave capillary reactor

The microwave flow reactor consists of two basic parts and is a schematic is shown in Figure 38. A Knauer 1050 smartline pump is used to push the starting solution through a 1/16th inch inner diameter PTFE tubing that was coiled inside a 125 mL roundbottom flask. The flask is filled with DI water to help with uniform heating of the coil. The flask was placed in the microwave cavity of a CEM discovery microwave SP. The synthesized nanoparticles were collected with a catch flask.

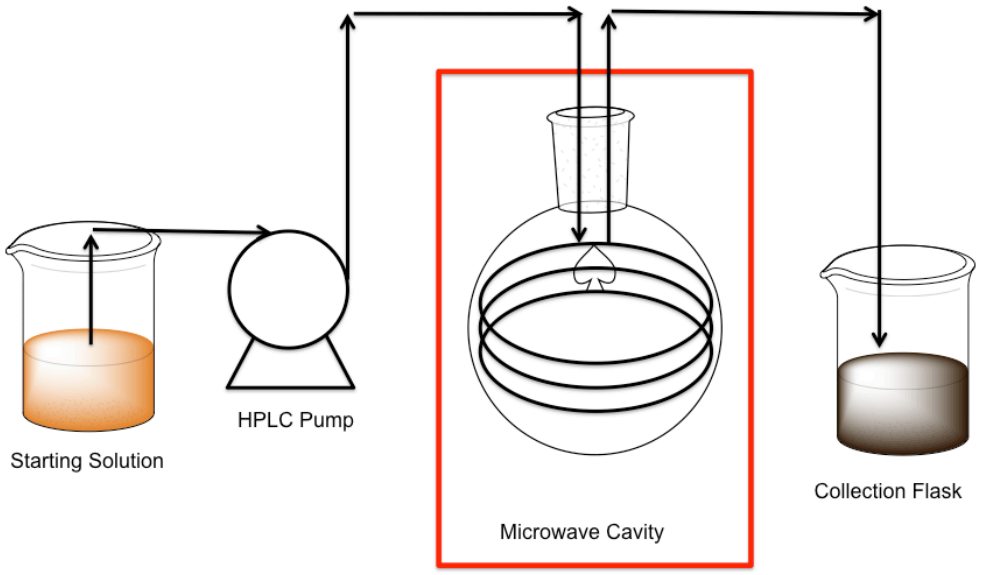

Figure 38. Schematic of Continuous Flow Microwave Microreactor

5.3.4. Synthesis of platinum nanoparticles using a continuous stir tank microwave reactor

For these reactions, a commercially available continuous stir tank reactor (CSTR) from CEM was used. The CSTR has a total volume of 10 mL and a schematic of the reactor setup is shown in Figure 39. Two syringe pumps set at 0.5 mL/min were used that met at a y mixing point to the stir tank. A peristaltic pump set at 400 rpm was used to pull the solution out of the stir tank to have a resonance time of 10 minutes in the stir tank.

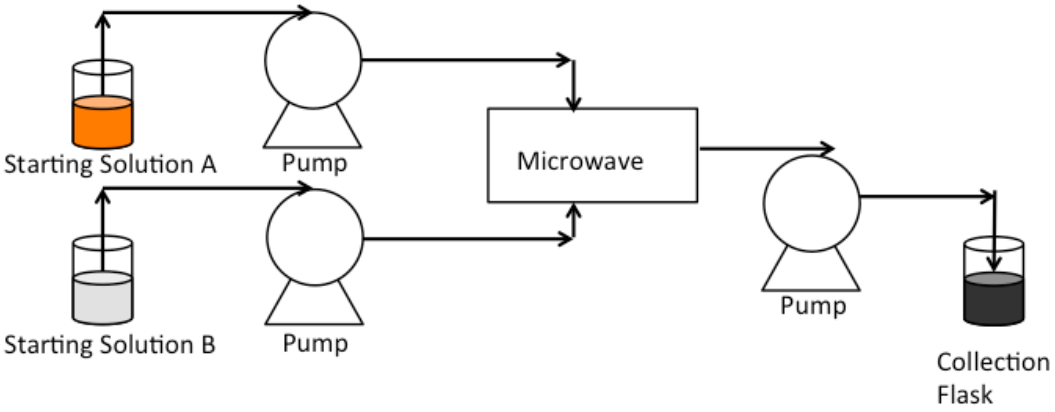

Figure 39 Schematic of CSTR microwave reactor

5.3.5.Characterization

The hydrodynamic size of the nanoparticles was determined by dynamic light scattering (DLS) using a Malvern Zetasizer. Transmission electron microscopy (TEM) was collected on a Zeiss Libra 120 Plus operating at 120 keV. The nanoparticles were characterized using a PANalytical MPD X-Ray diffractometer (Cu Kα, λ=1.54 Å) (XRD) and the data was analyzed using X'Pert Highscore.

5.3.6.Hydrogenation Reactions

Hydrogenation of octene was preformed on a HEL Chemscan II in stainless steel autoclaves loaded with 0.01 mmol of catalyst in 3 mL of DI H_2O. After three pressure/vent cycles with hydrogen, the reactor was pressurized to 400 psi of H_2 and heated to 200 °C while stirring at 500 rpm for 30 minutes. After cooling, 3 mmol of octene was added to the pretreated catalyst solution. The solution was heated to 30 °C under 114 psi of H_2 and let react for various times. The reaction was monitored by GC/MS. To prepare for GC, 30 µL of solution was diluted with 2 mL of dichloromethane and pushed through a silica column to remove the platinum catalyst from solution.

5.4. Results and Discussion

5.4.1.Optimization of benchtop synthesis

5.4.1.1.Temperature

Reaction temperature is one of the more influential parameters on the synthesis of nanoparticles. With this set of reactions, the temperature was varied between 50-95 °C with a reaction time of 10 minutes at temperature. At all temperatures, platinum was reduced and crystal structure was confirmed by XRD and shown in Figure 40. The platinum nanoparticles synthesized at all four temperatures displayed similar crystallite sizes and are shown in Table 8. Temperature had the biggest effect on the hydrodynamic radius of the platinum nanoparticles as seen with DLS analysis. With a reaction temperature of 50 °C, the nanoparticles were larger with a hydrodynamic radius of 1083 d.nm with a PDI value of 0.552. At the lower temperature, the nucleation and growth stage of the nanoparticles are not separated, leading to large, more

polydisperse nanoparticles.[31] Based on the results in Table 8, a reaction temperature of 70 °C afforded platinum nanoparticles with the smallest hydrodynamic radius, PDI, and crystallite size.

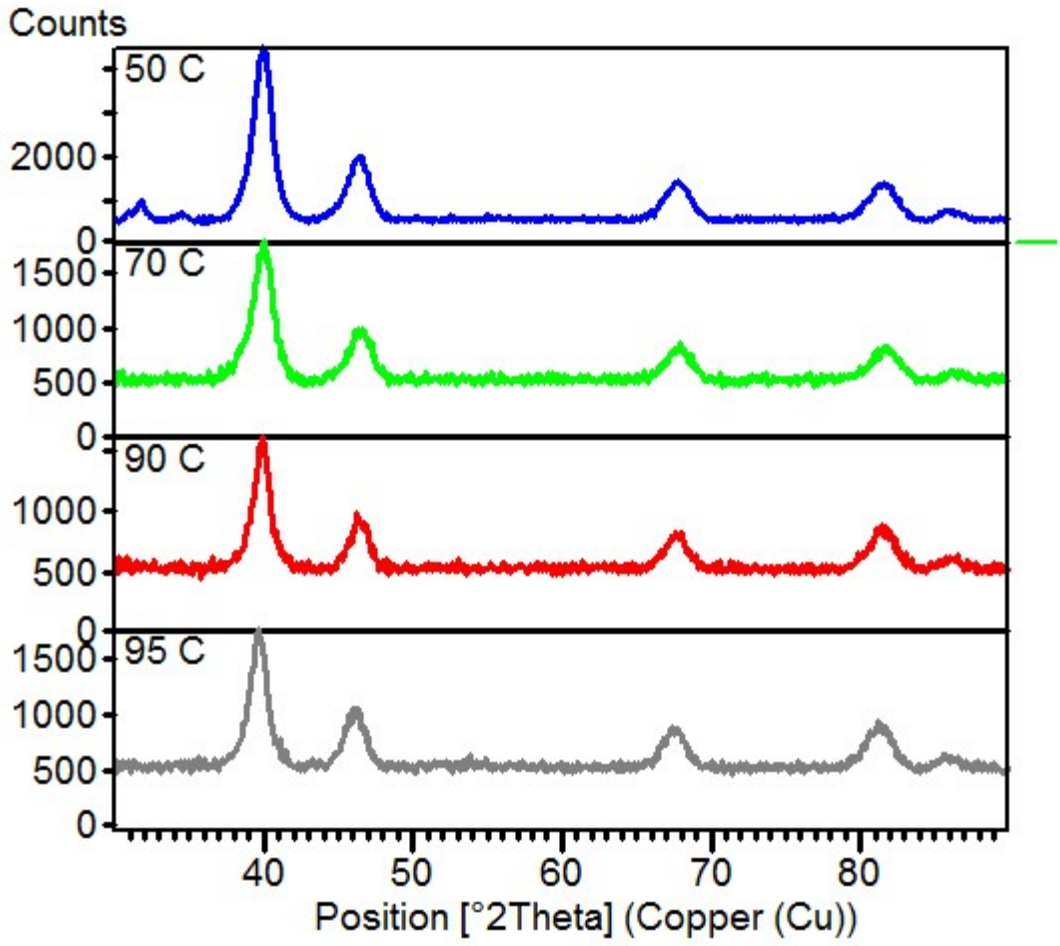

Figure 40 XRD spectra of platinum nanoparticles synthesized at different temperatures

Table 8 Crystallite size, hydrodynamic radius, and PDI values for platinum nanoparticles synthesized at different temperatures

Temperature (°C)	Crystallite Size (nm)	Hydrodynamic radius (d.nm)	PDI
50	5.7	1083 (100%)	0.552
70	5.2	22.68 (100%)	0.167
90	6.9	47.56 (95.9%)	0.244
95	6.6	27.45 (65.6 %) 79.31 (34.2%)	0.261

5.4.1.2. pH

pH had the greatest affect on the reaction time of the platinum nanoparticles. Platinum metal does not have a plasmon in the visible range, making it difficult to study the formation of platinum nanoparticles *in situ*.[52] However, K_2PtCl_4 does show absorption peaks in the visible range that can be examined and watched disappear as nanoparticles are formed. As the nanoparticles form, the solution turns a dark color, raising the overall absorption of the solution background. Figure 41 shows the UV/VIS spectrum of K_2PtCl_4 solution before and after reduction.

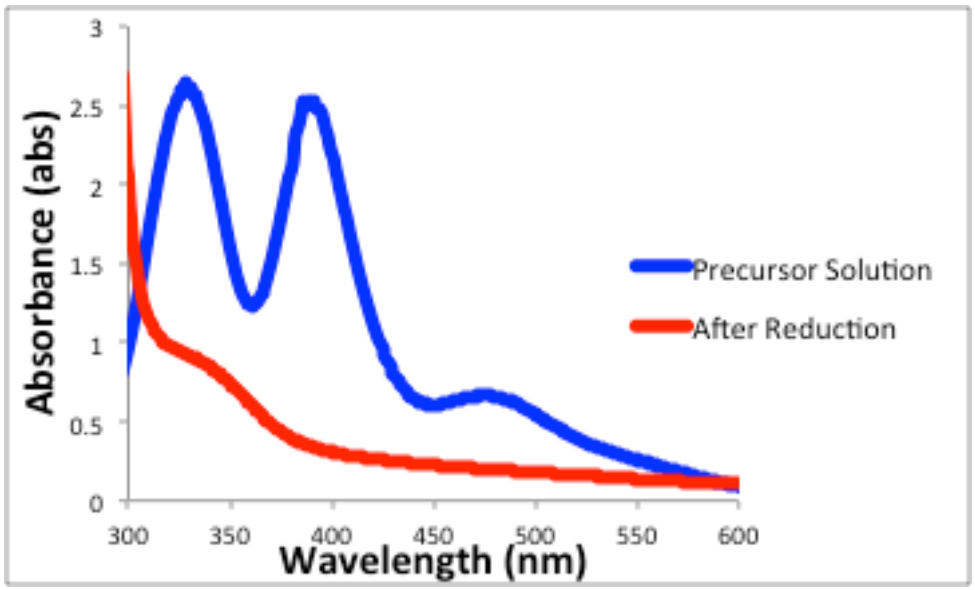

Figure 41 UV/VIS spectrum of K_2PtCl_4 solution before and after reduction

To see how pH affected the reaction time, flow UV/VIS was used. In this set of experiments, the pH of the solution was varied to pH of 5 shown in Figure 42, pH of 8 shown in Figure 43 , and a pH of 10 shown in Figure 44. From each figure, the time where reduction began was determined from the time where the increase in the baseline absorption was observed. Since the absorption was above 4 abs towards the end of the reaction, the time where reduction was completed was difficult to quantify. Table 9 displays the time reduction started and reached an equilibrium based on absorbance at each pH.

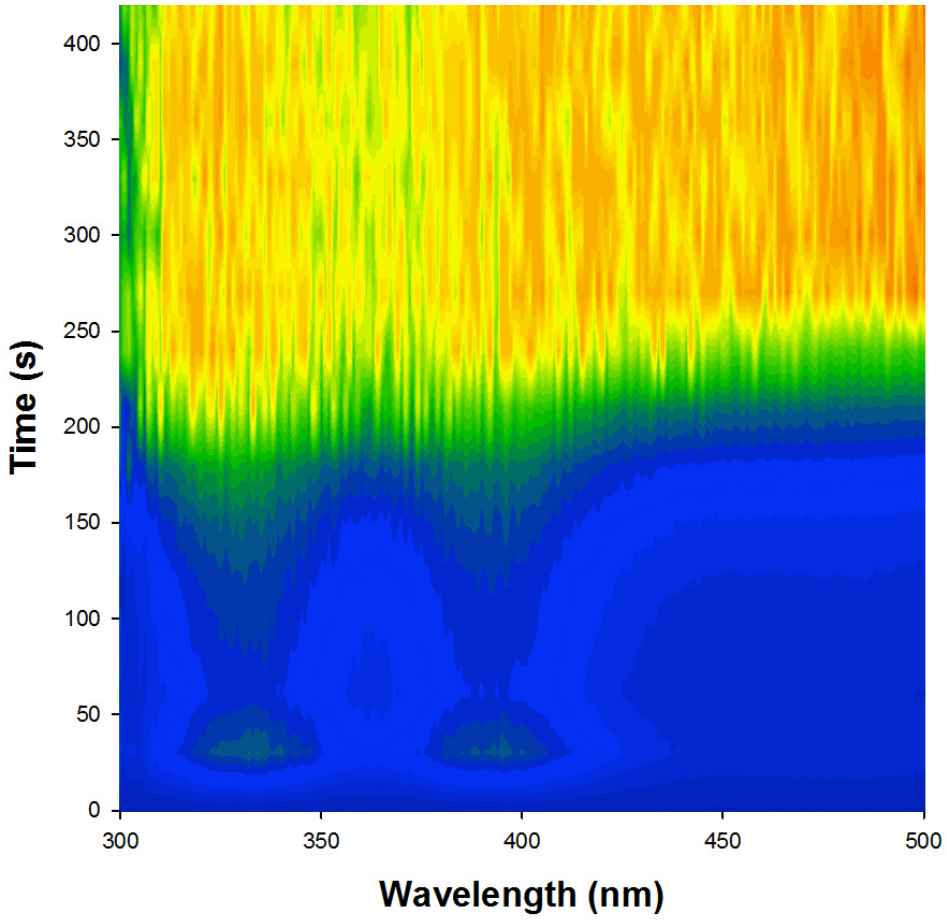

Figure 42 Flow UV/VIS of platinum nanoparticles synthesized at a pH of 5

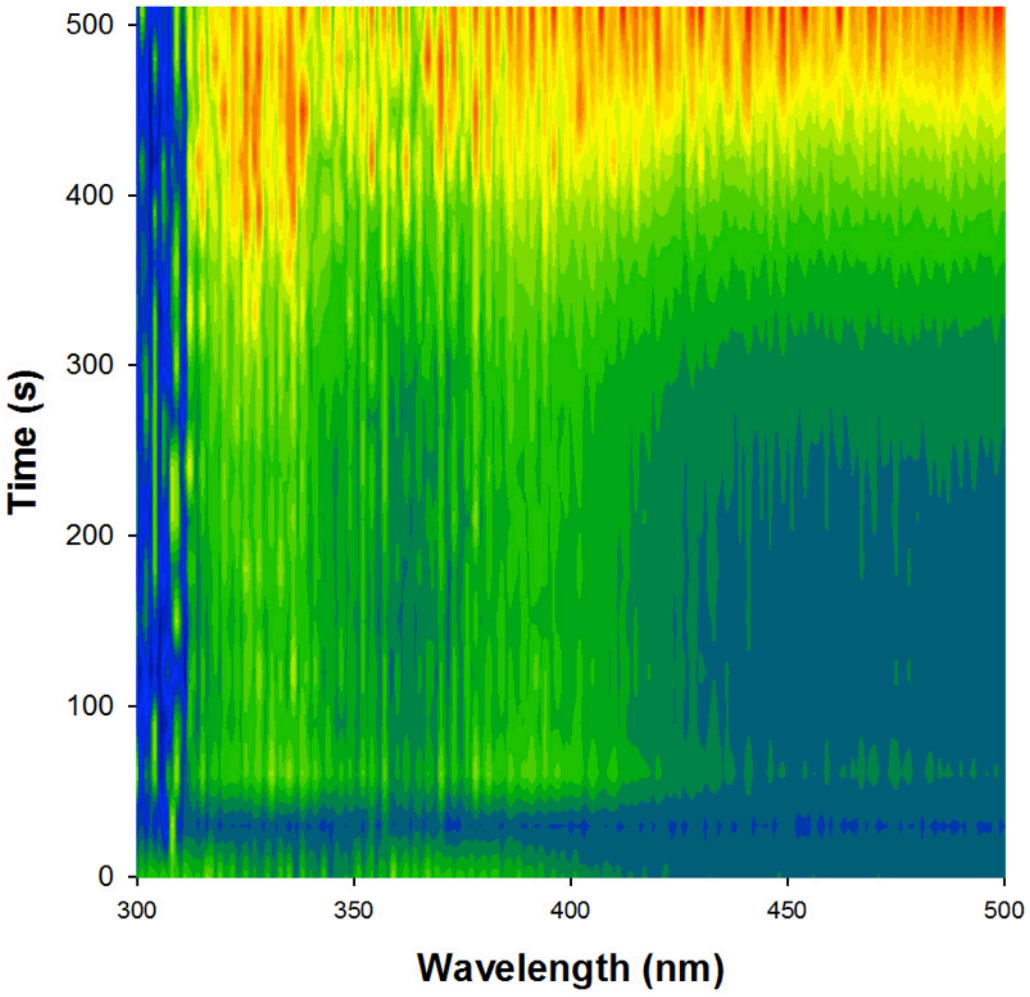

Figure 43 Flow UV/VIS of platinum nanoparticles synthesized at a pH of 8

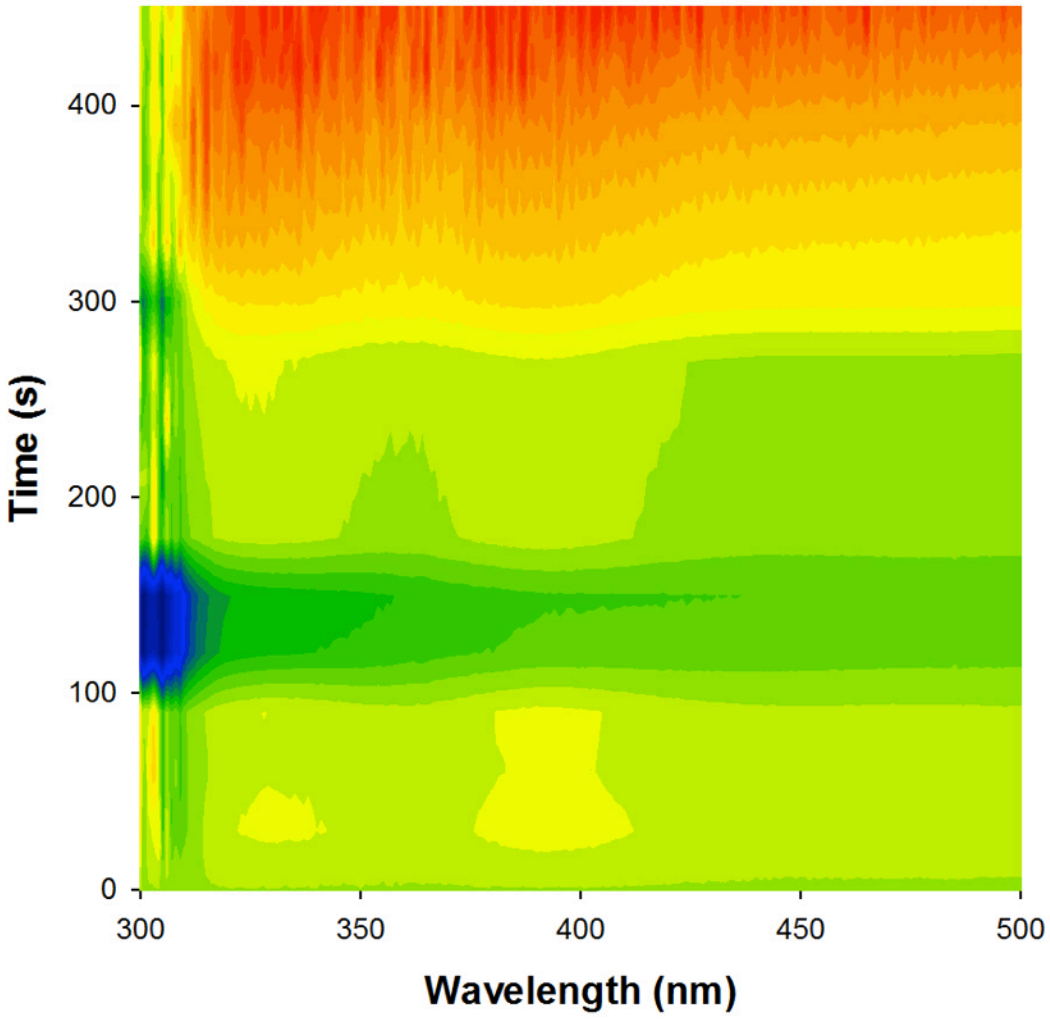

Figure 44 Flow UV/VIS of platinum nanoparticles synthesized at a pH of 10

Table 9 Reduction time from UV/VIS data at different pHs

pH	Start reduction (min)	End reduction (min)
5	3.5	4
8	5	7
10	5	6.5

Based on the UV/VIS data collected in Table 9, a pH of 10 appeared to control the nucleation and growth of the platinum nanoparticles with the greatest efficiency. Since ascorbic acid as to pKa values of 4.17 and 11.79 as shown in Figure 45, the pH will affect which form is the major form present. In order for ascorbic acid to act as a reducing agent, the vinylic hydrogen has to be removed.

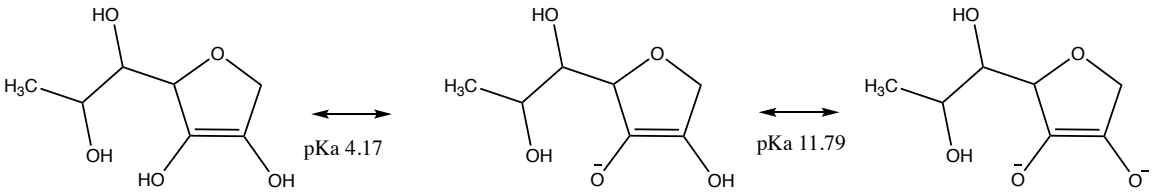

Figure 45 Schematic of ascrobic acid at different pH values

5.4.2. Optimization of conventional microwave synthesis

5.4.2.1. pH

To see if microwave irradiation affected the optimal pH compared to benchtop reactions, the reaction was completed at 3 different pH values. Table 10 shows the results using different pHs with microwave irradiation. Similarly to the benchtop reactions, a pH of 8 resulted in platinum nanoparticles with a small hydrodynamic radius of 5.3 d.nm. However, the PDI value revealed that the most monodisperse platinum nanoparticles were synthesized with a pH of 6. This could suggest that the platinum nanoparticles synthesized at a pH of 6 are larger, but more monodisperse. Moving forward, the reactions were run at a pH of 10.

Table 10 Hydrodynamic radius and PDI values for platinum nanoparticles synthesized at different pHs with microwave irradiation

pH	Hydrodynamic radius (d.nm)	PDI
6	152 (100%)	0.228
8	5.337 (99.7%), 70.63 (0.3%)	0.537
10	6.204 (99.9%) 104.7 (0.1%)	0.609

5.4.2.2. Surfactants

One of the most common ways to control a nanoparticles size and shape is with the use of a surfactant. In this section, the identity of the surfactant was varied keeping all other reaction parameters constant. Several hydrophilic surfactants were tested to see which surfactant would afford a stable colloid of small, monodisperse platinum nanoparticles with the 18 wt % surfactant with the results shown in Table 11. When CTAB and PEG 4,000 were used, the platinum nanoparticles had a large hydrodynamic radius and did not afford a stable colloid of platinum nanoparticles. The platinum nanoparticles synthesized using PEG 2,000 did form small monodisperse nanoparticles, but were not as stable in water and aggregated based on the TEM image in Figure 46B. The platinum nanoparticles synthesized with different PVP of different weights provided stable colloids with PVP K10 showing platinum nanoparticles with the smallest hydrodynamic radius of 4.9 d.nm. The TEM image in Figure 46A shows platinum nanoparticles that did not aggregate. When a larger PVP was used, the polydispersity increased. Based on the information gathered and displayed in Table 11, PVP K10 is the best choice for surfactant. PVP has been used to cap platinum nanoparticles in colloidal systems.[133-134]

Table 11 Hydrodynamic radius and PDI values of platinum nanoparticles synthesized with different surfactants with 18 wt% surfactant with microwave irradiation

Surfactant	Hydrodynamic radius (d.nm)	PDI
CTAB	85.9 (74.8%) 194 (25.2%)	0.273
PEG 2,000	12.2 (99.8%)	0.231
PEG 4,000	n/a	n/a
PVP K10	4.9 (99.6%)	0.543
PVP K58	6.2 (99.8%)	0.668
PVP K358	10.8 (97.5%) 27.98 (2.4%)	0.706

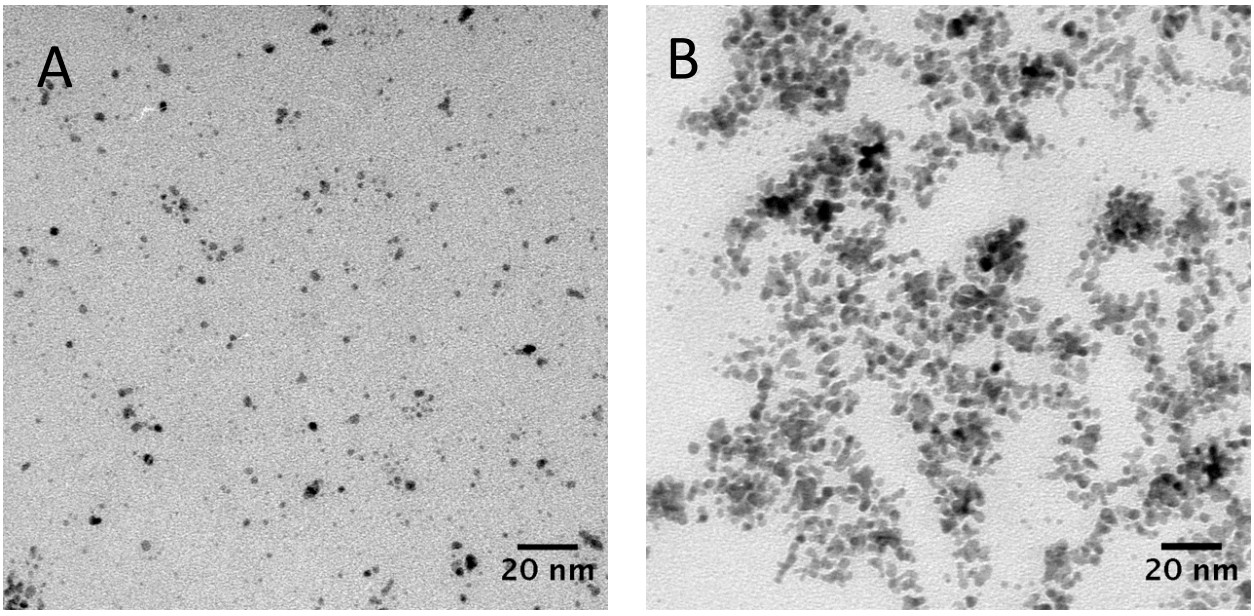

Figure 46 TEM images of platinum nanoparticles synthesized with A. PVP K10. and B. PEG 2,000.

The amount of PVP K10 was varied during the synthesis of platinum nanoparticles synthesized with microwave irradiation and size data from DLS is shown in Table 12. Without PVP K10, the platinum nanoparticles were relatively monodisperse, but displayed a hydrodynamic radius of 18 d.nm. With the addition of PVP K10, the hydrodynamic radius of the platinum nanoparticles decreased. When the wt % of PVP K10 was 25, the platinum nanoparticles were more polydisperse with a PDI value of 0.414. When 9 and 18 wt % of PVP K10 were used in the reaction, the resulting platinum nanoparticles had the smallest PDI value with small hydrodynamic radius. This data shows that a minimal amount of PVP is needed to control the size of the platinum nanoparticles. Once that amount is met, the excess PVP does not affect the size based on the hydrodynamic radius. The optimal amount of PVP K10 was determined to be between 9 and 18 wt %.

Table 12 Hydrodynamic radius and PDI values of platinum nanoparticles synthesized with different amounts of PVP K10 with microwave irradiation

Wt % PVP K10	Hydrodynamic radius (d.nm)	PDI
25	6.1 (99.8%)	0.414
18	4.9 (99.6%)	0.543
9	5.1 (99.4%)	0.227
4.5	8.8 (98.9%) 51.6 (1.1%)	0.333
0	18.2 (99.7%)	0.246

To confirm that the hydrodynamic radius was indicative of particle size, scanning transmission electron microscopy (STEM) was completed. The images are shown in Figure 47. The image shows platinum clusters with diameters of 20-28 nm made of platinum nanoparticles about 3 nm in size. This showed that the hydrodynamic size of 19 d.nm was more indicative of cluster size.

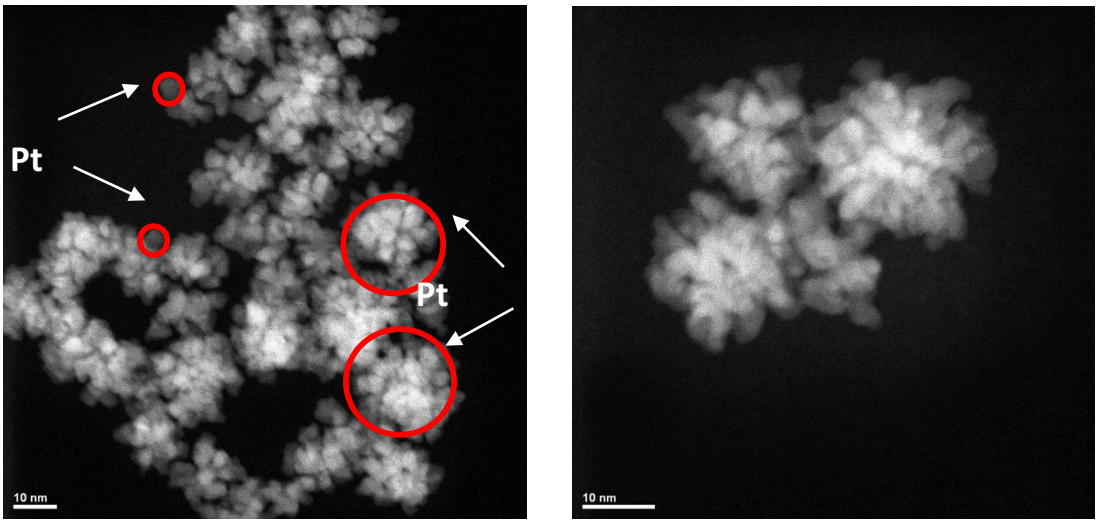

Figure 47 STEM images of platinum nanoparticles synthesized using conventional microwave

5.4.3.Optimization of continuous flow capillary microwave synthesis

Flow reactors have several parameters that can be optimized. In this work, the microwave settings, resonance time, pH, and temperature were optimized for the synthesis of platinum nanoparticles synthesized using the microwave flow reactor described in 5.3.3.

5.4.3.1. Microwave Wattage Settings

The CEM discover microwave can be run under different wattage settings. With fixed wattage, the wattage output is held constant for the entirety of the reaction time no matter the reaction temperature. The CEM discover can also be run under dynamic mode. With this mode, the microwave wattage is varied to keep a constant temperature.

Under fixed wattage, the temperature of the aqueous solution reached and stayed relatively stable at 107 °C. DLS analysis revealed that the hydrodynamic radius of nanoparticles in solution were 78.5 d.nm based on volume measurements and is shown in Table 13. TEM images, shown in Figure 48, show a wide size range and morphology including smaller nanoparticles and rods.

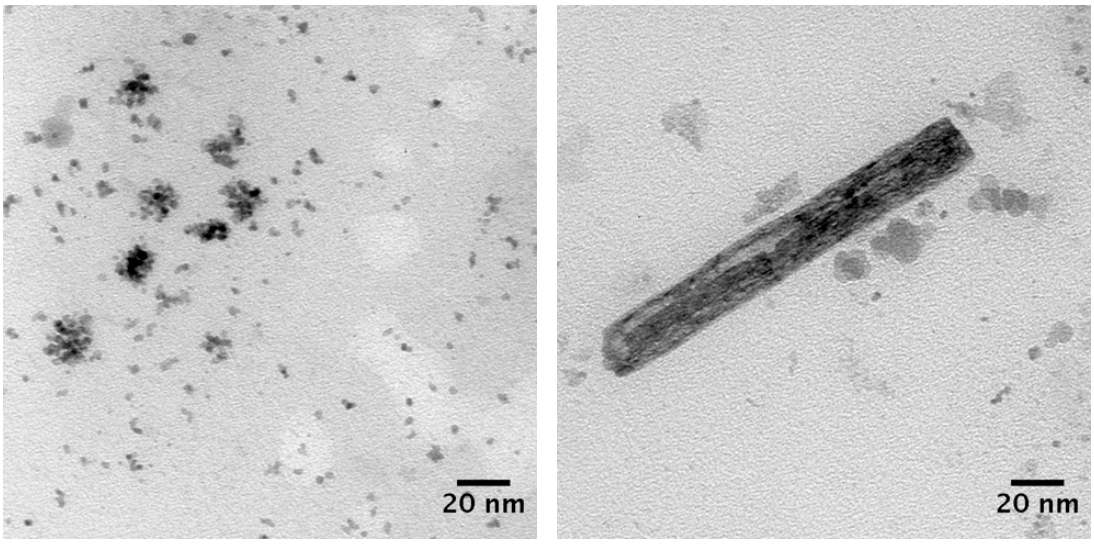

Figure 48 TEM images of platinum nanoparticles synthesized under a fixed wattage of 300 W

When run with dynamic microwave heating, the temperature of the reaction was kept constant at 95 °C. The resulting platinum nanoparticles were much smaller with an observed hydrodynamic radius of 11 d.nm. TEM images, shown in Figure 49, show more monodisperse nanoparticles, which is in agreement with the PDI value obtained from DLS. Table 13 shows the hydrodynamic radius and PDI values for the platinum nanoparticles synthesized with both dynamic and fixed wattage microwave settings. Based on these results, dynamic wattage setting was determined as the optimal setting. This is constant with literature that found that dynamic settings increased the rate of nucleation and growth of nanoparticles.[66]

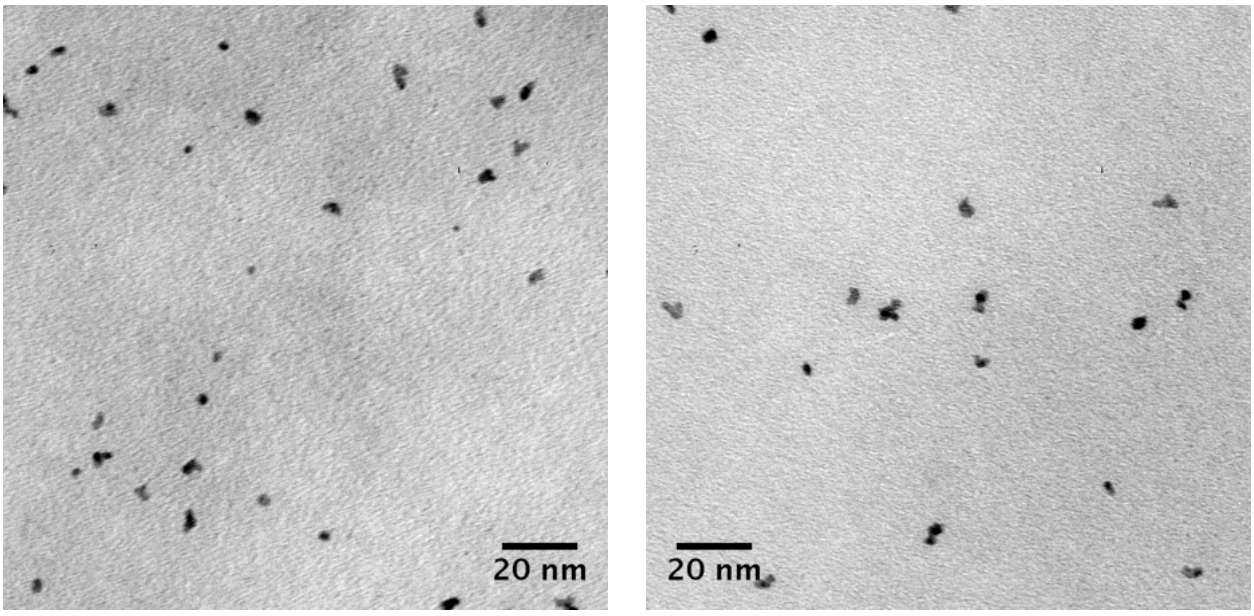

Figure 49 TEM images of platinum nanoparticles synthesized under dynamic wattage

Table 13 Hydrodynamic radius and PDI values for platinum nanoparticles synthesized with different microwave settings

Microwave wattage setting	Temperature (°C)	Hydrodynamic radius (d.nm)	PDI
Fixed	107	78.5 (99.3%)	0.379
Dynamic	95	11.0 (99.9%)	0.125

5.4.3.2. Resonance Time

The most common way to control the reaction time is by altering the resonance time of the precursor solution in the capillary. The resonance time can be modified by altering either the flow rate or the length of the reaction coil. By altering the length of the reaction coil, the inner volume changes. Table 14 shows the results from changing the resonance time of the platinum precursor solution under microwave irradiation at 90 °C. When the resonance time was 2 minutes, no reduction of platinum was observed. When the resonance time was increased to 4 minutes by decreasing the flow rate, reduction was seen 10 minutes after the platinum solution

was passed through the microwave cavity. It is believed that the 4 minutes the platinum solution was under microwave irradiation provided an induction period. With a resonance time of 8 minutes, the solution was brown/black when exiting the capillary revealing that the platinum precursor had been reduced. DLS revealed that the nanoparticles were of a small, monodisperse morphology. Figure 50 shows a TEM image of the nanoparticles synthesized with a resonance time of 8 minutes. The image shows that the nanoparticles are aggregating, but are of small sizes.

Table 14 Hydrodynamic radius and PDI values for platinum nanoparticles synthesized with different resonance times

Flow rate mL/min	Inner volume of coil (mL)	Resonance time (min)	Reduction?	Hydrodynamic radius (d.nm)	PDI
1	1.96	2	no	n/a	n/a
0.5	1.96	4	after 10 min	13.0 (100%)	0.210
1	4.2	8	yes	10.7 (100%)	0.234

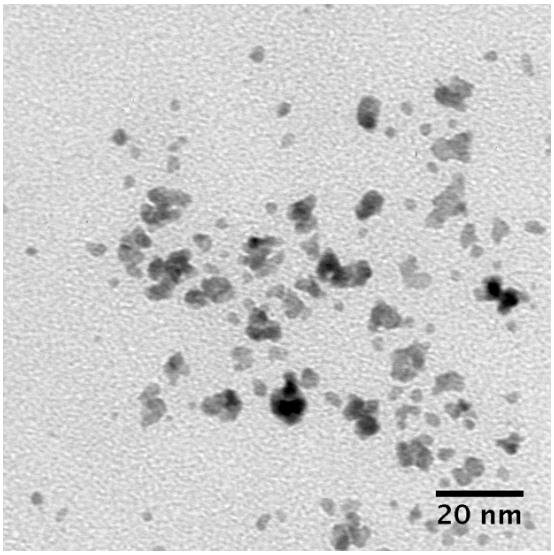

Figure 50 TEM image of platinum nanoparticles synthesized with a resonance time of 8 minutes

5.4.3.3.Temperature

The temperature was ranged from 80 °C to 100 °C at 5 °C increments keeping all other parameters constant. Table 15 displays the observed hydrodynamic diameter measured from DLS and particle diameters measured from TEM images shown in Figure 51. At 80 °C, a longer resonance time is needed to reach supersaturation for nucleation to take place. At temperatures between 85 and 95 °C, formation of platinum nanoparticles was observed with the higher temperatures resulting in particles with smaller hydrodynamic radii and lower polydispersity. At 100 °C, the water in the tubing boiled, causing the solvent to flow efficiently through the reactor. The optimal temperature was determined to be 90 °C and was used in all further reactions.

Table 15 Hydrodynamic radius, PDI and TEM size data for platinum nanoparticles synthesized at various temperatures

Temperature (°C)	Hydrodynamic radius (d.nm)	PDI	TEM size (nm)
80	No reduction	No reduction	n/a
85	15.53 (96.1%)	0.433	2.5 ± 0.9
90	10.1 (100%	0.143	2.66 ±0.56
95	9.4 (99.9%)	0.247	2.50 ±0.54
100	10.1 (99.4%)	0.227	n/a

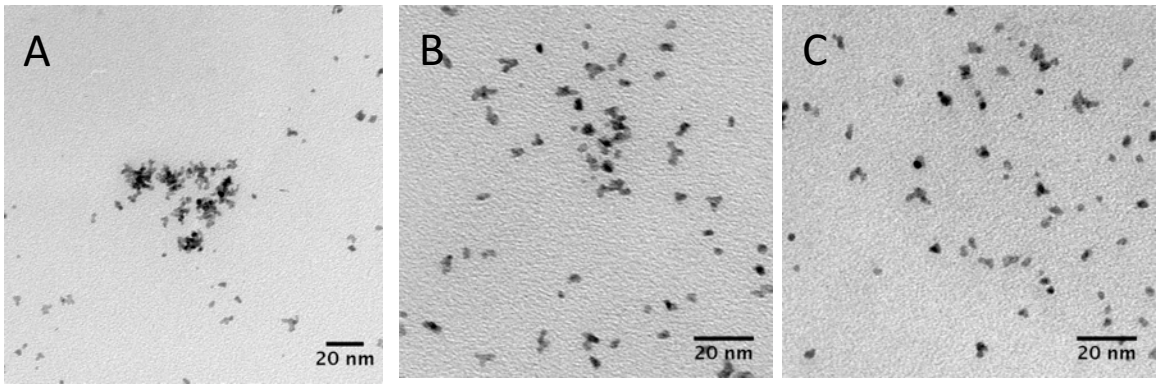

Figure 51 TEM images of platinum nanoparticles synthesized at A. 85 °C B. 90 °C and C. 95 °C

5.4.3.4. pH

Similarly to the optimization performed with conventional heating and conventional microwave heating, pH had a great affect on the synthesized platinum nanoparticles. For this set of reactions, the resonance time, temperature, and concentration were all held constant. The pH was adjusted with either 0.1 M NaOH or 0.1 M HCl and the results are shown in Table 16. Ascorbic acid has to pKa values at 4.1 and 11.8. In most research using ascorbic acid as a reducing agent, the pH is commonly adjusted between 9 and 10. As expected, when the pH was adjusted lower than the pKa of ascorbic acid, no reduction took place. In order for ascorbic acid to act as the reducing agent, the most acidic hydrogen must dissociate. At the highest pH tested of 11.07, no reduction was seen because a majority of both hydrogens were dissociated. Figure 52 shows the nanoparticles synthesized at a pH of 5.8, 6.5 and 9.1. The images show that at all pH values, small platinum nanoparticles were obtained. Based on the hydrodynamic radius and PDI values, the optimal pH was 6.5. This was the unadjusted pH sample. This could be because with more ions in solution from adjusted the pH, the water molecules were held in a fixed position.

Table 16 Hydrodynamic radius and PDI values for platinum nanoparticles synthesized at different pHs

pH	Hydrodynamic radius (d.nm)	PDI
2.7	No reduction	n/a
5.8	9.1 (99.9%0	0.223
6.5	6.4 (99.7%)	0.143
8.05	6.9 (99.8%)	0.749
9.1	7.71 (99.8%)	0.306
11.07	No reduction	n/a

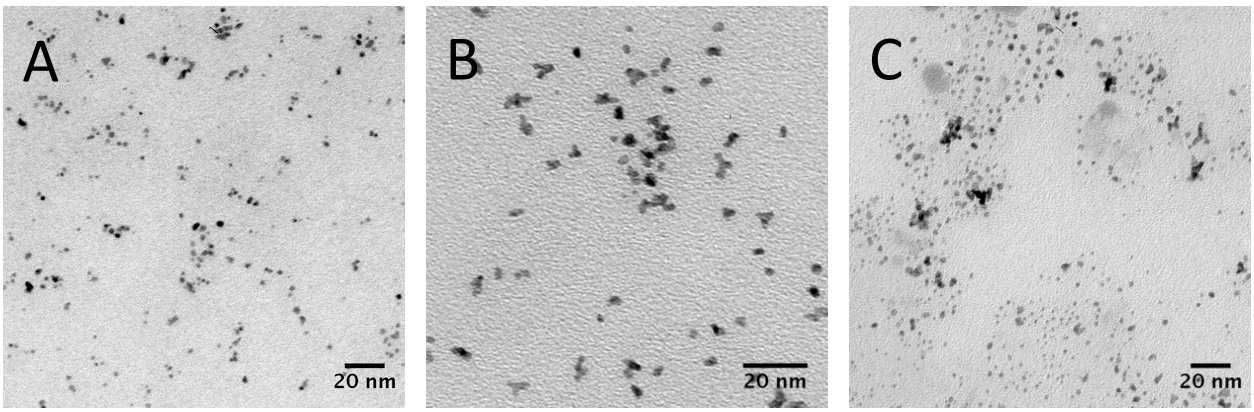

Figure 52 TEM images of platinum nanoparticles synthesized at a pH of A. 5.8 B 6.5, and C 9.1

5.4.3.5.Concentration of Metal Precursor

The last parameter investigated was the concentration of precursors in solution. To be more cost efficient, the reaction should be run at the highest concentration of precursors as possible that maintains the small size and low polydispersity. Table 17 shows the measured hydrodynamic radius and PDI value for reactions run with different concentrations of K_2PtCl_4. As the concentration of precursors was increased, the PDI increased as well. The reaction could

be completed with 7.6 mM of K_2PtCl_4 while maintaining the small size. Figure 53 shows the TEM images of platinum nanoparticles synthesized with 2.9 and 7.6 mM K_2PtCl_4. The reaction run with 7.6 mM K_2PtCl_4 were 2.5 ±0.7 nm and were comparable to the reaction run at a lower concentration.

Table 17 Hydrodynamic radius, PDI and TEM diameters of platinum nanoparticles synthesized at different mM of K_2PtCl_4

mM K_2PtCl_4	Hydrodynamic radius (d.nm)	PDI	TEM (nm)
9.9	17.0 (99.7%)	0.775	n/a
7.6	5.83(99.9)	0.252	2.53 ±0.7
4.9	8.0 (99.8%)	0.746	n/a
2.9	4.4 (87.6%) 10.7 (12.4%)	0.398	1.67± 0.45 2.91± 0.52
1.4	10.1 (99.4%)	0.143	2.66 ±0.56
0.5	n/a	n/a	n/a

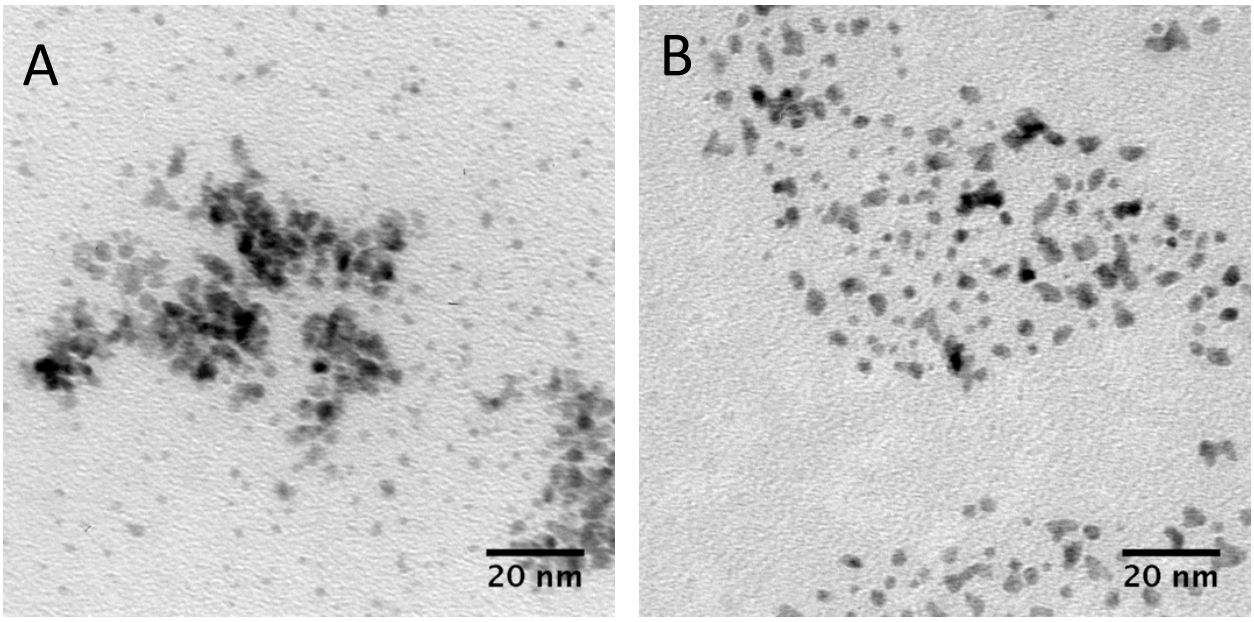

Figure 53 TEM images of platinum nanoparticles synthesized with A 2.9 mM K_2PtCl_4 and B 7.6 mM K_2PtCl_4

5.4.4. Optimal Conditions

Based on all the optimization reactions, the optimal conditions were determined to be a resonance time of 8-10 minutes, a pH of 6.5, reaction temperature of 90 °C, PVP K10 as the surfactant, and a metal concentration of 7.6 mM.

Table 18 shows the size data obtained by DLS and TEM. With more surfactant present, the PDI value was much lower, suggesting that with more surfactant, the resulting nanoparticles are more monodisperse. However, the TEM images, shown in Figure 54, show nanoparticles of roughly the same size of 1.7 nm. The difference in PDI values could be from a difference in the polymer coating on the surface of the nanoparticles.

Table 18 Hydrodynamic radius, PDI, and TEM sizes of platinum nanoparticles synthesized with microwave flow

PVP (g)	Hydrodynamic radius (d.nm)	PDI	TEM size (nm)
0.15	7.3 (97%)	0.297	1.76 ± 0.5 nm
0.07	7.0 (99%)	0.831	1.74 ± 0.4 nm

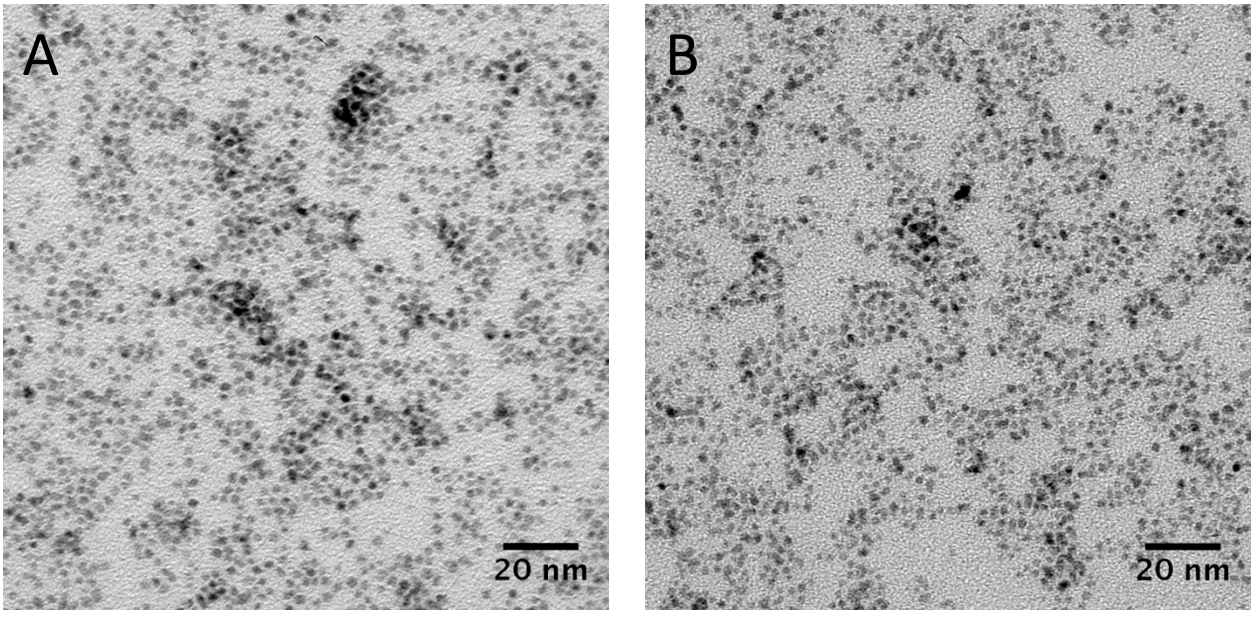

Figure 54 TEM images of platinum nanoparticles synthesized with A 18 wt % and B 9 wt % PVP K10

5.4.5. Organic Removal

In catalytic reactions, the number of active sites on the catalyst is directly related to its activity. The presence of an organic layer on the surface of a catalyst could decrease its catalytic activity.[38, 135-136] Therefore, it is important to study what conditions are needed to remove the organic layer. To determine at what temperature excess organic is burned off the platinum nanoparticles, temperature programmed oxidation (TPO) was performed. The colloidal sample was prepared by removing the water with a rotovap without any cleaning steps affording a tar-like sample of platinum and frozen in liquid nitrogen to make the sample more powder like and added to quartz wool. TPO was performed from 30-600 °C with a gas composition of 10% ultra high purity O_2 balanced with helium with a total flow of 20 SCCM. By measuring the amount of CO_2 and H_2O evolved with by mass spectroscopy, the oxidation of PVP can be monitored. Figure 55 shows that H_2O, with a mass of 18, forms first indicating that oxidative dehydrogenation of PVP is more facile then oxidative hydrogenolysis of C-C bonds to form CO_2, with a mass of 44. At 600 °C, large amounts of CO_2 were produced with a simultaneous decrease in O_2 from the feed stream, shown with a mass of 32. During the soak at 600 °C with a time of 60-120 minutes in Figure 55, the CO_2 and O_2 returned to normal concentrations based on the feed stream. This suggests that the platinum surface is now clean and the PVP has been removed. Based on that there appears to be two stages of oxidation at 100-450 °C and at temperatures above 500 °C suggests that the first temperature range is due to platinum assisted combustion of PVP from PVP that is in contact with the surface and the second temperature is due to combustion of PVP without platinum assistant.

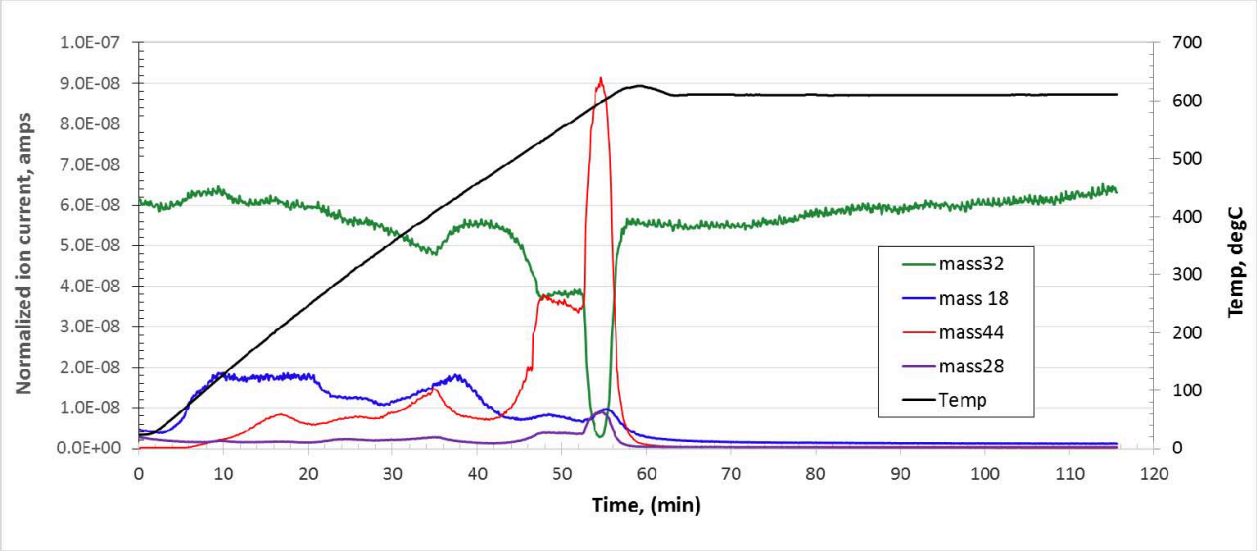

Figure 55 TPO of platinum nanoparticles from 30-600 °C and then held at 600 °C for 1 hour

Since PVP contains nitrogen, the oxidation can also be followed with the formation of NO_x and is shown in Figure 56. NO was formed at 123 °C and 410 °C, suggesting that platinum assisted dinitrogenation is fairly easy.

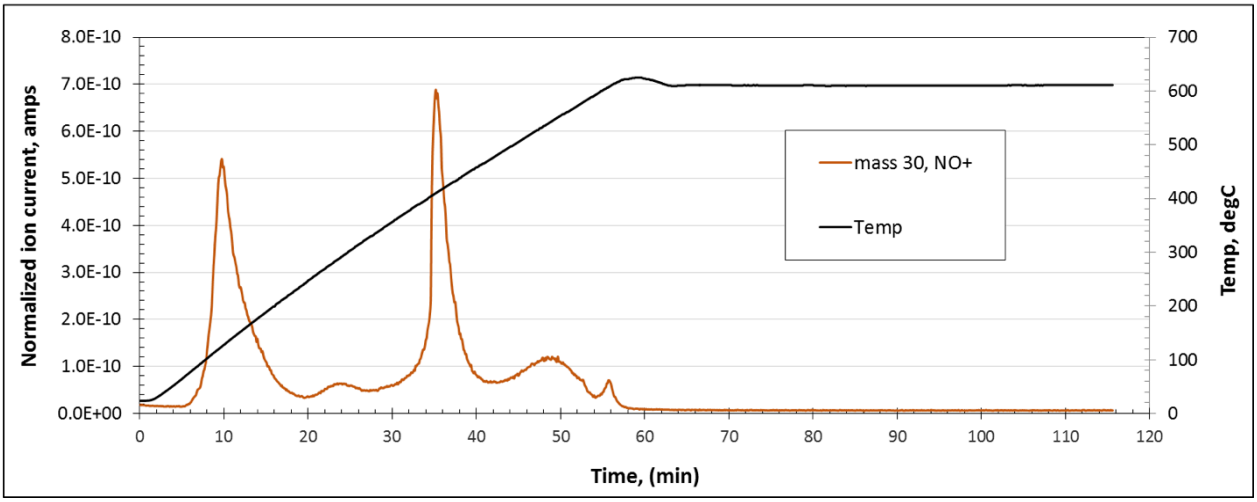

Figure 56 TPO of platinum nanoparticles from 30-600 °C and then held at 600 °C for 1 hour following the formation of NO_x with a mass of 30

To see if the TPO reactions altered the size of the platinum nanoparticles, an XRD spectrum of the nanoparticles was obtained and is shown in Figure 57. The platinum

nanoparticles have sintered to a particle size between 20-25 nm. This suggests that during synthesis, less PVP should be used or a more easily oxidized surfactant such as PVA should be used because such a high temperature is needed to remove the PVP from the surface.

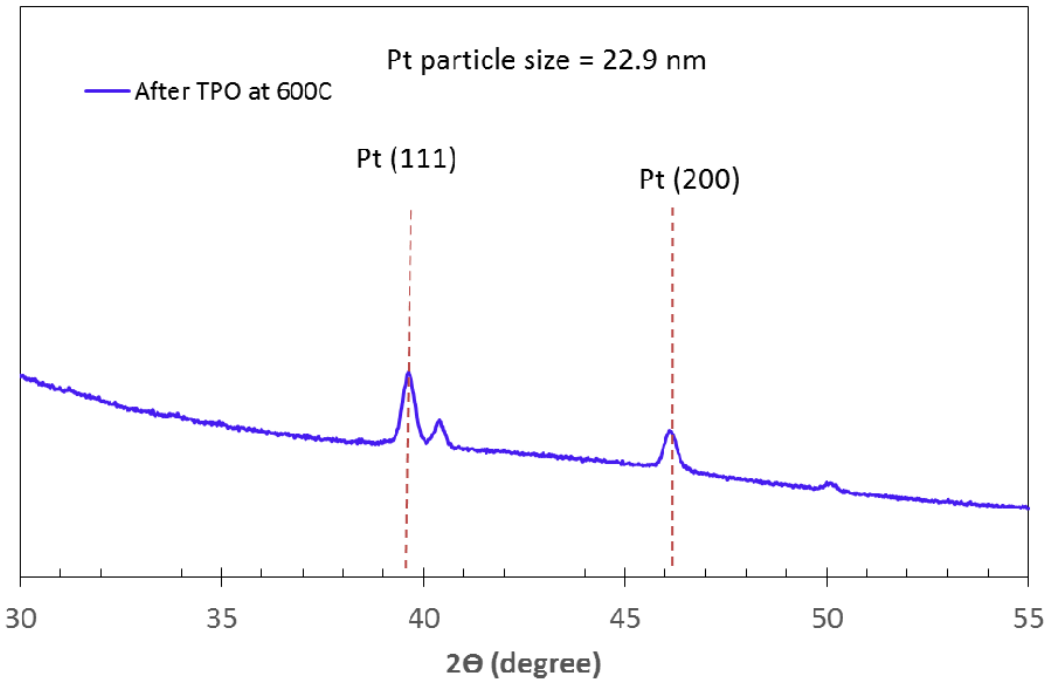

Figure 57 XRD spectrum of platinum nanoparticles after TPO at 600 °C

5.4.6.Hydrogenation of Octene

Hydrogenation of octene, shown in Figure 58, was completed using the synthesized platinum nanoparticles without the removal of PVP. Platinum nanoparticles synthesized by microwave continuous flow, microwave low continuous stir tank reactor, and by conventional heating on benchtop were tested for activity. During the reaction, an aliquot was taken at 15 and 30 minutes of reaction time to see how much of the octene had been converted to octane at the given reaction time. Figure 59 shows the uptake of H_2 as a function of time. From the graph, it can be inferred that platinum nanoparticles synthesized using microwave continuous flow have a

greater rate of catalytic activity. Table 19 shows the % conversion at 15 and 30 minutes, and the initial rate per mmol of platinum catalyst. The initial rate was found by the slope from the first 15 minutes of reaction time in Figure 59. The initial rate data reveals that the two reactions run using platinum synthesized by continuous microwave flow exhibited the fastest initial rate followed by platinum nanoparticles synthesized by conventional heating on benchtop. The reason for this is still under investigation.

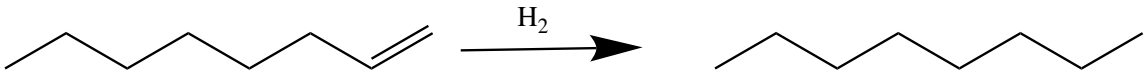

Figure 58 Schematic of the hydrogenation of octene to octane

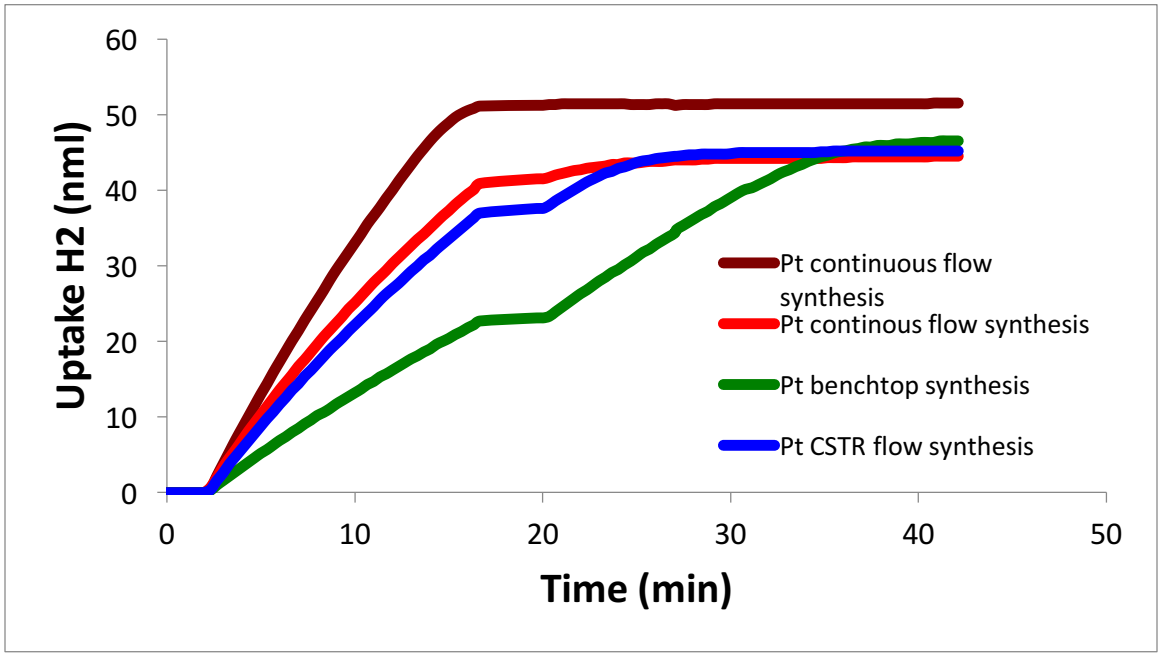

Figure 59 Uptake of H_2 as a function of time for platinum nanoparticles synthesized in microwave flow, benchtop conventional heating, and platinum using a CSTR microwave flow

Table 19 Comparison of hydrogenation of octene using several platinum catalysts

	No catalyst	Pt flow no octene	Pt Flow (l)	Pt Flow (s)	Pt bench (s)	Pt CSTR (l)
Total H_2 uptake at 30 min (nml)	2.1	1.4	51.5	44.5	46.5	45.2
% conversion 15 min	0	0	97.69	92.76	49.33	81.29
% conversion 30 min	5.86	0	100	100	100	100
mmol Pt	0	0.006	0.006	0.0002	0.003	0.006
Initial rate (nmL H_2/min mmol Pt)	0	11.7	611.5	7593	4809	440

5.5. Conclusions

In this chapter, the synthesis of platinum nanoparticles with a continuous microwave flow reactor was investigated. The reaction was optimized using three different methods with continuous microwave flow being last. Using the optimal conditions of a pH of 5.8, PVP of 18 wt %, 90 °C, and metal concentration of 7.6 mM, platinum nanoparticles with a TEM diameter of 1.76 nm were synthesized. To remove PVP, a TPO study was performed. The removal of PVP took place over two temperature ranges. At temperatures between 150-400 °C, platinum assisted combustion of PVP takes place from PVP on the surface of the nanoparticle. At temperatures above 500 °C, combustion of PVP without platinum assistance takes place, which is likely PVP that was not bound to the platinum nanoparticle. Hydrogenation of octene reactions showed that nanoparticles synthesized using continuous flow microwave was more active based on the initial rate of the reaction. This chapter shows that nanoparticles synthesized with continuous flow

microwave reactors can be used as a catalyst and that the organic layer did not hinder the catalytic activity.

Chapter 6: Synthesis of Supported Platinum Nanoparticles onto Silica Star Supports

6.1.Overview and Motivation

In Chapter 5, colloidal platinum nanoparticles were synthesized using a continuous flow microwave reactor and were tested for catalytic activity towards the hydrogenation of octene. While the nanoparticles showed good activity, to characterize the products using GC/MS the solution was firs passed through a silica column to separate the colloidal catalyst from the products and then through a micron filter to remove any silica that may have been introduced during the silica column. To make this process more efficient and easier, the platinum nanoparticles can be put onto a support. When on a support, the recovery of the catalyst for post catalysis characterization and recyclability tests will be much simpler and efficient.

6.2. Introduction

Supported nanoparticles are some of the most common heterogeneous catalysts and are used for several catalytic reactions. They are much easier to remove from the reaction medium. Supporting materials are varied and include metal oxides, graphene, carbon nanotubes, and much more. [73-75, 86-87, 137-139] Each support offers different porosity, electronic properties, sizes, and interactions with the supported metal.

There are many methods for preparing supported nanoparticles. Some methods rely on adding synthesized nanoparticles onto the supports by wet impregnation or incipient wetness.[26, 140-141] Using wet impregnation or incipient wetness commonly lead to nanoparticles that are not firmly attached to the surface of the support. This can cause problems with metal leaching into the reaction medium.[142] It is also difficult to get an even distribution of the nanoparticle through the entire support, creating areas of high active sites and areas of low to no active sites.[140]

Other methods nucleate and grow the nanoparticle directly onto the support. When the nanoparticles are grown onto the support, they are more evenly dispersed.[140] There are many methods used to synthesize nanoparticles onto supports such as solvothermal, microwave assisted, supercritical fluids and many more.[38, 72-73, 75, 143-148] When the nanoparticles is grown directly onto the support, there are no ligands that need to be removed like when using presynthesized nanoparticles.[141] Using microwave irradiation as the heat source, the nanoparticles grown on the support are small, more evenly distributed, and of high purity.[145] By choosing supports with large loss tangent values, the support can be selectively heated, increasing the rate of nucleation of the nanoparticle onto the support by heterogeneous nucleation.

6.3.Experimental Methods

6.3.1. Incipient wetness of colloidal platinum nanoparticles onto silica star supports

Colloidal platinum nanoparticles were synthesized in similar methods to those in Chapter 5. The silica stars were determined to hold 80% of their weight in water. This weight of colloidal platinum solution was added to the silica star support and let stir for 30 minutes before putting in a vacuum oven to dry.

6.3.2. Synthesizing platinum nanoparticles onto silica support using microwave irradiation

In a typical experiment, 0.02 mmol of K_2PtCl_4 and 0.04 mmol of ascorbic acid were dissolved in 80% of the silica stars weight of DI water. In some reactions, 3 mL of hexanes was added to the water solution. The silica stars were then added to the solution and stirred for 30

minutes. After 30 minutes, the sample was microwaved at 45 °C for 2 minutes at 10 W. The silica stars were removed from the hexanes, rinsed with methanol, and put in a vacuum oven to dry overnight.

6.3.3.Characterization

The wt % of platinum on the support was determined by ICP-OES. Samples were digested for 1 hour in 1 mL of aqua regia to remove the platinum from the support and filtered to remove the support from the solution. SEM EDX was completed on a Zeiss Auriga FIB-SEM. Samples were first coated with carbon to prevent surface charging of the silica. XPS was performed on a Thermo fisher Scientific ESCALAB 250 using a monochromatic Al Kr X-ray. Samples were prepared on indium foil and the data was fit using CasaXPS software. The binding energies were calibrating by adjusting the aliphatic hydrocarbon C 1s peak to 284.6 eV.

6.4. Results and Discussion

6.4.1. Incipient wetness with colloidal platinum nanoparticles

Early work revealed that when the support was submerged in a large volume of the colloidal platinum solution, the wt % of platinum loaded on the support was low, but uniform. To increase the loading wt % of platinum, an incipient wetness method was investigated. In this method, the amount of platinum taken up by the support is controlled because only as much solution is added to the support as the support can hold. Therefore, all platinum in solution is absorbed by the support. The silica stars used in this chapter were able to absorb 75 % of their mass. First, colloidal nanoparticles were synthesized using batch microwave. These nanoparticles had a hydrodynamic radius of 25.8 d.nm and the solution was 0.22 wt % platinum. To help achieve an even coating of platinum on the support, the colloidal platinum solution was

diluted with hexanes to aid with mixing. Table 20 displays the wt % of platinum loading onto the support using this method and comparison to platinum loaded onto the support without hexanes present. The data shows that when hexane was added, the overall loading of platinum nanoparticles onto the support was larger.

Table 20 Wt % platinum onto support using incipient wetness method with and without hexanes

Preparation	Theoretical loading wt %	Wt% Pt
No hexanes	0.042	0.03
3 mL hexanes	0.041	0.05

6.4.2.Microwave synthesis of platinum nanoparticles onto silica star supports

To obtain a higher wt % of platinum on the silica star supports, the synthesis of platinum directly onto the support was investigated. Silica is known as an insulator and a poor thermal conductor. It has a low loss tangent value meaning that it will not easily convert microwave irradiation into heat. Despite this value, when the silica stars were heated using microwave irradiation, the temperature quickly rose to reaction temperatures and surpassed the set temperature. With the addition of the support, the mechanism for the formation of nanoparticles was changed from a homogenous nucleation to heterogeneous nucleation. Therefore, the reaction could be run at lower temperatures to achieved reduction of the platinum nanoparticles onto the support.

To increase the wt % platinum loaded on the supports, an incipient wetness method combined with microwave irradiation was tested. In these reactions, the support was added to a

precursor solution that was 80% of the weight of the star support. The sample was then microwaved for various times with the microwave set at 45 °C and 10 watts. Table 21 displays the wt % of platinum at the various reaction times with each sample having a theoretical wt % platinum loading of 8 %. At longer reaction times, the wt % of platinum on the support was higher suggesting more platinum had been reduced onto the support. When the 30 second reaction was repeated with a 30 minutes stir step, the wt % platinum onto the support increased from 2.4 to 5.2 wt %. This suggests that stirring the support in the precursor solution helps increase the amount of platinum nanoparticles formed on the star. However, the image shown in Figure 60 of this silica star support after microwave irradiation shows that the platinum is not evenly distributed through the support. To decrease the heterogeneity of the support, a more effective method is needed.

Table 21 Wt % platinum loaded onto the support at different reaction times

Reaction Time (min)	Wt % platinum on support
2	6.4
1	2.7
0.5	2.4

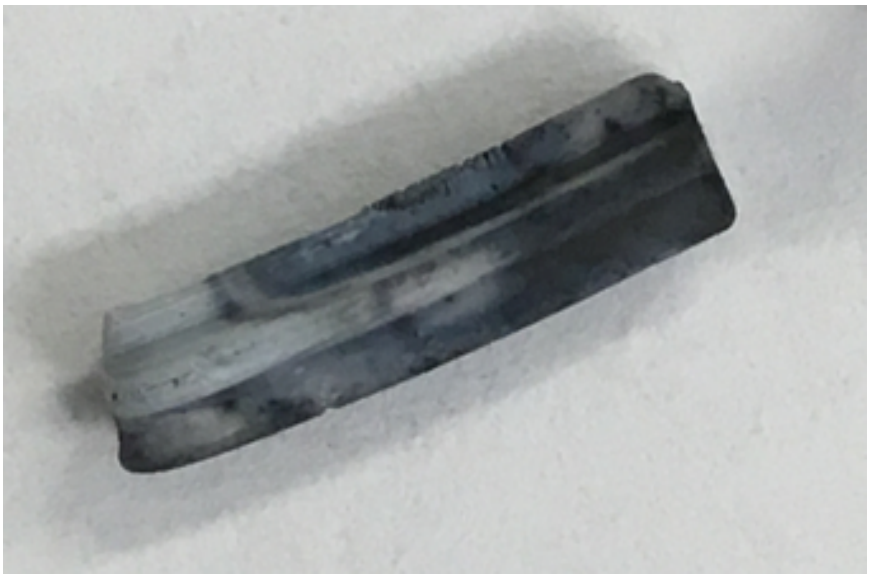

Figure 60 Image of platinum on silica support synthesized with 0.5 minutes of microwave irradiation with a 30 minute prestir step

Since the nucleation method had changed from Chapter 5, the ratio of platinum precursor to ascorbic acid and PVP K10 was investigated to see what ratios afforded a good wt % of platinum and uniform coating and the results are shown in Table 22. The optimal molar ratio of K_2PtCl_4 to ascorbic acid based on wt % of platinum loaded onto the support was 1:1. With the addition of PVP K10 to the reaction, the platinum selectively grew on the interior of the star support and an image is shown in Figure 61. To confirm that platinum was not on the outside of the star support, EDX elemental mapping was completed on a cross section of the support and is shown in Figure 62. Without PVP K10 present, the platinum nanoparticles appear more homogenous on the support as shown in Figure 63. To confirm this elemental mapping of platinum using EDX on a cross section was completed and shown in Figure 64. The elemental mapping shows a higher concentration of platinum towards the center of the star, similarly to the darker areas shown in Figure 63. This confirms that the darker coloring on the silica support is

due to platinum being present. In both samples shown, the platinum is still heterogeneous throughout the support.

Table 22 Wt % of platinum on the support at different ratios of ascorbic acid and PVP K10

Pt:AA mole ratio	Mass ratio of Pt: PVPK10	Theoretical wt % platinum	Wt % platinum on support
1:1	0	3.6	2.5
1:2	1:0.5	3.6	1.5
1:1	1:0.5	3.6	2.7
1:1	1:0.5	2	0.9

Figure 61 Image of cross section and full support of platinum on star support with PVP K10 present

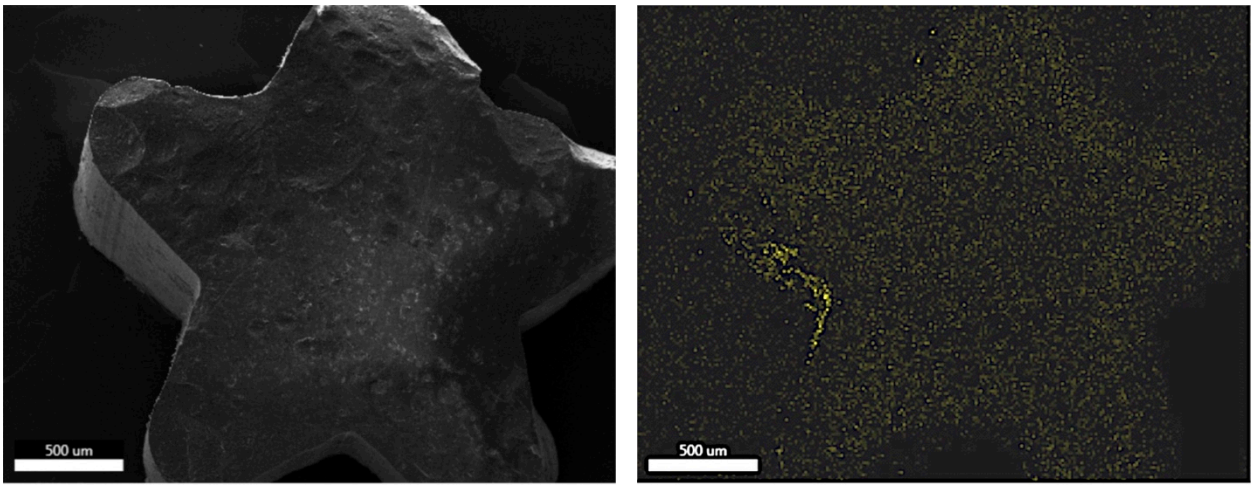

Figure 62 EDX elemental mapping of platinum for the cross section of the silica star support synthesized with PVP K10

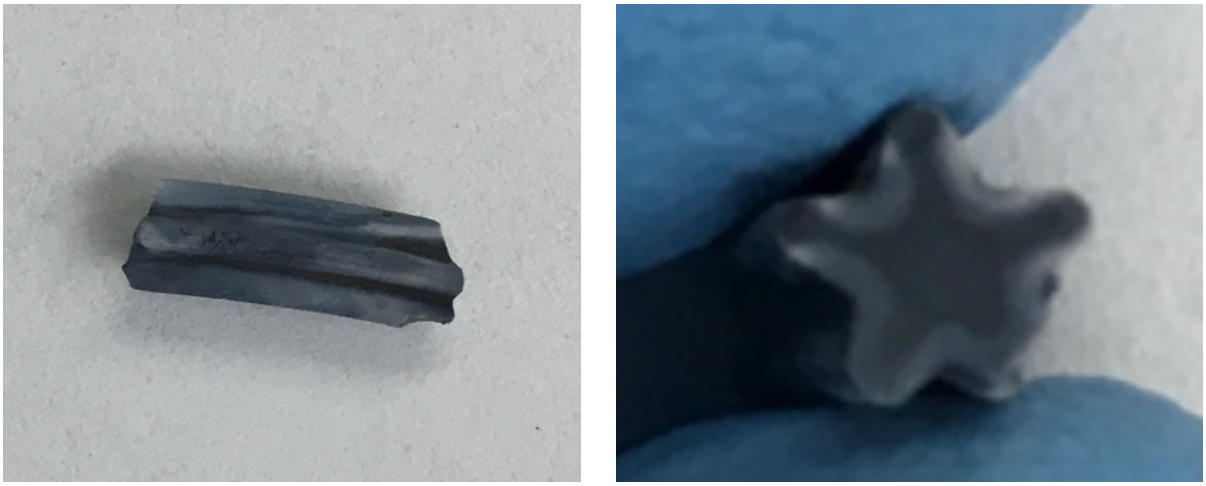

Figure 63 mage of cross section and full support of platinum on star support without PVP K10 present

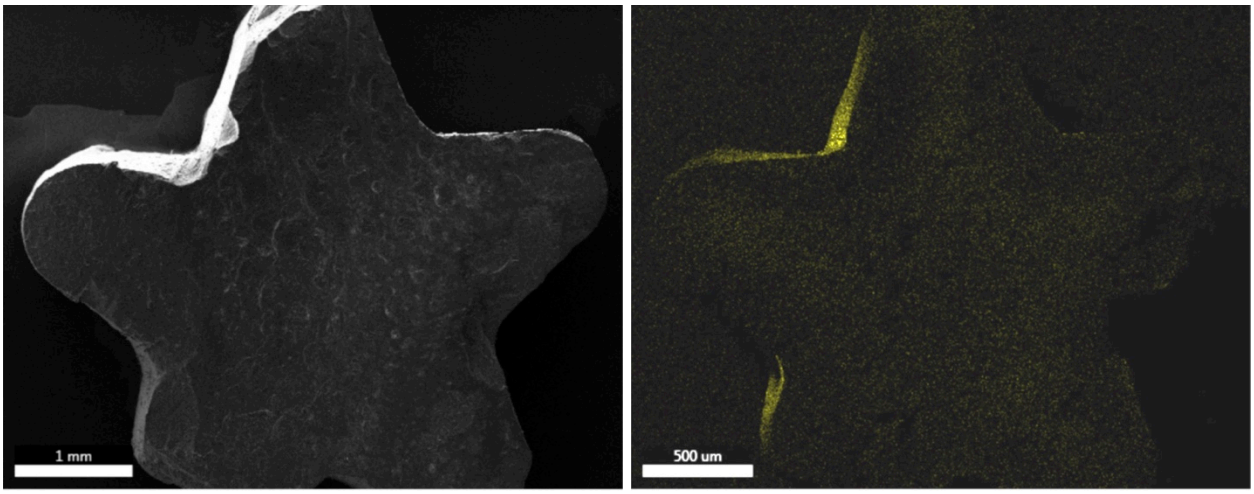

Figure 64 EDX elemental mapping of platinum for the cross section of the silica star support synthesized without PVP K10

6.4.2.1. Using hexanes as a co-solvent

Previously in this chapter, the use of hexanes as a co-solvent with the colloidal platinum solution was investigated and displayed a higher wt % of platinum on the support. With the addition of hexanes to the incipient wetness of platinum precursor solution followed by microwave irradiation, a more homogeneous distribution of platinum on the support should be achieved due to more efficient mixing. In this set of reactions, the precursors were dissolved in 80 % of the stars weight in DI water and then diluted with 4 mL of hexanes. Before microwaving, the solutions containing the stars were stirred on a hotplate. During this step, the silica stars absorbed the aqueous solution, turning the stars orange as shown in Figure 65A. After microwaving for 4 minutes at 65 °C with 10 W, the stars turned black with the hexanes remaining clear, suggesting that the platinum selectively grew onto the supports and not in the hexane as shown in Figure 65B. Using this method, the wt % of platinum was increased and appeared to be more uniform.

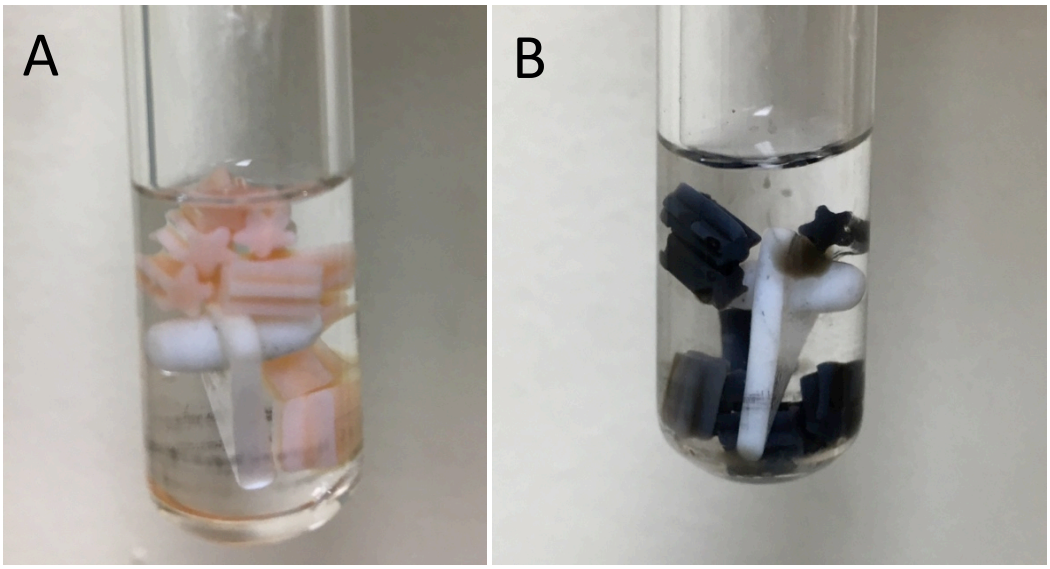

Figure 65 Image of silica stars in a solution of hexanes, DI water, and K_2PtCl_4 A. before microwave irradiation and B. After microwave irradiation

6.4.2.2. Adding Ascorbic Acid in a Second Step

With the addition of a support, the energy barrier for the nucleation of platinum nanoparticles is drastically reduced. Therefore, less reducing agent and heat is needed for nucleation to take place. In some reactions, the platinum nanoparticles reduced during the 30 minutes prestir step. To stop the premature nucleation, the ascorbic acid was added after the prestir step right before microwaving. Table 23 displays the data of platinum synthesized onto the support with and without ascorbic acid added as a second step. When ascorbic acid was added during the prestir step and reduced before microwaving, the wt % of platinum on the support was only 0.45 wt %. When added as a second step, the wt % of platinum increased to 0.81 wt %. This suggests that with ascorbic acid added as a second step, more platinum is reduced onto the support. To see if adding the ascorbic acid as a second step affected the homogeneity of platinum throughout the support, an image of the cross section of each sample from Table 23 was taken and shown in Figure 66. The images show that with ascorbic acid

added as a second step, the platinum enters further into the star, but is not evenly distributed throughout the entire cross section. When the platinum reduced before the microwave, the platinum appears to be localized more towards the edges of the cross section.

Table 23 Wt% platinum on support with ascorbic acid added as a second step

Reaction	Theoretical wt % platinum	Wt% Pt
No microwave irradiation	2.33	0.45
three step process	2.83	0.81

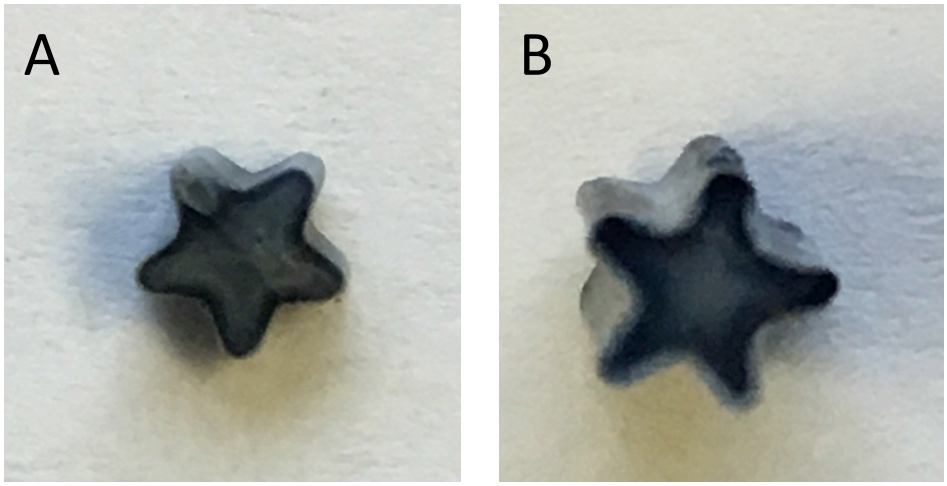

Figure 66 Cross section of A. reduced before microwave B. ascorbic acid added in a second step and microwaved

To confirm that the platinum precursor was reduced to platinum metal and not an oxide phase, XPS was completed on the silica star support after loading with platinum and is shown in

Figure 67. When ascorbic acid was added during the prestir step and reduced without microwave irradiation, the platinum binding energy was 71.2 eV showing the platinum was Pt^0. When the ascorbic acid was added as a second step, the observed binding energy was 71.1 eV, also showing that the platinum on the support was in the Pt^0 state. Ascorbic acid was an affective reducing agent for platinum.

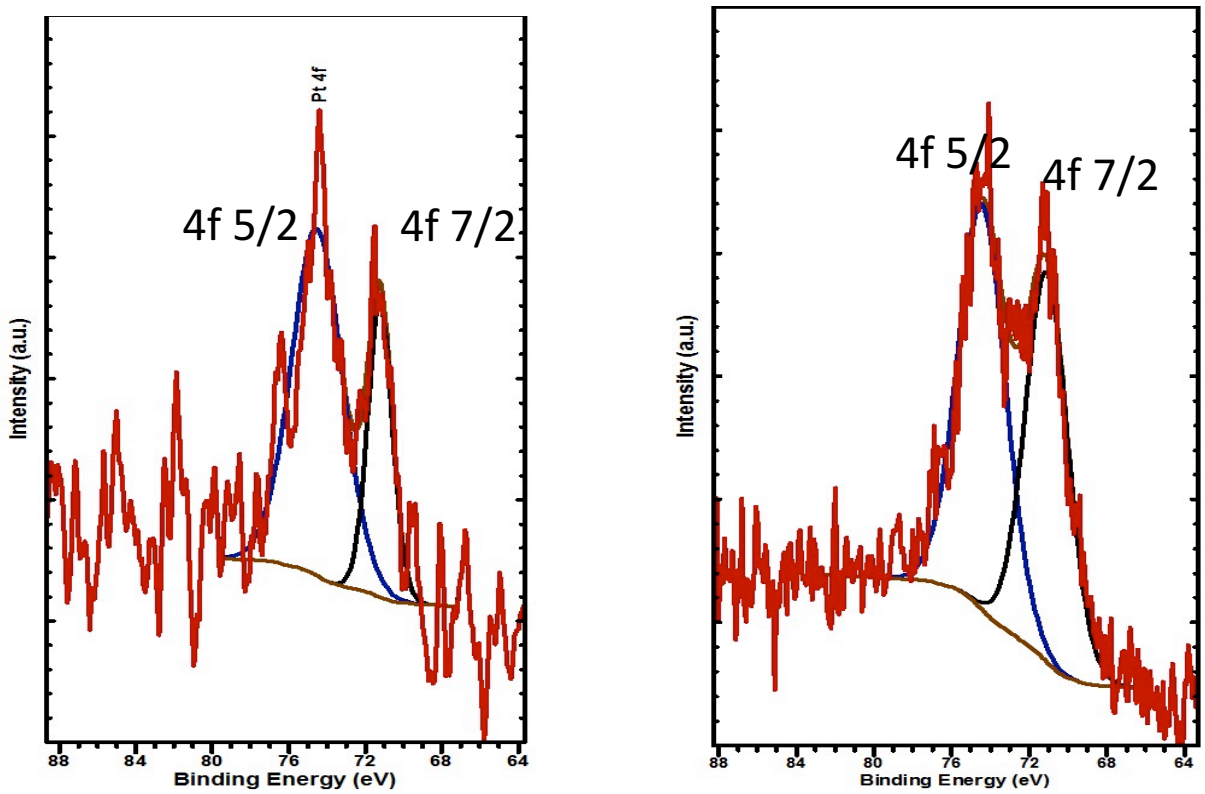

Figure 67 XPS of silica stars after loading platinum by A. reducing before microwave and B. ascorbic acid added as a second step and then microwaved

6.5. Conclusions

In this chapter, the synthesis of platinum nanoparticles onto silica star supports was investigated. When loading with presynthesized colloidal platinum nanoparticles, the wt % of platinum loaded onto the support was low due to the low concentration of platinum in the colloidal solution. A new method that combines incipient wetness with the addition of a

hydrophobic solvent to increase mixing and the homogeneity of platinum nanoparticles throughout the entire support was developed. This method allowed for a more homogenous distribution of platinum throughout the entire silica star support. The catalytic activity and TEM images of the supported platinum nanoparticles are currently under investigation to see how they perform in hydrogenation reactions.

Chapter 7: Conclusions

The main goal of this research was to synthesize metallic nanoparticles for catalytic applications that could be used on an industrial scale. In most academic research laboratories, inorganic synthesis reactions are run using conventional methods such as using a roundbottom flask heated with a mantle. This type of reaction is difficult to scale up to an industrial scale due to ineffective heating methods that are solvent volume dependent.

The major achievements and conclusions achieved by this work are the following:

1. CuPd nanoparticles were synthesized using a facile oleylamine synthesis using conventional heating methods. The nanoparticles were 4.5 nm in diameter and consisted of an alloy of the two metals. On the surface, both metals existed in both metal and oxidized phases with 33% oxidized. This removes the need for a copper halide co-catalyst for the Sonogashira reaction. The CuPd nanoparticles were active for Suzuki cross coupling reactions with both electron withdrawing and donating substituents. The particles exhibited a TOF of 72,000 hr^{-1} and were recyclable up to 5 times while maintaining decent product yields. This work shows that bimetallic nanoparticles can successfully replace co-catalysts and maintain catalytic activity.
2. Core/Shell Cu@Ni and Cu@Co nanocomposites were successfully synthesized using a continuous flow capillary reactor. The nanocomposites synthesized using continuous flow techniques were comparable to those synthesized by conventional benchtop methods. XRD and Reitveld refinement showed that the degree of alloying between the two metals is less when synthesized with continuous flow methods. TEM and EELS shows that the nanoparticles were large and polydisperse, but did have a core/shell

morphology. This core/shell morphology was stable under N_2 until 550 °C. The nanocomposites were tested for Fischer Tropsch synthesis. The Cu@Ni particles behaved as expected and were more selective towards the formation of methane. However, the Cu@Co composites exhibit a surface restructuring to Co_2C and were also more selective to the formation of methane. This work showed that continuous flow methods for synthesizing complex nanoparticles could be achieved and that they were catalytically active.

3. Building off of the work with the continuous flow capillary reactor, a continuous flow microwave capillary reactor was made and used to synthesize colloidal platinum nanoparticles in water. After several optimization reactions using conventional heating methods, conventional microwave methods, and continuous flow microwave capillary reactor methods, 1.7 nm colloidal platinum nanoparticles were achieved. Oxidation studies were completed and used to determine under what oxidative conditions were needed to remove excess organics off the surface of the nanoparticles. However, hydrogenation of octane reactions were completed on organic capped platinum nanoparticles and displayed good catalytic activity, converting over 90% of octane to octane in 15 minutes. More studies are being completed for other hydrogenation reactions such as for crotonaldehyde and characterization of the colloidal nanoparticles.
4. The last section of this research investigated supported platinum nanoparticles. Loading presynthesized colloidal platinum nanoparticles onto the silica star supports resulting in low wt % of platinum on the support. This could be from the low concentration of platinum nanoparticles in the colloidal solution. To overcome this, the synthesis of platinum nanoparticles using microwave irradiation directly onto the support was

investigated. The biggest challenge of this section was to overcome the heterogeneity of the platinum throughout the support. By altering an incipient wetness method by adding an excess of hexanes, more efficient mixing of supports with precursor solution was achieved and the platinum was more evenly distributed.

In the presented work, more cost efficient synthetic methods of metallic nanoparticles for catalytic applications were investigated. This was completed by synthesizing alloyed, core/shell, and single metal catalysts using a variety of methods. By using continuous flow methods for synthesizing nanomaterials, the materials can be produced on an industrial scale. The heat transfer and reaction rate is increased, while the batch-to-batch variability is decreased. Future work should include synthesizing bimetallic alloyed and complex morphology nanoparticles and increasing the number of catalytic reactions.

List of References

1. Wang, C.; Daimon, H.; Onodera, T.; Koda, T.; Sun, S., A General Approach to the Size- and Shape-Controlled Synthesis of Platinum Nanoparticles and Their Catalytic Reduction of Oxygen. *Angewandte Chemie International Edition* **2008,** *47* (19), 3588-3591.
2. Rioux, R. M.; Song, H.; Grass, M.; Habas, S.; Niesz, K.; Hoefelmeyer, J. D.; Yang, P.; Somorjai, G. A., Monodisperse platinum nanoparticles of well-defined shape: synthesis, characterization, catalytic properties and future prospects. *Top. Catal.* **2006,** *39* (3/4), 167-174.
3. Smith, S. E.; Siamaki, A. R.; Gupton, B. F.; Carpenter, E. E., CuPd nanoparticles as a catalyst in carbon-carbon cross-coupling reactions by a facile oleylamine synthesis. *RSC Advances* **2016,** *6* (94), 91541-91545.
4. Huang, G.; Hu, J.; Zhang, H.; Zhou, Z.; Chi, X.; Gao, J., Highly magnetic iron carbide nanoparticles as effective T2 contrast agents. *Nanoscale* **2014,** *6* (6), 726-730.
5. Zhao, C.-X.; He, L.; Qiao, S. Z.; Middelberg, A. P. J., Nanoparticle synthesis in microreactors. *Chem. Eng. Sci.* **2011,** *66* (7), 1463-1479.
6. Wagner, J.; Köhler, J. M., Continuous Synthesis of Gold Nanoparticles in a Microreactor. *Nano Lett.* **2005,** *5* (4), 685-691.
7. Marre, S.; Jensen, K. F., Synthesis of micro and nanostructures in microfluidic systems. *Chem. Soc. Rev.* **2010,** *39* (3), 1183-1202.
8. Smith, S. E.; Huba, Z. J.; Almalki, F.; Regalbuto, J. R.; Monnier, J.; Carpenter, E. E., Continuous-flow synthesis of Cu-M (M=Ni, Co) core—shell nanocomposites. *J. Flow Chem. 0* (0), 1-5.
9. Polte, J., Fundamental growth principles of colloidal metal nanoparticles - a new perspective. *CrystEngComm* **2015,** *17* (36), 6809-6830.
10. Calderone, V. R.; Shiju, N. R.; Curulla-Ferré, D.; Chambrey, S.; Khodakov, A.; Rose, A.; Thiessen, J.; Jess, A.; Rothenberg, G., De Novo Design of Nanostructured Iron–Cobalt Fischer–Tropsch Catalysts. *Angewandte Chemie International Edition* **2013,** *52* (16), 4397-4401.
11. Polshettiwar, V.; Varma, R. S., Green chemistry by nano-catalysis. *Green Chem.* **2010,** *12* (5), 743-754.
12. Na, K.; Zhang, Q.; Somorjai, G. A., Colloidal Metal Nanocatalysts: Synthesis, Characterization, and Catalytic Applications. *J. Cluster Sci.* **2014,** *25* (1), 83-114.
13. Chinchilla, R.; Nájera, C., The Sonogashira Reaction: A Booming Methodology in Synthetic Organic Chemistry†. *Chem. Rev. (Washington, DC, U. S.)* **2007,** *107* (3), 874-922.
14. All Noble Prizes in Chemistry. http://www.nobelprize.org/nobel_prizes/chemistry/laureates/ (accessed April 25, 2015).
15. Wang, D.; Astruc, D., Fast-Growing Field of Magnetically Recyclable Nanocatalysts. *Chem. Rev. (Washington, DC, U. S.)* **2014,** *114* (14), 6949-6985.
16. Corbet, J.-P.; Mignani, G., Selected Patented Cross-Coupling Reaction Technologies. *Chem. Rev. (Washington, DC, U. S.)* **2006,** *106* (7), 2651-2710.
17. Shukla, P.; Sharma, A.; Pallavi, B.; Cheng, C. H., Nickel-catalyzed reductive Heck type coupling of saturated alkyl halides with acrylates and oxabenzonorbornadiene. *Tetrahedron* **2015,** *71* (15), 2260-2266.

18. Shukla, P.; Hsu, Y.-C.; Cheng, C.-H., Cobalt-Catalyzed Reductive Coupling of Saturated Alkyl Halides with Activated Alkenes. *The Journal of Organic Chemistry* **2006,** *71* (2), 655-658.
19. Babu, S. G.; Neelakandeswari, N.; Dharmaraj, N.; Jackson, S. D.; Karvembu, R., Copper(ii) oxide on aluminosilicate mediated Heck coupling of styrene with aryl halides in water. *RSC Advances* **2013,** *3* (21), 7774-7781.
20. Perego, C.; Bortolo, R.; Zennaro, R., Gas to liquids technologies for natural gas reserves valorization: The Eni experience. *Catal. Today* **2009,** *142* (1–2), 9-16.
21. Jahangiri, H.; Bennett, J.; Mahjoubi, P.; Wilson, K.; Gu, S., A review of advanced catalyst development for Fischer-Tropsch synthesis of hydrocarbons from biomass derived syn-gas. *Catalysis Science & Technology* **2014,** *4* (8), 2210-2229.
22. Li, S.; Li, A.; Krishnamoorthy, S.; Iglesia, E., Effects of Zn, Cu, and K Promoters on the Structure and on the Reduction, Carburization, and Catalytic Behavior of Iron-Based Fischer–Tropsch Synthesis Catalysts. *Catal. Lett.* **2001,** *77* (4), 197-205.
23. Tsakoumis, N. E.; Rønning, M.; Borg, Ø.; Rytter, E.; Holmen, A., Deactivation of cobalt based Fischer–Tropsch catalysts: A review. *Catal. Today* **2010,** *154* (3–4), 162-182.
24. Atobe, M.; Okamoto, M.; Fuchigami, T.; Park, J.-E., Selective hydrogenation by polymer-encapsulated platinum nanoparticles prepared by an easy single-step sonochemical synthesis. *Ultrason. Sonochem.* **2010,** *17* (1), 26-29.
25. Johnstone, R. A. W.; Liu, J.-Y.; Lu, L.; Whittaker, D., Hydrogenation of alkenes over palladium and platinum metals supported on a variety of metal(IV) phosphates. *J. Mol. Catal. A: Chem.* **2003,** *191* (2), 289-294.
26. Jung, A.; Jess, A.; Schubert, T.; Schütz, W., Performance of carbon nanomaterial (nanotubes and nanofibres) supported platinum and palladium catalysts for the hydrogenation of cinnamaldehyde and of 1-octyne. *Appl. Catal., A* **2009,** *362* (1–2), 95-105.
27. Xi, P.; Cao, Y.; Yang, F.; Ma, C.; Chen, F.; Yu, S.; Wang, S.; Zeng, Z.; Zhang, X., Facile synthesis of Pd-based bimetallic nanocrystals and their application as catalysts for methanol oxidation reaction. *Nanoscale* **2013,** *5* (13), 6124-6130.
28. Yang, X.; Mueanngern, Y.; Baker, Q. A.; Baker, L. R., Crotonaldehyde hydrogenation on platinum-titanium oxide and platinum-cerium oxide catalysts: selective C[double bond, length as m-dash]O bond hydrogen requires platinum sites beyond the oxide-metal interface. *Catalysis Science & Technology* **2016,** *6* (18), 6824-6835.
29. Bai, L.; Wang, X.; Chen, Q.; Ye, Y.; Zheng, H.; Guo, J.; Yin, Y.; Gao, C., Explaining the Size Dependence in Platinum-Nanoparticle-Catalyzed Hydrogenation Reactions. *Angewandte Chemie International Edition* **2016,** *55* (50), 15656-15661.
30. LaMer, V. K.; Dinegar, R. H., Theory, Production and Mechanism of Formation of Monodispersed Hydrosols. *J. Am. Chem. Soc.* **1950,** *72* (11), 4847-4854.
31. van Embden, J.; Chesman, A. S. R.; Jasieniak, J. J., The Heat-Up Synthesis of Colloidal Nanocrystals. *Chem. Mater.* **2015,** *27* (7), 2246-2285.
32. Thanh, N. T. K.; Maclean, N.; Mahiddine, S., Mechanisms of Nucleation and Growth of Nanoparticles in Solution. *Chem. Rev. (Washington, DC, U. S.)* **2014,** *114* (15), 7610-7630.
33. Pearson, R. G., Hard and Soft Acids and Bases. *J. Am. Chem. Soc.* **1963,** *85* (22), 3533-3539.
34. Fievet, F.; Lagier, J. P.; Blin, B.; Beaudoin, B.; Figlarz, M., Homogeneous and heterogeneous nucleations in the polyol process for the preparation of micron and submicron size metal particles. *Solid State Ionics* **1989,** *32*, 198-205.

35. Rivers, J. H.; Carroll, K. J.; Jones, R. A.; Carpenter, E. E., A copper-polyol complex: [Na2(C2H6O2)6][Cu(C2H4O2)2]. *Acta Crystallographica Section C* **2010,** *66* (3), m83-m85.
36. Dong, H.; Chen, Y. C.; Feldmann, C., Polyol synthesis of nanoparticles: status and options regarding metals, oxides, chalcogenides, and non-metal elements. *Green Chem.* **2015,** *17* (8), 4107-4132.
37. Fereshteh, Z.; Rojaee, R.; Sharifnabi, A., Effect of different polymers on morphology and particle size of silver nanoparticles synthesized by modified polyol method. *Superlattices Microstruct.* **2016,** *98*, 267-275.
38. Boopathi, S.; Raju, C. V.; Jeyabharathi, C.; Kumar, S. S., Synthesis of poly(N-vinyl-2-pyrrolidone) adsorbed-AuPt/C bimetallic nanoparticles and their unusual electrocatalytic activity towards methanol tolerant oxygen reduction reaction. *J. Solid State Electrochem.* **2016,** *20* (2), 579-587.
39. Carroll, K. J.; Reveles, J. U.; Shultz, M. D.; Khanna, S. N.; Carpenter, E. E., Preparation of Elemental Cu and Ni Nanoparticles by the Polyol Method: An Experimental and Theoretical Approach. *J. Phys. Chem. C* **2011,** *115* (6), 2656-2664.
40. Adekoya, J. A.; Mlowe, S.; Dare, E. O.; Mesubi, M. A.; Revaprasadu, N., Synthesis and characterization of polyol stabilised Ag/Co allied nanocomposites. *Superlattices Microstruct.* **2015,** *78*, 97-105.
41. González-Carballo, J. M.; Sadasivan, S.; Landon, P.; Tooze, R. P., Synthesis of cobalt nanodumbbells and their thermal stability under H2, H2/CO and O2 atmospheres. *Mater. Charact.* **2016,** *118*, 519-526.
42. Xia, H.; Xiahou, Y.; Zhang, P.; Ding, W.; Wang, D., Revitalizing the Frens Method To Synthesize Uniform, Quasi-Spherical Gold Nanoparticles with Deliberately Regulated Sizes from 2 to 330 nm. *Langmuir* **2016,** *32* (23), 5870-5880.
43. Turkevich, J.; Stevenson, P. C.; Hillier, J., A study of the nucleation and growth processes in the synthesis of colloidal gold. *Discussions of the Faraday Society* **1951,** *11* (0), 55-75.
44. Wuithschick, M.; Birnbaum, A.; Witte, S.; Sztucki, M.; Vainio, U.; Pinna, N.; Rademann, K.; Emmerling, F.; Kraehnert, R.; Polte, J., Turkevich in New Robes: Key Questions Answered for the Most Common Gold Nanoparticle Synthesis. *ACS Nano* **2015,** *9* (7), 7052-7071.
45. Frens, G., Controlled nucleation for the regulation of the particle size in monodisperse gold suspensions. *Nature, Phys. Sci.* **1973,** *241*, 20-22.
46. Kettemann, F.; Birnbaum, A.; Witte, S.; Wuithschick, M.; Pinna, N.; Kraehnert, R.; Rademann, K.; Polte, J., Missing Piece of the Mechanism of the Turkevich Method: The Critical Role of Citrate Protonation. *Chem. Mater.* **2016,** *28* (11), 4072-4081.
47. Ziegler, C.; Eychmüller, A., Seeded Growth Synthesis of Uniform Gold Nanoparticles with Diameters of 15−300 nm. *J. Phys. Chem. C* **2011,** *115* (11), 4502-4506.
48. Minh, T.; Rebekah, D.; Madeline, T.; Sonal, P., Effect of citrate ratio and temperature on gold nanoparticle size and morphology. *Materials Research Express* **2016,** *3* (10), 105027.
49. Tyagi, H.; Kushwaha, A.; Kumar, A.; Aslam, M., A Facile pH Controlled Citrate-Based Reduction Method for Gold Nanoparticle Synthesis at Room Temperature. *Nanoscale Research Letters* **2016,** *11* (1), 1-11.
50. Lee, P. C.; Meisel, D., Adsorption and surface-enhanced Raman of dyes on silver and gold sols. *The Journal of Physical Chemistry* **1982,** *86* (17), 3391-3395.

51. Gorup, L. F.; Longo, E.; Leite, E. R.; Camargo, E. R., Moderating effect of ammonia on particle growth and stability of quasi-monodisperse silver nanoparticles synthesized by the Turkevich method. *J. Colloid Interface Sci.* **2011,** *360* (2), 355-358.
52. Bigall, N. C.; Härtling, T.; Klose, M.; Simon, P.; Eng, L. M.; Eychmüller, A., Monodisperse Platinum Nanospheres with Adjustable Diameters from 10 to 100 nm: Synthesis and Distinct Optical Properties. *Nano Lett.* **2008,** *8* (12), 4588-4592.
53. Qin, Y.; Ji, X.; Jing, J.; Liu, H.; Wu, H.; Yang, W., Size control over spherical silver nanoparticles by ascorbic acid reduction. *Colloids and Surfaces A: Physicochemical and Engineering Aspects* **2010,** *372* (1–3), 172-176.
54. Zhu, Y.-J.; Chen, F., Microwave-Assisted Preparation of Inorganic Nanostructures in Liquid Phase. *Chem. Rev. (Washington, DC, U. S.)* **2014,** *114* (12), 6462-6555.
55. Gedye, R.; Smith, F.; Westaway, K.; Ali, H.; Baldisera, L.; Laberge, L.; Rousell, J., The use of microwave ovens for rapid organic synthesis. *Tetrahedron Lett.* **1986,** *27* (3), 279-282.
56. Giguere, R. J.; Bray, T. L.; Duncan, S. M.; Majetich, G., Application of commercial microwave ovens to organic synthesis. *Tetrahedron Lett.* **1986,** *27* (41), 4945-4948.
57. Kappe, C. O., Controlled Microwave Heating in Modern Organic Synthesis. *Angewandte Chemie International Edition* **2004,** *43* (46), 6250-6284.
58. Nuchter, M.; Ondruschka, B.; Bonrath, W.; Gum, A., Microwave assisted synthesis - a critical technology overview. *Green Chem.* **2004,** *6* (3), 128-141.
59. Gabriel, C.; Gabriel, S.; H. Grant, E.; H. Grant, E.; S. J. Halstead, B.; Michael P. Mingos, D., Dielectric parameters relevant to microwave dielectric heating. *Chem. Soc. Rev.* **1998,** *27* (3), 213-224.
60. Kappe, C. O.; Dallinger, D.; Murphree, S. S., Practical Microwave Synthesis for Organic Chemists: Strategies, Instruments, and Protocols. In *Practical Microwave Synthesis for Organic Chemists*, Wiley-VCH Verlag GmbH & Co. KGaA: 2009; pp 291-299.
61. de la Hoz, A.; Diaz-Ortiz, A.; Moreno, A., Microwaves in organic synthesis. Thermal and non-thermal microwave effects. *Chem. Soc. Rev.* **2005,** *34* (2), 164-178.
62. Zhang, X.; O. Hayward, D.; Michael P. Mingos, D., Apparent equilibrium shifts and hot-spot formation for catalytic reactions induced by microwave dielectric heating. *Chem. Commun. (Cambridge, U. K.)* **1999,** (11), 975-976.
63. Zhang, X.; Hayward, D. O.; Mingos, D. M. P., Effects of Microwave Dielectric Heating on Heterogeneous Catalysis. *Catal. Lett.* **2003,** *88* (1), 33-38.
64. Schanche, J.-s., Microwave synthesis solutions from personal chemistry. *Mol. Diversity* **2003,** *7* (2-4), 293-300.
65. Bilecka, I.; Niederberger, M., Microwave chemistry for inorganic nanomaterials synthesis. *Nanoscale* **2010,** *2* (8), 1358-1374.
66. Panzarella, B.; Tompsett, G. A.; Yngvesson, K. S.; Conner, W. C., Microwave Synthesis of Zeolites. 2. Effect of Vessel Size, Precursor Volume, and Irradiation Method. *The Journal of Physical Chemistry B* **2007,** *111* (44), 12657-12667.
67. Tu, W.; Liu, H., Rapid synthesis of nanoscale colloidal metal clusters by microwave irradiation. *J. Mater. Chem.* **2000,** *10* (9), 2207-2211.
68. Bilecka, I.; Elser, P.; Niederberger, M., Kinetic and Thermodynamic Aspects in the Microwave-Assisted Synthesis of ZnO Nanoparticles in Benzyl Alcohol. *ACS Nano* **2009,** *3* (2), 467-477.
69. Komarneni, S.; Roy, R.; Li, Q. H., Microwave-hydrothermal synthesis of ceramic powders. *Mater. Res. Bull.* **1992,** *27* (12), 1393-1405.

70. Komarneni, S.; Pidugu, R.; Li, Q. H.; Roy, R., Microwave-hydrothermal processing of metal powders. *J. Mater. Res.* **2011,** *10* (7), 1687-1692.
71. Dahal, N.; García, S.; Zhou, J.; Humphrey, S. M., Beneficial Effects of Microwave-Assisted Heating versus Conventional Heating in Noble Metal Nanoparticle Synthesis. *ACS Nano* **2012,** *6* (11), 9433-9446.
72. Balu, A. M.; Dallinger, D.; Obermayer, D.; Campelo, J. M.; Romero, A. A.; Carmona, D.; Balas, F.; Yohida, K.; Gai, P. L.; Vargas, C.; Kappe, C. O.; Luque, R., Insights into the microwave-assisted preparation of supported iron oxide nanoparticles on silica-type mesoporous materials. *Green Chem.* **2012,** *14* (2), 393-402.
73. BayrakÇEken, A., Platinum or nickel nanoparticles decorated on silica spheres by microwave irradiation technique. *Turk. J. Chem.* **2014,** *38* (2), 309-316.
74. Chen, W.; Zhao, J.; Lee, J. Y.; Liu, Z., Microwave heated polyol synthesis of carbon nanotubes supported Pt nanoparticles for methanol electrooxidation. *Mater. Chem. Phys.* **2005,** *91* (1), 124-129.
75. Elazab, H.; Moussa, S.; Gupton, B. F.; El-Shall, M. S., Microwave-assisted synthesis of Pd nanoparticles supported on Fe3O4, Co3O4, and Ni(OH)2 nanoplates and catalysis application for CO oxidation. *Journal of Nanoparticle Research* **2014,** *16* (7), 1-11.
76. Li, D.; Komarneni, S., Synthesis of Pt Nanoparticles and Nanorods by Microwave-assisted Solvothermal Technique. In *Zeitschrift für Naturforschung B*, 2006; Vol. 61, p 1566.
77. Zhang, L.; Xia, Y., Scaling up the Production of Colloidal Nanocrystals: Should We Increase or Decrease the Reaction Volume? *Adv. Mater. (Weinheim, Ger.)* **2014,** *26* (16), 2600-2606.
78. Shahbazali, E.; Hessel, V.; Noel, T.; Wang, Q., Metallic nanoparticles made in flow and their catalytic applications in organic synthesis. *Nanotechnol. Rev.* **2014,** *3* (1), 65-86.
79. Eluri, R.; Paul, B., Synthesis of nickel nanoparticles by hydrazine reduction: mechanistic study and continuous flow synthesis. *Journal of Nanoparticle Research* **2012,** *14* (4), 1-14.
80. Elvira, K. S.; i Solvas, X. C.; Wootton, R. C. R.; deMello, A. J., The past, present and potential for microfluidic reactor technology in chemical synthesis. *Nat Chem* **2013,** *5* (11), 905-915.
81. Bayazit, M. K.; Yue, J.; Cao, E.; Gavriilidis, A.; Tang, J., Controllable Synthesis of Gold Nanoparticles in Aqueous Solution by Microwave Assisted Flow Chemistry. *ACS Sustainable Chemistry & Engineering* **2016,** *4* (12), 6435-6442.
82. Webb, D.; Jamison, T. F., Continuous flow multi-step organic synthesis. *Chemical Science* **2010,** *1* (6), 675-680.
83. Mi, J.-L.; Clausen, H. F.; Bremholm, M.; Schmøkel, M. S.; Hernández-Fernández, P.; Becker, J.; Iversen, B. B., Pulsed-Flow Near-Critical and Supercritical Synthesis of Carbon-Supported Platinum Nanoparticles and In Situ X-ray Diffraction Study of Their Formation and Growth. *Chem. Mater.* **2015,** *27* (2), 450-456.
84. Welch, C. J.; Albaneze-Walker, J.; Leonard, W. R.; Biba, M.; DaSilva, J.; Henderson, D.; Laing, B.; Mathre, D. J.; Spencer, S.; Bu, X.; Wang, T., Adsorbent Screening for Metal Impurity Removal in Pharmaceutical Process Research. *Organic Process Research & Development* **2005,** *9* (2), 198-205.
85. Garrett, C. E.; Prasad, K., The Art of Meeting Palladium Specifications in Active Pharmaceutical Ingredients Produced by Pd-Catalyzed Reactions. *Adv. Synth. Catal.* **2004,** *346* (8), 889-900.

86. Moussa, S.; Siamaki, A. R.; Gupton, B. F.; El-Shall, M. S., Pd-Partially Reduced Graphene Oxide Catalysts (Pd/PRGO): Laser Synthesis of Pd Nanoparticles Supported on PRGO Nanosheets for Carbon–Carbon Cross Coupling Reactions. *ACS Catal.* **2012,** *2* (1), 145-154.
87. Siamaki, A. R.; Khder, A. E. R. S.; Abdelsayed, V.; El-Shall, M. S.; Gupton, B. F., Microwave-assisted synthesis of palladium nanoparticles supported on graphene: A highly active and recyclable catalyst for carbon–carbon cross-coupling reactions. *J. Catal.* **2011,** *279* (1), 1-11.
88. Athilakshmi, J.; Ramanathan, S.; Chand, D. K., Facile synthesis of palladium nanoclusters and their catalytic activity in Sonogashira coupling reactions. *Tetrahedron Lett.* **2008,** *49* (36), 5286-5288.
89. Guo, S.; Zhang, X.; Zhu, W.; He, K.; Su, D.; Mendoza-Garcia, A.; Ho, S. F.; Lu, G.; Sun, S., Nanocatalyst Superior to Pt for Oxygen Reduction Reactions: The Case of Core/Shell Ag(Au)/CuPd Nanoparticles. *J. Am. Chem. Soc.* **2014,** *136* (42), 15026-15033.
90. Zheng, Z.; Li, H.; Liu, T.; Cao, R., Monodisperse noble metal nanoparticles stabilized in SBA-15: Synthesis, characterization and application in microwave-assisted Suzuki–Miyaura coupling reaction. *J. Catal.* **2010,** *270* (2), 268-274.
91. Shaabani, A.; Mahyari, M., PdCo bimetallic nanoparticles supported on PPI-grafted graphene as an efficient catalyst for Sonogashira reactions. *J. Mater. Chem. A* **2013,** *1* (32), 9303-9311.
92. Mazumder, V.; Chi, M.; Mankin, M. N.; Liu, Y.; Metin, Ö.; Sun, D.; More, K. L.; Sun, S., A Facile Synthesis of MPd (M = Co, Cu) Nanoparticles and Their Catalysis for Formic Acid Oxidation. *Nano Lett.* **2012,** *12* (2), 1102-1106.
93. Heshmatpour, F.; Abazari, R.; Balalaie, S., Preparation of monometallic (Pd, Ag) and bimetallic (Pd/Ag, Pd/Ni, Pd/Cu) nanoparticles via reversed micelles and their use in the Heck reaction. *Tetrahedron* **2012,** *68* (14), 3001-3011.
94. Myers, S. V.; Frenkel, A. I.; Crooks, R. M., X-ray Absorption Study of PdCu Bimetallic Alloy Nanoparticles Containing an Average of ~64 Atoms. *Chem. Mater.* **2009,** *21* (20), 4824-4829.
95. Nasrollahzadeh, M.; Banaei, A., Hybrid Au/Pd nanoparticles as reusable catalysts for Heck coupling reactions in water under aerobic conditions. *Tetrahedron Lett.* **2015,** *56* (3), 500-503.
96. Rossy, C.; Majimel, J.; Delapierre, M. T.; Fouquet, E.; Felpin, F.-X., Palladium and copper-supported on charcoal: A heterogeneous multi-task catalyst for sequential Sonogashira–Click and Click–Heck reactions. *J. Organomet. Chem.* **2014,** *755* (0), 78-85.
97. Kidwai, M.; Mishra, N. K.; Bhardwaj, S.; Jahan, A.; Kumar, A.; Mozumdar, S., Cu Nanoparticles in PEG: A New Recyclable Catalytic System for N-Arylation of Amines with Aryl Halides. *ChemCatChem* **2010,** *2* (10), 1312-1317.
98. Vegard, L., Die Konstitution der Mischkristalle und die Raumfüllung der Atome. *Zeitschrift für Physik* **1921,** *5* (1), 17-26.
99. Scherrer, P., Bestimmung der Grösse und der inneren Struktur von Kolloidteilchen mittels Röntgenstrahlen. *Nachr. Ges. Wiss. Göttingen* **1918,** *26*, 98-100.
100. Carroll, K. J.; Calvin, S.; Ekiert, T. F.; Unruh, K. M.; Carpenter, E. E., Selective Nucleation and Growth of Cu and Ni Core/Shell Nanoparticles. *Chem. Mater.* **2010,** *22* (7), 2175-2177.
101. Bonet, F.; Grugeon, S.; Dupont, L.; Urbina, R. H.; Guéry, C.; Tarascon, J. M., Synthesis and characterization of bimetallic Ni–Cu particles. *J. Solid State Chem.* **2003,** *172* (1), 111-115.

102. Kodama, R. H., Magnetic nanoparticles. *J. Magn. Magn. Mater.* **1999,** *200* (1–3), 359-372.
103. Smetana, A. B.; Wang, J. S.; Boeckl, J. J.; Brown, G. J.; Wai, C. M., Deposition of Ordered Arrays of Gold and Platinum Nanoparticles with an Adjustable Particle Size and Interparticle Spacing Using Supercritical CO2. *J. Phys. Chem. C* **2008,** *112* (7), 2294-2297.
104. Slostowski, C.; Marre, S.; Babot, O.; Toupance, T.; Aymonier, C., Near- and Supercritical Alcohols as Solvents and Surface Modifiers for the Continuous Synthesis of Cerium Oxide Nanoparticles. *Langmuir* **2012,** *28* (48), 16656-16663.
105. Choi, H.; Veriansyah, B.; Kim, J.; Kim, J. D.; Kang, J. W., Continuous synthesis of metal nanoparticles in supercritical methanol. *J. Supercrit. Fluids* **2010,** *52* (3), 285-291.
106. Pascu, O.; Marre, S.; Aymonier, C.; Roig, A., Ultrafast and continuous synthesis of crystalline ferrite nanoparticles in supercritical ethanol. *Nanoscale* **2013,** *5* (5), 2126-2132.
107. Clifford, D. M.; El-Gendy, A. A.; Lu, A. J.; Pestov, D.; Carpenter, E. E., Room Temperature Synthesis of Highly Magnetic Cobalt Nanoparticles by Continuous Flow in a Microfluidic Reactor. *J. Flow Chem.* **2014,** *4* (3), 148-152.
108. Xu, L.; Srinivasakannan, C.; Peng, J.; Zhang, D.; Chen, G., Synthesis of nickel nanoparticles by aqueous reduction in continuous flow microreactor. *Chemical Engineering and Processing: Process Intensification* **2015,** *93*, 44-49.
109. Søndergaard, M.; Bøjesen, E. D.; Christensen, M.; Iversen, B. B., Size and Morphology Dependence of ZnO Nanoparticles Synthesized by a Fast Continuous Flow Hydrothermal Method. *Cryst. Growth Des.* **2011,** *11* (9), 4027-4033.
110. Testino, A.; Pilger, F.; Lucchini, M.; Quinsaat, J.; Stähli, C.; Bowen, P., Continuous Polyol Synthesis of Metal and Metal Oxide Nanoparticles Using a Segmented Flow Tubular Reactor (SFTR). *Molecules* **2015,** *20* (6), 10566.
111. Gao, W.; Zhao, Y.; Chen, H.; Chen, H.; Li, Y.; He, S.; Zhang, Y.; Wei, M.; Evans, D. G.; Duan, X., Core-shell Cu@(CuCo-alloy)/Al2O3 catalysts for the synthesis of higher alcohols from syngas. *Green Chem.* **2015,** *17* (3), 1525-1534.
112. Xiao, K.; Bao, Z.; Qi, X.; Wang, X.; Zhong, L.; Fang, K.; Lin, M.; Sun, Y., Structural evolution of CuFe bimetallic nanoparticles for higher alcohol synthesis. *J. Mol. Catal. A: Chem.* **2013,** *378*, 319-325.
113. Singh, A. K.; Xu, Q., Synergistic Catalysis over Bimetallic Alloy Nanoparticles. *ChemCatChem* **2013,** *5* (3), 652-676.
114. Spivey, J. J.; Egbebi, A., Heterogeneous catalytic synthesis of ethanol from biomass-derived syngas. *Chem. Soc. Rev.* **2007,** *36* (9), 1514-1528.
115. Nafria, R.; Genç, A.; Ibáñez, M.; Arbiol, J.; Ramírez de la Piscina, P.; Homs, N.; Cabot, A., Co–Cu Nanoparticles: Synthesis by Galvanic Replacement and Phase Rearrangement during Catalytic Activation. *Langmuir* **2016,** *32* (9), 2267-2276.
116. Schoenitz, M.; Grundemann, L.; Augustin, W.; Scholl, S., Fouling in microstructured devices: a review. *Chem. Commun. (Cambridge, U. K.)* **2015,** *51* (39), 8213-8228.
117. Huba, Z. J.; Carpenter, E. E., Ethanol assisted reduction and nucleation of ferromagnetic Co and Ni nanocrystalline particles. *CrystEngComm* **2013,** *15* (44), 8919-8923.
118. Pearson, W. B., *Handbook of Lattice Spacings and Stuctures of Metals*. Pergamon Press Ltd.: Oxford, 1967.
119. Cha, S. I.; Mo, C. B.; Kim, K. T.; Hong, S. H., Ferromagnetic Cobalt Nanodots, Nanorices, Nanowires and Nanoflowers by Polyol Process. *J. Mater. Res.* **2005,** *20* (8), 2148-2153.

120. Ung, D.; Soumare, Y.; Chakroune, N.; Viau, G.; Vaulay, M. J.; Richard, V.; Fiévet, F., Growth of Magnetic Nanowires and Nanodumbbells in Liquid Polyol. *Chem. Mater.* **2007,** *19* (8), 2084-2094.
121. DiPietro, R. S.; Johnson, H. G.; Bennett, S. P.; Nummy, T. J.; Lewis, L. H.; Heiman, D., Determining magnetic nanoparticle size distributions from thermomagnetic measurements. *Appl. Phys. Lett.* **2010,** *96* (22), ---.
122. Sakharov, A. M.; Mazaletskaya, L. I.; Skibida, I. P., Catalytic Oxidative Deformylation of Polyethylene Glycols with the Participation of Molecular Oxygen. *Kinet. Catal.* **2001,** *42* (5), 662-668.
123. Li, T.; Wang, H.; Yang, Y.; Xiang, H.; Li, Y., Study on an iron–nickel bimetallic Fischer–Tropsch synthesis catalyst. *Fuel Process. Technol.* **2014,** *118*, 117-124.
124. Mohandas, J. C.; Gnanamani, M. K.; Jacobs, G.; Ma, W.; Ji, Y.; Khalid, S.; Davis, B. H., Fischer–Tropsch Synthesis: Characterization and Reaction Testing of Cobalt Carbide. *ACS Catal.* **2011,** *1* (11), 1581-1588.
125. Dry, M. E., Practical and theoretical aspects of the catalytic Fischer-Tropsch process. *Appl. Catal., A* **1996,** *138* (2), 319-344.
126. Schulz, H., Short history and present trends of Fischer–Tropsch synthesis. *Appl. Catal., A* **1999,** *186* (1–2), 3-12.
127. Piella, J.; Bastús, N. G.; Puntes, V., Size-Controlled Synthesis of Sub-10-nanometer Citrate-Stabilized Gold Nanoparticles and Related Optical Properties. *Chem. Mater.* **2016**.
128. Luty-Błocho, M.; Wojnicki, M.; Grzonka, J.; Kurzydłowski, K. J., The Synthesis of Stable Platinum Nanoparticles in the Microreactor. In *Archives of Metallurgy and Materials*, 2014; Vol. 59, p 509.
129. Harada, M.; Cong, C., Microwave-Assisted Polyol Synthesis of Polymer-Protected Monometallic Nanoparticles Prepared in Batch and Continuous-Flow Processing. *Ind. Eng. Chem. Res.* **2016,** *55* (19), 5634-5643.
130. Bayazit, M. K.; Cao, E.; Gavriilidis, A.; Tang, J., A microwave promoted continuous flow approach to self-assembled hierarchical hematite superstructures. *Green Chem.* **2016,** *18* (10), 3057-3065.
131. Glasnov, T. N.; Kappe, C. O., Microwave-Assisted Synthesis under Continuous-Flow Conditions. *Macromol. Rapid Commun.* **2007,** *28* (4), 395-410.
132. Horikoshi, S.; Abe, H.; Torigoe, K.; Abe, M.; Serpone, N., Access to small size distributions of nanoparticles by microwave-assisted synthesis. Formation of Ag nanoparticles in aqueous carboxymethylcellulose solutions in batch and continuous-flow reactors. *Nanoscale* **2010,** *2* (8), 1441-1447.
133. Borodko, Y.; Habas, S. E.; Koebel, M.; Yang, P.; Frei, H.; Somorjai, G. A., Probing the Interaction of Poly(vinylpyrrolidone) with Platinum Nanocrystals by UV−Raman and FTIR. *The Journal of Physical Chemistry B* **2006,** *110* (46), 23052-23059.
134. Suryawanshi, P. L.; Gumfekar, S. P.; Kumar, P. R.; Kale, B. B.; Sonawane, S. H., Synthesis of ultra-small platinum nanoparticles in a continuous flow microreactor. *Colloid and Interface Science Communications* **2016,** *13*, 6-9.
135. Du, Y. K.; Yang, P.; Mou, Z. G.; Hua, N. P.; Jiang, L., Thermal decomposition behaviors of PVP coated on platinum nanoparticles. *J. Appl. Polym. Sci.* **2006,** *99* (1), 23-26.
136. Park, J. Y.; Aliaga, C.; Renzas, J. R.; Lee, H.; Somorjai, G. A., The Role of Organic Capping Layers of Platinum Nanoparticles in Catalytic Activity of CO Oxidation. *Catal. Lett.* **2009,** *129* (1), 1-6.

137. Cai, F.; Shan, S.; Yang, L.; Chen, B.; Luo, J.; Zhong, C.-J., CO oxidation on supported platinum group metal (PGM) based nanoalloys. *Science China Chemistry* **2015,** *58* (1), 14-28.
138. Härelind Ingelsten, H.; Béziat, J.-C.; Bergkvist, K.; Palmqvist, A.; Skoglundh, M.; Qiuhong, H.; Falk, L. K. L.; Holmberg, K., Deposition of Platinum Nanoparticles, Synthesized in Water-in-Oil Microemulsions, on Alumina Supports. *Langmuir* **2002,** *18* (5), 1811-1818.
139. Radivojević, D.; Seshan, K.; Lefferts, L., Preparation of well-dispersed Pt/SiO2 catalysts using low-temperature treatments. *Appl. Catal., A* **2006,** *301* (1), 51-58.
140. Banerjee, S.; Dasgupta, K.; Kumar, A.; Ruz, P.; Vishwanadh, B.; Joshi, J. B.; Sudarsan, V., Comparative evaluation of hydrogen storage behavior of Pd doped carbon nanotubes prepared by wet impregnation and polyol methods. *Int. J. Hydrogen Energy* **2015,** *40* (8), 3268-3276.
141. Zhao, Y.; Jia, L.; Medrano, J. A.; Ross, J. R. H.; Lefferts, L., Supported Pd Catalysts Prepared via Colloidal Method: The Effect of Acids. *ACS Catal.* **2013,** *3* (10), 2341-2352.
142. Jiang, T.; Du, S.; Jafari, T.; Zhong, W.; Sun, Y.; Song, W.; Luo, Z.; Hines, W. A.; Suib, S. L., Synthesis of mesoporous γ-Fe2O3 supported palladium nanoparticles and investigation of their roles as magnetically recyclable catalysts for nitrobenzene hydrogenation. *Appl. Catal., A* **2015,** *502*, 105-113.
143. Barau, A.; Budarin, V.; Caragheorgheopol, A.; Luque, R.; Macquarrie, D. J.; Prelle, A.; Teodorescu, V. S.; Zaharescu, M., A Simple and Efficient Route to Active and Dispersed Silica Supported Palladium Nanoparticles. *Catal. Lett.* **2008,** *124* (3), 204-214.
144. Derible, A.; Diebold, C.; Dentzer, J.; Gadiou, R.; Becht, J.-M.; Le Drian, C., A Palladium Catalyst Supported on Carbon-Coated Cobalt Nanoparticles – Preparation of Palladium-Free Biaryls by Suzuki–Miyaura Reactions in Ethanol. *Eur. J. Org. Chem.* **2014,** *2014* (34), 7699-7706.
145. Glaspell, G.; Fuoco, L.; El-Shall, M. S., Microwave Synthesis of Supported Au and Pd Nanoparticle Catalysts for CO Oxidation. *The Journal of Physical Chemistry B* **2005,** *109* (37), 17350-17355.
146. Peng, Z.; Kisielowski, C.; Bell, A. T., Surfactant-free preparation of supported cubic platinum nanoparticles. *Chem. Commun. (Cambridge, U. K.)* **2012,** *48* (13), 1854-1856.
147. Zhang, Y.; Erkey, C., Preparation of supported metallic nanoparticles using supercritical fluids: A review. *The Journal of Supercritical Fluids* **2006,** *38* (2), 252-267.
148. Samad, J. E.; Blanchard, J.; Sayag, C.; Louis, C.; Regalbuto, J. R., The controlled synthesis of metal-acid bifunctional catalysts: Selective Pt deposition and nanoparticle synthesis on amorphous aluminosilicates. *J. Catal.* **2016,** *342*, 213-225.

Vita

Sarah Emily Smith was born on December 29th, 1989 in Howard County, Maryland. She received her an ACS certified bachelors degree in chemistry from the University of Mary Washington in 2012. Sarah joined the VCU Chemistry Graduate Program in Fall 2012. She joined Everett E. Carpenter's research group in Spring 2013. While at VCU, she was a teaching assistant for general chemistry recitations, labs, and inorganic chemistry lecture. In 2015 She received the Outstanding Graduate Teaching Award and the Lidia M. Vallarino Scholarship. In 2016, Sarah received the Altria Graduate Assistantship sponsored by the Altria Group, Inc.